UNIVERSITÉ DU QUÉBEC

MÉMOIRE PRÉSENTÉ À
L'UNIVERSITÉ DU QUÉBEC À CHICOUTIMI
COMME EXIGENCE PARTIELLE
DE LA MAÎTRISE EN INGÉNIERIE

PAR

EBRAHIM JEDDI

NUMERICAL STUDY OF ANODIC VOLTAGE DROP IN THE HALL-HÉROULT CELLS BY FINITE ELEMENT METHOD

ÉTUDE NUMÉRIQUE DE LA CHUTE DE VOLTAGE ANODIQUE DANS LES CUVES HALL-HÉROULT PAR LA MÉTHODE DES ÉLÉMENTS FINIS

AVRIL 2012

Dedicated to my parents
with love and gratitude
for their unstinting support

ABSTRACT

Aluminum production using the Hall–Héroult process requires an intensive electric current. With an increasing demand for aluminum due to the growth in use of raw materials such as aluminum, and economic developments, aluminum producers are striving to reduce their production costs to remain competitive in a difficult market. One way of doing this is to reduce the voltage drop in the Hall-Héroult cells, which yields a remarkable amount of savings in the long term from only a slight optimization. For this reason, a thorough understanding of the phenomena taking place during operation is necessary.

In this research work, anode assembly as one of the major components of the Hall-Héroult cell was modeled using APDL (ANSYS® Parametric Design Language). The newly presented features of the full anode assembly model, which make it a robust one in terms of geometrical modeling, were introduced in detail. A submodel was extracted from the full model to carry out primary numerical simulations to investigate the Thermo-Electro-Mechanical (TEM) phenomena taking place in the stub hole region to where up to 25% of the total voltage drop in the anode assembly, caused by contact resistance at the interfaces, is attributed. Special attention was paid to the good prediction of contact conditions at the cast iron to carbon interface. In comparison to previous research work, a more thorough and precise approach was taken to employ equations used to predict the initial air gap at the cast iron to carbon interface, which has an influential role in controlling contact particularly at lower temperatures (400°-600°).

In order to calibrate the model, experimental tests, performed by the Arvida Research and Development Centre (ARDC) at Rio Tinto Alcan (RTA), were utilized. FESh++ was used to calibrate the fully coupled TEM model using the results obtained by RTA; subsequently, sensitivity analysis (SA) was performed to investigate the influences of changes in material properties and cast iron/carbon interface characteristics. Also, one study on the geometrical sensitivity, namely, SA on the change in the diameter of the stub, was fulfilled.

After detailed discussions using the various simulation results as well as statistical data obtained from the newly implemented feature in FESh++, conclusions were drawn as to the importance of precise prediction of the initial air gap, contact establishment and condition at the interface, essentiality of the carbon constitutive law, significance of phase change of cast iron, temperature dependency of some materials and anisotropy of electrical resistance of carbon, etc. Finally, suggestions were proposed for future research work and developments such as: considering a better constitutive law for carbon, taking account of creep in cast iron, evaluation of the initial air gap distribution through simulation of cast iron solidification, etc.

RÉSUMÉ

La production de l'aluminium primaire via le procédé hall-Héroult nécessite l'utilisation d'un courant de très forte intensité. Conséquent d'une demande croissante de l'aluminium et du coût élevé des matières premières nécessaires à la production du métal gris, il devient prioritaire pour les producteurs d'aluminium d'assurer un meilleur contrôle du procédé et ce, afin de réduire les coûts de production et ainsi, demeurer compétitif à l'échelle mondiale. Une façon d'atteindre cet objectif consiste à identifier les zones les plus résistives électriquement dans la cellule d'électrolyse et de réduire, lorsque possible, ces résistances, afin de minimiser sa consommation énergétique. Dans cette optique, une compréhension approfondie des phénomènes qui prennent place pendant l'opération ainsi que leurs interactions demeurent de toute première importance est essentiel.

Dans le cadre de ce travail, on s'attarde plus précisément à l'étude des chutes de voltage dans les assembles anodiques, constituante hautement résistive de la cellule d'électrolyse. L'assemblage anodique est modélisé sous ANSYS à l'aide du langage APDL® (ANSYS Parametric Design Language), un langage de programmation utilisé dans le logiciel de simulation ANSYS. Ce langage est également utilisable dans le volet Mechanical du logiciel ANSYS Workbench. Totalement paramétré, le modèle géométrique peut être transformé afin de permettre l'étude spécifique de diverses composantes selon certaines hypothèses simplificatrices. En particulier, un sous-modèle a été extrait du modèle afin de réaliser des simulations numériques dans la zone du tourillon et ce, afin d'étudier les phénomènes Thermo-électro-mécaniques (TEM) prenant place dans cette zone critique de l'assemblage où près de 25% de la chute de voltage anodique se produit; chute de voltage attribuable à la résistance de contact électrique à l'interface fonte/carbone. Une attention particulière a été portée sur la bonne représentation des conditions de contact TEM à cette interface. En particulier, une extension de la méthode simplifiée proposée par Richard a été utilisée afin de quantifier l'espace d'air initial à l'interface fonte/carbone; élément crucial dans le comportement de l'assemblage anodique et qui a un rôle déterminant dans l'évolution des conditions de contact, particulièrement à basses températures (400°C – 600°C). L'ensemble des simulations numériques a été réalisé à l'aide d'une application spécifique développée dans l'environnement FESh++ via une approche fortement couplée des champs de voltage, température et déplacement en régime établi.

La calibration du modèle a été réalisée à l'aide de résultats issus d'essais expérimentaux réalisés au Centre de Recherche et de Développement Arvida (CRDA) de Rio Tinto Alcan (RTA). Par la suite, une étude de sensibilité a été conduite afin d'étudier l'impact de certaines modifications matérielles et/ou géométriques sur le comportement de l'assemblage anodique.

Plus spécifiquement il apparait clairement que les congés du tourillon, la température nominale du rondin au moment du scellement ainsi que le changement de phase de l'acier et de la fonte ont un impact majeur sur la chute de voltage.

Finalement, les recommandations proposées permettront d'améliorer la performance des assemblages anodiques et d'orienter les travaux futurs dans ce domaine de recherche. On pense ici à l'utilisation d'une loi de comportement représentative pour le carbone (comportement quasi-fragile), à la prise en compte du comportement en fluage de l'acier du rondin et de la fonte de scellement ainsi qu'à la prédiction par simulation numérique de l'étape de scellement afin d'obtenir une représentation plus précise de l'espace d'air à l'interface fonte/carbone.

ACKNOWLEDGEMENTS

This research would not have been possible without the support of many people.

The author would like to express his deepest gratitude to his supervisor **Prof. Daniel Marceau** for giving him the chance to make a turning point in his master's studies. Prof. Marceau's professionalism and knowledge was a tremendous help in this research work. The author would also like to acknowledge the debt he owes Prof. Marceau for the support, encouragement and the lessons he taught the author to be more successful in his future career.

The author wishes also to convoy his great appreciation to **Prof. Laszlo Kiss**, the co-supervisor of this research work, for his invaluable guidance and professional input in this work. Prof. Kiss' kind advice, support and persuasion were all enlightening.

Special thanks also to the industrial partner team in this project, namely **Mr. Jean-Francois Bilodeau**, **Mr. Denis Laroche** and **Mr. Lyès Hacini** from the Arvida Research & Development Center at Rio Tinto Alcan without whose professional input and experimental research provision this research work would not have been successful. Thanks to Lyès Hacini for his kind assistance in the calibration part of this work.

Thanks and appreciations are also due to **Prof. Martin Désilets** from the mechanical engineering department at the University of Sherbrooke and **Mr. Lyès Hacini** for their revision and comments on this thesis.

Not forgetting his support on the infrastructure of the cluster and who kept the cluster functional and running during the simulations, the author would like to take this opportunity to thank **Mr. Étienne Lafrenière**.

The author would like to convey thanks to **Rio Tinto Alcan, National Sciences and Engineering Research Council of Canada (NSERC)** and **Aluminium Research Centre (REGAL)** for providing the financial means.

And, last but not least, the author wishes to express his deepest love and gratitude to his beloved parents and his family for their understanding, patience and endless love and also his friends for their help and support through the duration of his master's studies.

TABLE OF CONTENTS

TABLE OF FIGURES

LIST OF TABLES

PREFACE

This document presents the master's thesis of the engineering program by the author, Ebrahim Jeddi, at UQAC[1] – CURAL[2], which is a numerical study on the anodic voltage drop in the Hall-Héroult (HH) cells using finite element method.

The project is a part of a larger project, under a registered research program at Natural Sciences and Engineering Research Council of Canada (NSERC), in partnership with Rio Tinto Alcan (RTA), whose main objective is to develop a numerical tool for the anode assembly analysis.

The document is also presented as the final report to RTA; however, owing to the non-disclosure agreement (NDA) with RTA, confidential materials are excluded from the public version of the document (available for public viewing) and are presented as appendices only to RTA. The charts demonstrating the results obtained from simulations have been normalized to preserve the right of RTA to be the only party to have access to the absolute values of the results.

---

[1] *Université du Québec à Chicoutimi*

[2] *Centre Universitaire de Recherche sur l'Aluminium*

CHAPTER 1:
INTRODUCTION

1.1 General points

Aluminum is the world's most used metal after iron. It is the most abundant metal in the earth's crust (8%). Nearly three-quarters of all aluminum ever produced globally remains in use today. It is the second most malleable and the sixth most ductile metal. Some of its alloys have the same strength as steel but aluminum is three times lighter than steel [1]. Today, use of aluminum encompasses a wide range of variety such as: construction, packaging, electric/engineering industry, transport, design and pharmaceutics. More than a century ago, aluminum was first used in buildings and now aluminum is in every building in the form of window frames, doors, handles, ceiling and roofs etc. Imagining an airplane manufactured without aluminum is almost impossible. The automobile industry is now more inclined to manufacture more parts with aluminum. Moreover, aluminum is a non-toxic metal which has been widely adopted for medicine and packaging. It is used enormously in packaging drinks, medications and even food. Kitchens are full of aluminum appliances and artists have even found it useful to easily use it in their work.

Today's aluminum industry is the subject of an international competition which is forcing producers to reduce their production costs and their carbon emissions. Canada, as the third largest producer of aluminum in the world, can afford no slackening. Economic development and population growth around the world have resulted in an increase in the use of aluminum. While demand for this exceptional metal is growing, it is necessary to examine the impact of this continuing growth on the environment, since aluminum mass production is accompanied by pollution. The use of new technology has resolved this to some extent, but the problem still exists. Aluminum production is a multidimensional manufacturing process; however, there are two main sources which produce aluminum: **Primary aluminum** is the process of extraction of alumina from bauxite and transforming it to aluminum through electrolysis. Recycled aluminum is known as secondary aluminum. **Secondary aluminum** is produced in a wide range of formats as presented in figure 1.1 in conjunction with primary aluminum production steps. The work presented in this thesis is categorized as primary aluminum production.

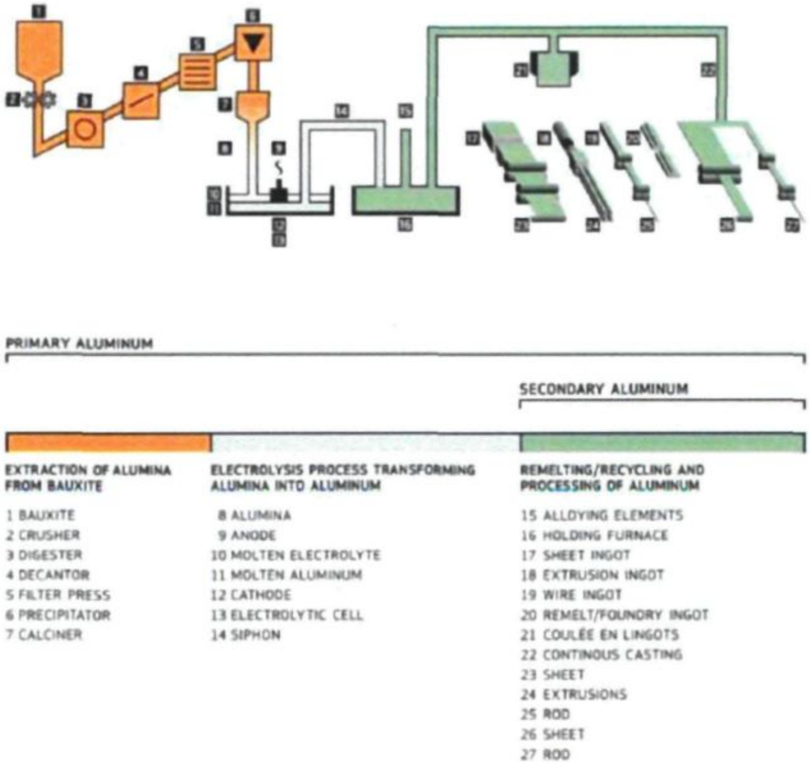

Figure 1.1: A multidimensional manufacturing process [1]

Today, annual world production has reached 41 million metric tons, of which approximately 7% is made in Canada [1], after China and Russia the largest producer of aluminum [2]. To remain a leader among the most innovative industries, the boundaries of knowledge must be constantly pushed back. This applies to Canada's aluminum industry, especially in Quebec, where most of its aluminum smelters are located. To do so, research projects in various domains of aluminum production are constantly defined by the aluminum producers including RTA. The work presented in this thesis is only a small part of one of them which focuses on the development of a numerical tool to better investigate the phenomena relevant to the aluminum reduction.

1.2 The Hall-Héroult process

The **Hall-Héroult** process is the major industrial process for the production of aluminum which is carried out in electrolytic cells or **reduction cell** (pots). An intensive electric current passes from anode to cathode through a bath of molten **cryolite** (Na_3AlF_6). It involves dissolving **alumina** (Al_2O_3) in molten cryolite at approximately 960°C, and electrolyzing the solution to obtain pure aluminum metal. Alumina is decomposed to aluminum such that:

$$2Al_2O_3^{dissolved} + 3C^{solid} = 4Al^{liquid} + 3CO_2^{gas} \tag{1.1}$$

Aluminum oxide has a melting point of over 2,000°C while pure cryolite has a melting point of 1,012°C; a small percentage of aluminum oxide dissolved in cryolite has a melting point of about 1,000°C. **Aluminum fluoride** (AlF_3) is also present in order to reduce the melting point of the cryolite. The mixture is electrolyzed which causes the liquid aluminum to be deposited at the cathode as a precipitate, while the oxygen from the alumina oxidizes the carbon anode to form carbon dioxide. The electrical voltage across each cell is low (typically 3-5 volts DC), but a considerable amount of current is drawn by the circuit. In state-of-the-art cells, the current can be from 220 kA [1] to 400 kA [3]. Today, some of the cells are operated with currents up to and beyond 500 kA. It can be easily concluded that the Hall-Héroult process deals with high temperatures and a large extent of energy, particularly when it comes to the mass production of aluminum in a long run. Figure 1.2 depicts a pot room at the Grande-Baie smelter of Rio Tinto Alcan in which some Hall-Héroult cells can be seen on a potline.

Figure 1.2: Hall-Héroult electrolytic cells (Grande-Baie smelter, Rio Tinto Alcan)

More specifically, figure 1.3 depicts the schema of a typical reduction cell cross section which is used to produce aluminum through the Hall-Héroult process. This figure shows that a reduction cell consists of many different components of which busbar, fume collection hood, steel shell and cradles, refractory (ceramic) and carbon side walls, carbon anodes, electrolyte (bath), crust, collector bars and anode assembly can be mentioned as the main parts that are installed on an insulated ground.

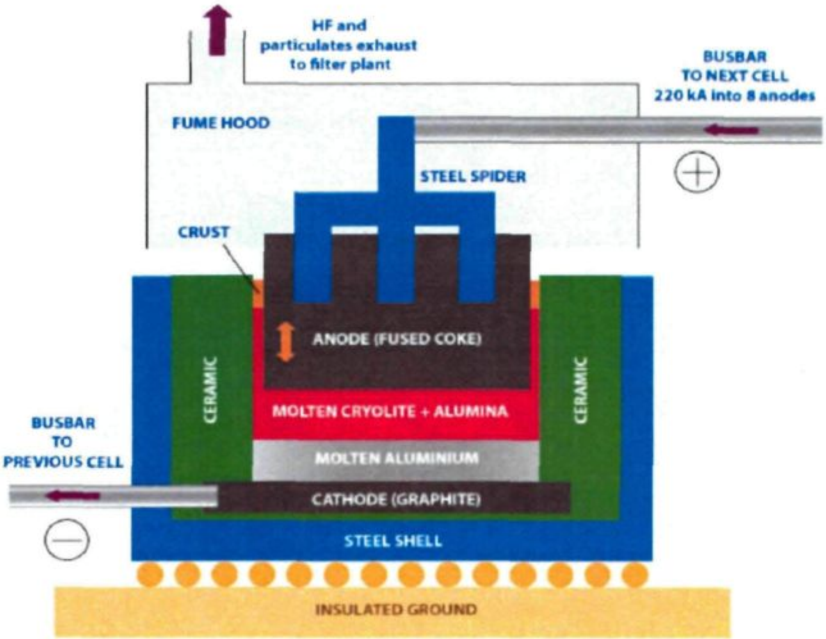

Figure 1.3 : Simplified cross section of a Hall-Héroult cell [3]

In figure 1.4, the **anode assembly**, one of the main parts of the reduction cell, which consists of 3 main parts, is schematically depicted. The **anode hanger (superior part)**, a main part of anode assembly, is itself a metallic assembly that is used to hold carbon anode(s) (blocks), another main part of the anode assembly, partially immersed in electrolyte (bath). Cast iron connectors, as the third main part of the anode assembly, connect and fix the superior part to the carbon block(s). A Superior part typically is an assembly made of an aluminum (copper in some technologies) rod (stem), a steel yoke (with 2 to 6 yoke arms) and steel stubs equivalent to the number of yoke arms. The electric current is fed by the busbar from the top to the anode assembly. After passing through all of the components of the anode assembly, the current is conducted to the carbon cathode through the bath facilitating the chemical reaction to decompose alumina to aluminum. Figure 1.4 shows an anode assembly with one carbon block and a yoke of 4 arms (tetrapod); nevertheless, this is not always the case. The number of yoke arms and carbon blocks varies from one technology to another. The subject of this work is the AP30 technology which is a hexapod yoke (6 yoke arms) with two carbon blocks.

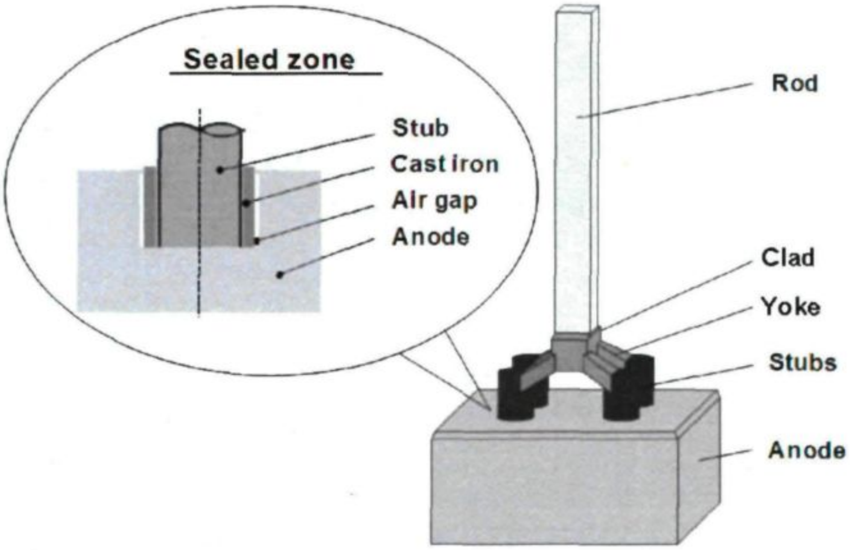

Figure 1.4: Schematic anode assembly [4]

Carbon (anode) is the only part which is consumed to reduce alumina to aluminum according to equation (1.1). The lifespan of carbon depends on the technology and the current density: the higher the operation current, the shorter the lifespan of the carbon. In the AP30 technology usually carbon is consumed in 20 to 30 days. Once carbon reaches the end of its lifetime new carbon blocks must be installed. Carbon anodes have specially designed holes called **stub holes** into which the stubs (of the superior part) are positioned and molten iron is cast to connect and fix stubs to the carbon blocks. An air gap at the cast iron to carbon interface opens up once cast iron solidifies in **anode sealing (rodding)**. Steel to cast iron interface is not a perfect link; however, it is known that compared to the cast iron/carbon interface, there is a good connection between two components to conduct heat and electricity. Cast iron/carbon interface has a critical influence on the performance of the anode assembly. This will be addressed in detail in the problematic.

1.3 Problematic

The aluminum production process requires an enormous amount of electrical power. A typical potline consists of several reduction cells (electrolysis cells) in series, operating at low voltage and high intensity. Electrical losses in each cell accumulate over the potline, increasing total power consumption. Many efforts are dedicated to finding ways to increase efficiency of all these parts and lower the potential drop and the energy loss. Many projects, carried out by researchers in different domains, are dedicated to this subject. Nevertheless, the focus in the author's project is the anode assembly's contribution to the total voltage drop of the reduction cell.

In the reduction process, the electric current flows to the cell through the busbar on its top. After passing through several parts and components of the anode assembly, bath and finally cathode, the current is finally conducted to the adjacent cell through the busbar. It is well known that the electric current loses its potential while it is conducted through these components. In figure 1.5, which illustrates a typical voltage break down of a reduction cell, it can be seen that the anode assembly also contributes to the total voltage drop.

It is given that materials have resistivity against the electrical current; thus, electrical potential drops as the current flows through anode assembly components. However, this is not the only phenomenon that causes resistance against the current in the anode assembly. Interfaces between components of the superior part can also act as a barrier against the current. These interfaces stem from the anode assembly manufacturing process of which the most important step is that between cast iron and carbon due to its remarkable impact on the total voltage drop in the anode assembly.

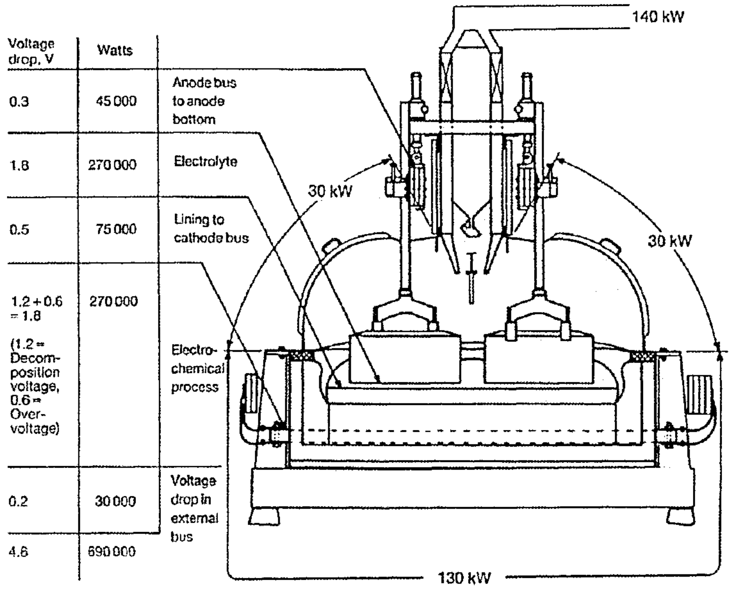

Voltage drop, V	Watts	
0.3	45 000	Anode bus to anode bottom
1.8	270 000	Electrolyte
0.5	75 000	Lining to cathode bus
1.2 + 0.6 = 1.8 (1.2 = Decomposition voltage, 0.6 = Overvoltage)	270 000	Electrochemical process
0.2	30 000	Voltage drop in external bus
4.6	690 000	

Figure 1.5: Typical voltage breakdown of a prebaked aluminum reduction cell at 150kA and 4.6 V [9]

After the solidification of cast iron in the rodding process, an air gap appears at the cast iron/carbon interface. The magnitude of the air gap varies depending on the rodding procedure, thermo-mechanical and thermo-physical properties of cast iron, as well as the geometry of the stub hole. The stubs and the carbon around the stub hole are preheated; steel stubs usually reach 250°C, whereas carbon does not exceed 150°C. This is mainly to make sure there is no moisture on the surfaces which are supposed to be in contact with the cast iron. Note that in some technologies preheating is not applied. After positioning the stubs into the stub holes, molten iron at approximately 1300°C is cast. At this point, heat is transferred at a high rate to the carbon and steel. Cast iron solidification starts around 1100°C by the exterior layers (surfaces in contact with carbon, cast iron an air) which cool down faster due to a higher rate of heat transfer to steel, carbon or air. Notice that heated carbon and steel expand and narrow down the total radial space between stub and carbon until the solidification of cast iron starts where the rate of cast iron cooling slows down and the thermal expansion of steel and carbon stops. Since solidification of the entirety of the cast iron does not happen at once, a metallurgical modification occurs during cooling which causes the cast iron to contract and enlarge the air gap between it and the carbon. It should be kept in mind that the structure of the cast iron depends on the rate of cooling and thus cannot be uniform in the connectors. This makes it difficult to determine the exact properties of cast iron and the initial air gap magnitude. The temperature of the materials in the stub hole region, while in operation, does not exceed 900°C. In this way, it is possible that the air gap cannot be filled up completely and thus, contact cannot be established uniformly on the entire exterior surface of cast iron.

The cast iron/carbon interface causes thermal and electrical **contact resistance** which plays a key role during aluminum smelting. Solid surfaces are not perfectly smooth, and once in contact, the two surfaces have real, atomic-level contact only at some points. These points are called contact points and are shown in figure 1.6. A constriction of electric flow occurs at the interface of two bodies in contact if they are conducting an electrical current. An example of such kind of constrictions is also demonstrated in figure 1.6. The current loses some of its potential (voltage) depending on the number of contact points, or, in other words, depending on the sum of the real contact areas. This phenomenon is known as contact resistance. Research has revealed for a long time now that contact resistance is a function of pressure and temperature (for detailed information refer to section 1.6.3). With increasing temperature or pressure, the interface between two surfaces in contact will impose less resistance. A similar phenomenon happens to the thermal flows passing through interfaces; but in this case, instead of voltage the temperature of the thermal flow drops. Electrical contact resistance is more critical than thermal contact resistance, since even though there is no contact between two surfaces of an interface, radiation makes it possible to transfer heat from one surface to another. Unlike the thermal flow, in the presence of an air gap and lack of any physical contact, there is no way to transfer the electrical flow from one surface to another. Notice that in the presence of moisture the current may go through the interface.

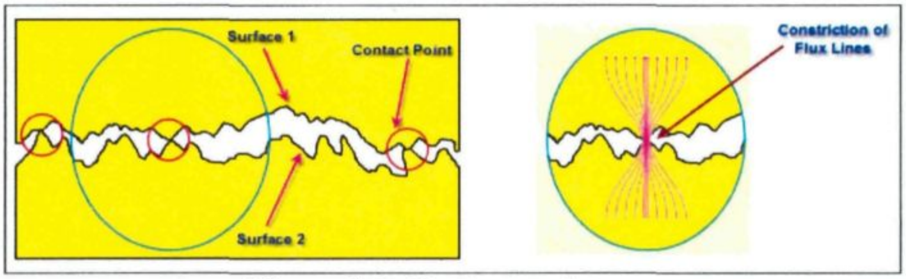

Figure 1.6: Contact resistance

Voltage drop in anode assembly is highly important since it is directly associated with production costs. A simple calculation of saving potential will signify the enormous credibility of the present work.

For RTA smelters, a very rough estimation of the potential amount of money to be saved save with only 3% optimization of the cast iron/carbon area assuming a total voltage drop of 80 mV at the cast iron to carbon interface yields 0.704 Million C$/year:

$$\begin{aligned} &0.08(\mathrm{V})\times 0.03\times 250(\mathrm{kA})\times 24\frac{\mathrm{hour}}{\mathrm{day}}\times 365\frac{\mathrm{day}}{\mathrm{year}} \\ &\times 3825(\mathrm{pots})\times 0.035\frac{\mathrm{CDN}}{\mathrm{kWh}} = 0.704 \end{aligned} \tag{1.2}$$

A very similar calculation for Quebec and Canada, assuming the number of pots to be 8904 and 9932 respectively, results in 1.64 and 1.83 Million C$/year.

That said, considering the voltage drop as a good index for evaluating the energy loss of the entire system seems reasonable. Up to 25% of the anodic voltage drop is attributed to the steel/cast iron/carbon area [5]. The rest of the anodic voltage drop (75%) occurs in the other parts of the anode assembly of which a great percentage is caused by the resistivity of the materials. Since there is not much that can be done to significantly reduce this resistivity, researchers' attention has turned to the steel/cast iron/carbon area due to the nature of energy loss in that area mostly contact resistance at the interfaces and not the material electrical resistivity.

Considering equation (1.1), theoretically it is expected that 1 kg of aluminum is produced by spending 6 kWh while actual energy consumption is between 12.5 kWh and 16 kWh. It simply means that in practice, in the best case scenario, the amount of energy loss is more than 50%. From an engineering point of view, it is not possible to attain an efficiency of 100% (for example, consider energy dissipation by the Joule effect which cannot be zero); there is, however, a lot of potential that can lower the energy loss and production costs.

As aforementioned, materials show resistivity against the electric current they are conducting. Potential loss occurs as the current flows through the conductor and the electrical energy is dissipated in the form of heat. This phenomenon is known as the **Joule effect**. It is impossible to conduct an electric current with no heat generation. In plain language, it is impossible to produce a solid material that has no resistance against the electric current. In the case of an anode assembly, even optimizing solid materials used in the superior part of the anode assembly cannot make a major difference in the performance of the reduction cell. Unlike these solid materials, interfaces can be highly resistant against the current. It should be borne in mind that cast iron is not assumed as a component of the superior part. Optimization of cast iron and steel properties can have an effect on the quality of contact; and thus, the total voltage drop. The fact that up to 25% of voltage drop occurs in the stub/cast iron/carbon area makes it a region that requires special consideration.

A reduction cell deals with many physical phenomena; thermal, chemical, electrical and mechanical are the most important ones in the aluminum production process. The solidified cast iron in the stub hole plays the role of a mechanical, thermal and electrical connection [5]. The reason that an air gap opens up at the cast iron/carbon interface in anode fabrication is that cast iron does not wet carbon [6]. The interface causes thermo-electro-mechanical (TEM) contact resistance which plays a key role during aluminum smelting. These phenomena are not independent of each other, and they are especially significantly coupled at the interfaces. Joule effect makes solid components expand due to generated heat. The expansion changes the contact condition at the interfaces so that if there was not any contact beforehand, contact may be established or, if there was already established contact, it may change its condition since contact pressure increases. Higher pressure allows more electrical and thermal flux to pass through since contact resistance at interfaces decreases. The more electric current passes, the more heat is generated and the more expansion occurs; consequently, the more pressure is applied at interfaces. In other words, with a higher current density, the Joule effect will make a more significant contribution to temperature increase.

According to the geometry of the stub hole and cast iron connector, the initial air gap between cast iron and carbon is not uniform. This has an impact on the contact condition while the anode assembly is in operation since the gap is not filled completely and uniformly during the heat up. A non-uniform contact at the interface can cause a different current density profile and different temperature distribution throughout the anode assembly, particularly in the stub hole area. Figure 1.7 illustrates how thermal, electrical and mechanical phenomena are coupled, as shown by Richard *et al.* [7].

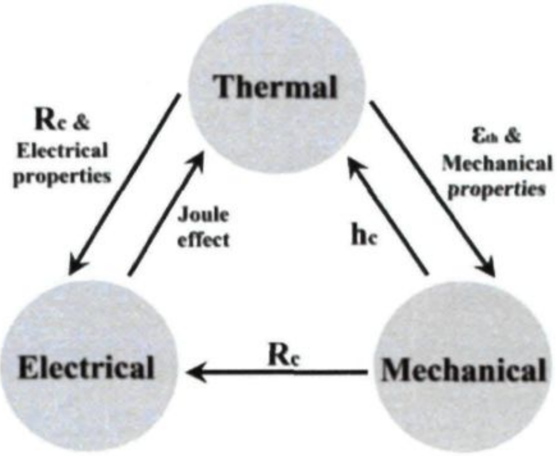

Figure 1.7: Interrelations among physical phenomena

Essentially voltage drop in anode assembly can originate from different sources. For example, ideally in the carbon anode, the only potential loss is caused by the material resistivity unless carbon anode fabrication was faulty and cracks or higher porosity existed in the carbon block, which impose more voltage drop. However, since the focus in this work has been cast iron/carbon interface such kind of sources will not be addressed in this document.

Apart from expansion, a change in TEM properties can change the behavior of the system e.g. with temperature dependent mechanical properties, the stiffness of the solids will vary with a change in the thermal flow since it causes a change in temperature. This is not only true for the materials but also for the interfaces too.

It is primarily conceived that applying higher pressure will solve the problem of dropping electrical potential at the interfaces. Considering the susceptibility of carbon to tensile stress, this option is off the table. Excessive pressure may cause critical mechanical stresses which consequently may cause damage or change the operation conditions. Like concrete, carbon is a quasi-brittle nonlinear material which behaves differently under compression and tension. Its susceptibility to cracking under tension may cause extreme loss of stiffness (damage). Less stiff (more flexible) carbon results in less contact pressure: thus, higher contact resistance and consequently, higher potential loss. In extreme cases, a part of carbon can be ripped apart from anode and fall into the molten and contaminate it. It is not only cracks in carbon that can cause loss of stiffness. Even in a good operating condition, since carbon participates in the chemical reaction to produce aluminum, the carbon volume decreases over time. As carbon is consumed and its volume is decreases day after day in its life span, it gets less stiff. Being less stiff, carbon will then be more likely to produce cracks. This can have an impact on the contact condition due to the change in the stiffness of carbon once it is exposed to tensile stress imposed by the expanding stub and cast iron connector in the stub hole. In addition, as the carbon is consumed and the anode is lowered, the temperature in the stub hole region increases. Such increase causes more thermal expansion in the stub and the cast iron connector which increases the risk of crack generation.

As a result of long term exposure to high levels of stress and temperature, creep can also have an influence on the global behavior of the anode assembly. Creep is more likely to take place in steel stubs and cast iron connectors since they are metallic components and they are subjected to intensive heat and stress for a long period of time. Also, they are more sensitive to creep than carbon. During operation they can easily reach or pass the temperatures equal to or greater than the half of their melting point. This fact increases probability of creep and then a decrease of the contact pressure causes voltage drop increase.

Taking this explanation into consideration, for lowering the anodic voltage drop and, consequently, production costs, a comprehensive study of the anode assembly, particularly its thermo-electro-mechanical behavior at interfaces as well as the change in the TEM behavior of the materials during the process is needed. To date, taking all the aspects necessary to study the behavior of the anode assembly into account has been challenging. Finding the key parameters to increase the quality of materials and the performance of the entire system in operation is a complicated process due to multiplicity of the parameters. To date, there has not been any work which has presented any robust numerical tool validated with the experimental and *in situ* results. In addition, up to now there has not been any has a rigorous approach which takes advantage of numerical modeling to better investigate the phenomena taking place in the anode assembly, particularly in the steel/cast iron/carbon area which allows optimization of design.

Given this lack, it is concluded that a proper and detailed study of the anode assembly, especially on the cast iron to carbon interface where a considerable percentage of the electrical energy is wasted and where there is an excellent chance to find and apply some technical and feasible ways to improve efficiency of the components during the smelting operation, is worthwhile.

1.4 Objectives

The main objective of this project is to achieve a better understanding of the thermo-electro-mechanical behavior of the anode assembly during aluminum smelting in order to identify the key parameters associated with the anodic voltage drop in the anode assembly; and more specifically, at the carbon to cast iron interface and propose realistic changes to the actual design in order to lower the voltage drop for the aluminum industry.

As a long term objective, the project will provide the aluminum industry with an efficient tool for the design of future anode assembly to reduce their energy consumption and thereby, the production costs.

1.5 Methodology

To fulfill the objectives of this project, a comprehensive study of the anode assembly, particularly the area stub/cast-iron/carbon, is needed, which requires the consideration of complex and coupled thermal, electrical and mechanical phenomena. This project deals with the development of a robust numerical tool and its validation using experimental results obtained by RTA. It is realized in three main steps:

In the **first step**, a robust parametric model will be developed using APDL. This model will enable us to change the geometry for different analyses easily. Optional conditions to mesh the geometry will be a case for the model which will provide different meshing sets to ensure the convergence of the results.

The **second step** mainly is about selecting constitutive laws, material properties and gathering and putting all experimental results together. To maximize the accuracy of the simulation results and building a robust numerical tool, realistic material properties or contact constitutive laws which were obtained through other projects carried out by other researchers working in the same field will be employed. This is ongoing work and as soon as more information is available, it can be implemented in the model to improve its efficiency.

The analysis (solving) process is the **third step**. A submodel (half block) will be extracted from the full model to be used for calibration and preliminary studies on the phenomena being dealt with, especially in the cast iron to carbon interface. The half block model will first be calibrated with the experimental data obtained from the industrial partner (RTA). The model that has the same geometry as the numerical model does is called Electrical Contact Furnace (ECF) model. Then it will be used to perform analyses to investigate the system in different ways. This will be an auspicious start to using the full model for more realistic and complex analyses simulating the real situation as closely as possible.

FESh++ will be used for this purpose. FESh++ is an object-oriented multi-physic finite element analysis toolbox. FESh++ supports the implementation of complex material constitutive laws, for instance for carbon-based materials, so it is extremely useful to carry out advanced research work [see 8]. To investigate the system, Sensitivity Analysis (SA) will be performed. SA is the study of how the variation (uncertainty) in the output of a mathematical model can be apportioned, qualitatively or quantitatively, to different sources of variation in the input of a model.

And, last but not least, the result obtained from the sensitivity analysis on the materials, geometry and operational conditions accomplished by the numerical tool will be a noticeable improvement to facilitate the optimization of the anode assembly. Note that some of such study will be covered within the framework of the author's research project and the remainder will be future work for other investigators.

1.6 Previous work

In this section, a brief review on the previous experimental, *in situ* and numerical work is presented to explain the level of complexity of investigating electrolysis process. Since contact interfaces play an important role in the electrolysis, and particularly at the cast iron/carbon interface in the anode assembly, mathematical models and experimental models for contact are briefly introduced. Finally, recent models of the anode assembly are presented.

1.6.1 Complexity of the problem at a glance

Over the past decades, several authors have studied the electrical losses in the stub hole, both *in situ* or experimentally [9,10,11,12] and using numerical models [13].Since electrolysis process to produce aluminum involves contact problems, the initial efforts were to better understand the contact resistance and propose mathematical constitutive laws to predict resistance at interfaces, particularly at the cast iron to carbon interface.

On the one hand, the experimental investigations did not lead to any practical means of predicting the losses in a configuration different than that tested. In his 1976 paper, Peterson [9] instrumented an anode with 30 voltage probes and 50 thermocouples. Temperature and potential readings were taken during 24 hours while the anode was in operation. It was found difficult to evaluate the cast iron/carbon electrical contact resistance; nonetheless, it was estimated that up to 25% of the anode voltage drop was attributed to the stub to carbon connection. It was also noticed that contact resistance seemed to decrease exponentially with temperature. In 1978, Peterson instrumented an anode with a different stub hole design and put in an oven. Once again, electrical contact resistance was difficult to evaluate, but it seemed to decrease to negligible values at high temperatures. In 1984, Brooks and Bullough [11] analyzed the impact of cast iron thickness on electrical contact resistance. They found out that both temperature and contact pressure influenced the resistance greatly and suggested design charts for cylindrical connectors. In 1989, Peterson *et al.* [12] also built charts for the optimum cast iron thickness, with similar results. However, it was still impossible to study the influence of the flutes or more complex stub hole geometries on the connector performance [14].

On the other hand, the limitation of the approach used in the numerical models of Hou *et al.* [13] did not allow any clear conclusion to be drawn. Indeed, the behavior of contact resistance at the interface was hypothetical. It was assumed constant and independent of pressure or temperature. Moreover, the cast iron connector was assumed to establish contact with carbon on its entire surface, which in reality might not be the case. These assumptions were a consequence of the purely thermo-electrical nature of those models: no mechanical run was made to evaluate the actual contact points (for contact points see figure 1.6) and their corresponding contact pressure. Furthermore, no experimental results were presented as a validation to the model's assumptions and results [14].

From all this, it can be concluded that the problem of contact resistance has not been easy to solve. The challenges over nearly four decades have resulted in some developments but still a lot of research into the behavior of contact resistance is needed. Numerical simulations validated by experimental measurements will be the best way to unravel this problem in its entirety. In addition, an accurate and reliable simulation of anode assembly, or any other part of the HH cell which deals with contact, requires a rigorous constitutive law for contact at interfaces.

1.6.2 Mathematical models of contact resistance

It is known today through previous work that contact resistance has a considerable impact on the voltage drop in the anode assembly [10]. With that being said, a proper mathematical (numerical) representation of contact resistance is crucial to obtaining reliable results from numerical models. In the past, several purely mathematical models have been presented. Also, several models have been presented through experimental work. In this section, only a compact review of the developed mathematical models of contact resistance is presented since the detailed study on the subject is beyond the scope of the project.

Many mathematical models have been suggested to represent contact resistance. The Cooper-Mikic-Yovanovitch model (CMY model), published in 1969 [15], is considered by several publications [7,16] as one of the best to predict thermal contact conductance correctly. A convenient form of contact conductance (h_c) was expressed by Yovanovitch, which is the result of a simplification [see 17] such that:

$$h_c = 2\frac{k_s n a}{\left(1-\frac{A_r}{A_a}\right)^{1.5}} \tag{1.3}$$

where A_r is the real contact area, in other words, the total area of the microscopic asperities actually in contact; A_a represents the apparent contact area, the area which seems to be in contact together; k_S is the harmonic mean thermal conductivity, calculated with the root mean square (rms) method; the contact spot density is represented by the symbol n; and finally, symbol a is the mean circular contact radius.

The expression of electrical contact resistance (R_c) can be obtained from equation (1.3) by equivalent expressions of h_c and k_s [see 18], which conducts to equation (1.4):

$$R_c = \frac{1}{h_c} = 0.8\rho_\epsilon \frac{\sigma}{m}\left(\frac{P}{H_c}\right)^{-0.95} \quad \textbf{(1.4)}$$

where σ represents the root mean square (rms) surface asperities height of the equivalent surface; m, the harmonic mean slope of the same equivalent surface, ρ_ϵ the harmonic mean electrical resistivity of the connecting materials, P the contact pressure and H_c, the microhardness of the softest surface, as presented in the CMY mode. As discussed by Yovanovitch and Sridhar [19], electrical contact resistance depends on the surface properties of the contacting bodies.

The CMY model was reviewed almost a quarter of century later and a model was developed by Mikic [20].The elastoplastic model of Yovanovitch, based on CMY surface model (EP-CMY), permits a comparison of theoretical predictions with elastic, elastoplastic and fully plastic deformations. The fractal model of Majumdar & Tien (Maj), developed by Majumdar and Tien [21],permits a description of irregular geometries. In fact, “fractal geometry is a mathematical tool that describes the structural disorder and chaos of a number of objects found in nature” [see 22 and 23]. The Majumdar and Tien fractal model was introduced in 1991 [24] and is based on a fractal representation of the surfaces, obtained from a Weierstrass–Mandelbrot generating function whose parameters are calibrated by comparing its power spectrum to that of the real surface’s profilometric data. The fractal model is built on a better surface representation, which allows an objective characterization of the contact surfaces; nevertheless, since both models rely on the same mechanical assumptions, the fractal model eventually takes on the same form as the CMY model [25].The CMY and the fractal model are based on the following key variables: surface roughness, surface hardness and contact pressure.

In the Greenwood-Williamson model (GW), the material properties and typographic properties influence the contact conductance h_c. Singer and Kshonze converted the contact conductance into an electrical resistance R_c. [see 26].

1.6.3 Experimental work on contact resistance

In situ and laboratory results were carried out in the seventies by Peterson on anodic cast iron connectors, with apparently contradictory conclusions. Later, Sørlie, Gran [27], Hiltmann *et al.* [28] studied contact of carbon and steel (or cast iron) cylinders in a hydraulic press fitted with a furnace allowing a wide range of pressure and temperatures to be achieved. A schematic of the setup is reproduced in figure 1.8. The cylinders were instrumented with voltage probes and thermocouples; a constant current was forced through the assembly and while the temperature was held constant, temperature and voltage were recorded as the pressure was slowly increased, then slowly decreased. This was repeated at five temperatures from ambient to around 1000 °C. Contact resistance was calculated by extrapolating the electrical potential from both sides of the interface [25].

Sørlie and Gran found that pressure and temperature influenced greatly contact resistance, but again, no constitutive law was proposed. Moreover, as discussed by Beck [29], this method of calculating contact resistance by extrapolation of the potential to the interface is prone to error. Indeed, it assumes a linear behavior of the potential, which might not be a good approximation when the location of the measuring probes is far from the contact surfaces, since thermal conductivity and electrical resistivity are temperature dependent and are different for carbon and cast iron [25].

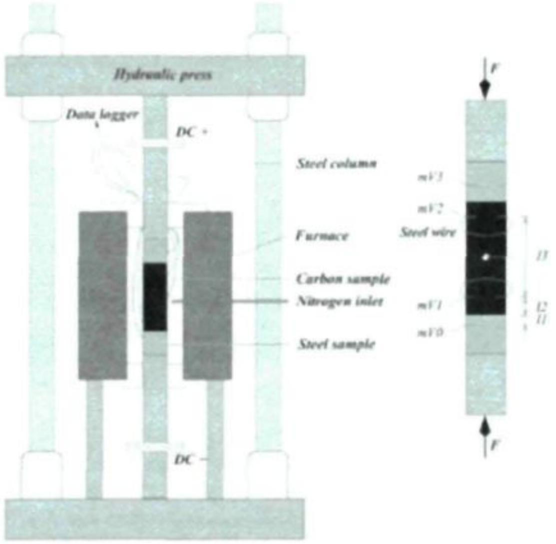

Figure 1.8: Sørlie and Gran experimental setup [25]

In 2000, Richard *et al.* [25, 14 repeated the experiment using anode material. Based on their experimental data, they proposed a constitutive law in the form of the Weibull equation and validated the results with data published by Brooks and Bullough [11]. The need to adequately represent the thermo-electro-mechanical influence of contact in the reality logically led the researchers to the development of a tool based on both theoretical fundamentals and experimental results.The phenomenological model developed by Richard [30] meets the need to adequately represent the thermo-electro-mechanical evolution of the anode connectors in an electrolytic cell. This model is based on experimental parameters obtained by Sørlie & Gran [27]. The most important assumption is the influence of the temperature and pressure on contact conductance and contact resistance. Equation (1.5) shows the general expression of the contact resistance suggested by Richard such that:

$$R_C(T,P) = A(T) - B(T)\exp\left(-\left(\frac{P}{C(T)}\right)^{D(T)}\right) \tag{1.5}$$

where R_c is contact resistance, P, contact pressure, and T, the mean surface temperature. Parameter C(T) can be seen as a ''hardness parameter'' to adimensionalize pressure, while D(T) could be interpreted as a ''fractal dimension'' related to surface roughness. Parameters A(T) and B(T) control the maximum value at very low adimensional pressure as well as the maximum value at very high adimensional pressure. The parameters temperature dependency was found to be well represented by equations (1.6) to (1.9) [25]:

$$A(T) = \exp\left(\frac{a_0 + a_1 T}{1 + a_2 T + a_3 T^2}\right) \tag{1.6}$$

$$B(T) = \exp\left(\frac{b_0 + b_1 T}{1 + b_2 T + b_3 T^2}\right) \tag{1.7}$$

$$C(T) = c_0 + c_1 T \tag{1.8}$$

$$D(T) = d_0 + d_1 T \tag{1.9}$$

The twelve parameters shown in the above equations are calculated by reverse engineering. The calibration was different for rough and smooth interfaces. By extrapolation of experimental results, Richard succeeded in obtaining an expression for the electrical resistance covering the temperature range of the sealing of anodic connectors.

In 2006, Kiss *et al.* published their results of experimental measurements [31, 32]. They used a very similar setup (figure 1.9) to that of Sørlie and Gran except they determined both thermal and electrical contact resistance at the same time.

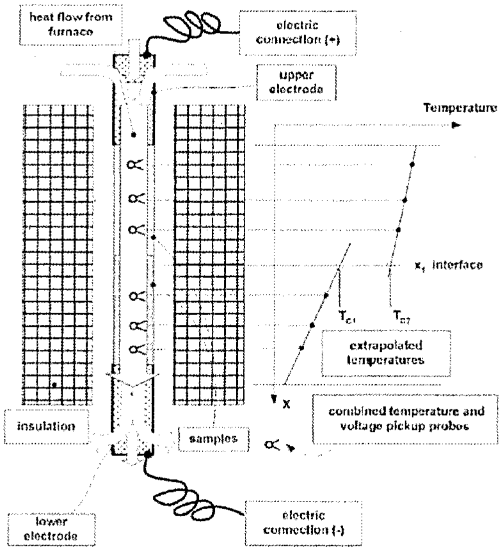

Figure 1.9: Measurement principle [31]

Their experimental results covered a wide range of temperature and pressure. Another interesting feature of their work was the use of samples that had naturally shaped surface micro geometry and the same microstructure as in certain applications [see 14]. Rouleau's proposed constitutive law for contact resistance, which is presented in equation (1.10), was employed in this work.

$$R_E(P,T) = C_1(T)\,P^{C_2(T)} \qquad \textbf{(1.10)}$$

In the aforementioned equation R_E is electrical contact resistance and P is contact pressure. C_1 and C_2 are the coefficients to be determined and assumed to be temperature dependent. The results of the measurements revealed that both electrical and thermal contact resistance are temperature and pressure dependent. Figure 1.10 illustrates a comparison of these results and theoretical models. The higher values of the experimentally obtained contact resistance compared to the theoretical models show either the possible effect of "naturally" shaped surfaces versus machined ones, or the relatively false model assumptions of clean and conform surfaces (surfaces with uniform distribution of asperities) [31].

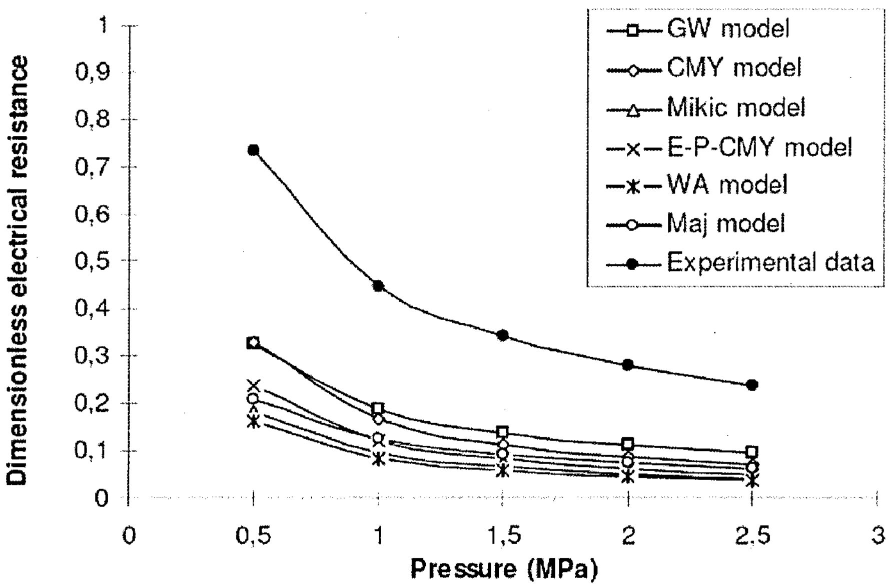

Figure 1.10: Electrical and thermal prediction models compared to experimental data [31]

In 2007, Wilkening and Côté [33] published the results of measurements of electrical resistivity, thermal conductivity and thermal expansion as a function of temperature for the three critical materials in the anode assembly, namely steel, cast iron and carbon. Phase transition (phase change) was addressed in their work. Kandev and Fortin also addressed phase transition, particularly in their work presented in 2009 [34].

In 2009, St-Georges *et al.* measured the coefficient of friction between the two solids in the same condition as the ones used for the measurement of contact resistance [see 35]. The coefficient of friction plays an important role in sliding contact problems.

Kandev *et al.* [36] introduced their new apparatus, shown in figure 1.11, to characterize ECR (Electrical Contact Resistance) and thermal contact resistance in their paper published in 2011. Instead of commonly used convection, they employed electrical induction heating to generate heat. The main advantage of the new apparatus is that temperature equilibrium of the samples can be reached very quickly (within two or three hours) while controlling the heat flux [36].

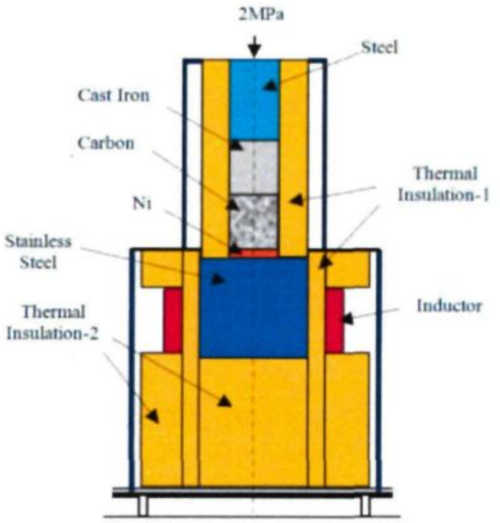

Figure 1.11: Simplified schema of Kandev et al. setup [36]

1.6.4 Recent numerical models of anode assembly

The first efforts to build a model to solve the problems of aluminum production process go back to 1980s [see 37]. It was in 1984 that the first 3D model was built using ANSYS$^{®}$: a thermo-electric half anode model. There has been a positive tendency in the recent years to work much more on the anode assembly, especially the cast iron connector and stub hole redesign since the experimental measurements in conjunction with numerical models have shown that this region in the anode assembly is critical and prone to wasting a lot of energy due to the interaction between interfaces and contact resistance.

There have been several research projects done recently to reduce the voltage drop in the anode assembly through different approaches like stub hole redesign; nevertheless, most of them could not simulate the anode system and reduction process adequately due to many geometrical simplifications and lack of consideration of the thermal, electrical and mechanical phenomena simultaneously. These projects are briefly described below.

Richard was the first to develop an ANSYS® based TEM anode stub hole model [30,38]. Unfortunately, the ANSYS® version available at the time did not support thermo-electro-mechanical contact elements and thus preventing the development of a fully coupled model. In their paper in 2001 [see 14] Richard *et al.* published their conclusions based on the results of their simulation. They stated that some reduction in losses could be achieved without increasing the cast iron mass; greater savings were possible by increasing the cast iron volume significantly, which involves the reduction of rodding productivity. He also mentioned that the problem was highly nonlinear that no general conclusion on stub hole design could be made. He concluded that a better understanding of the carbon behavior, cracking prediction and prevention, a strong thermo-electro-mechanical coupling allowing transient simulation and accounting joule heating effects, a detailed geometry modeling and a better way to predict the air gap between cast iron and carbon would improve the reliability of the model.

Following Richard's initial effort, Goulet developed a fully coupled TEM contact model based on the in-house Object-Oriented finite element code FESh++ [39,40]. ANSYS® has been the code of choice of the industry for over 25 years now [38]. However, in spite of much improvement in ANSYS® in the recent years, it still remains difficult to effectively simulate fully coupled TEM contact problems in ANSYS® using temperature-pressure electrical contact resistance dependency.

In 2009, four models were presented at the TMS conference. Kandev and Fortin presented a thermo-electrical model and indicated that it appeared that the fully coupled TEM anode model with displacement and Joule heat effect had not been solved to that date. Their goal was to examine general electrical and thermal field distributions in the stub anode connection and to validate the agreement between the experimental results and the simulation, in preparation for the completion of the 3D TEM anode model [see 34]. Their model, which is shown in figure 1.12, was a simplified TE numerical model and could not be used for stub hole design optimization or interface gap analysis. Finally the suggested idea was to use a protective electro-conductive collar (cast iron or other material) around the stub. Their simulation results showed that in using such a collar, the current density in the stub was more homogenous; therefore, the electrical losses decrease. They estimated a reduction of the anode Joule losses about 6% was possible by using such a collar.

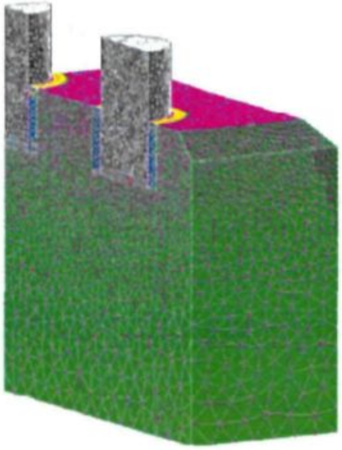

Figure 1.12: Finite element anode model- quarter of domain with stubs and mesh distribution, presented by Kandev and Fortin [34]

Figure 1.13 illustrates the model presented by Fortin *et al.* which was a 3D TEM anode model to determine the effect of flute design, cast iron composition or tripod geometry on voltage drop and the effect of stub diameter changes in tripod steel stubs used in AP-30 technology operating at a current of 330 kA. In their paper published in the TMS 2009 [see 40], it was mentioned that the dominant parameter affecting the anode is the initial cast iron/carbon gap and that its initial magnitude is a problem to determine. The authors used the law taken by Richard in which the air gap is calculated as a function of steel radius. In the presented paper, the results showed a variation of about 3% on the voltage drop for the 160 mm diameter configuration compared to the 180 mm diameter one.

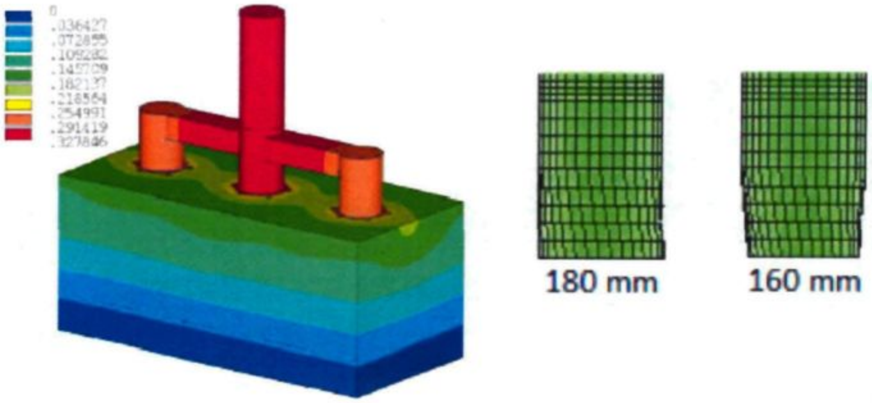

Figure 1.13: Anode assembly model and tested stub diameters presented by Fortin *et al.* [40]

Li *et al.* presented a very simplified TE model shown in figure 1.14 and used it to determine the anode voltage drop and consider possible design modifications to lower the anode voltage drop. The influences of anode carbon block height, yoke dimensions, number of stubs and stub diameter were analyzed [see 41]. They stated that the voltage drop of carbon anode is proportional to the height of the anode and has a linear relationship with the electricity consumption. The optimum anode height should be evaluated by anode price, electricity price, anode consumption per ton of aluminum and electricity consumption per ton of aluminum. Concerning yoke, they concluded that the yoke is a good heat modulator for the cell energy equilibrium. Their analysis of the number of stubs showed that the total anode voltage drop decreases with an increasing number of stubs. Moreover, the electric potential is evenly distributed in carbon with 5 stubs than with 4 stubs and 3 stubs; however, when too many stubs are used, the risk of cracking increases since the carbon cannot bear the excessive pressure caused by the expansion of stubs. Note that the impression is that the diameter of the stub holes remains constant.

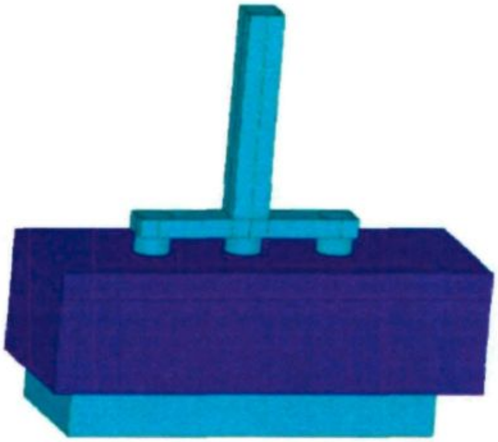

Figure 1.14: Parametric thermo-electrical model of Li *et al.* [41]

The fourth model presented in TMS 2009 was by Richard *et al.*, which tried to investigate the impact of number of flutes on the voltage drop. Their analysis showed that the 16 flute cast iron connector resulted in a slightly higher voltage drop compared to the 6 flute case. They concluded that the quality of contact decreases with the distance from the stubs.

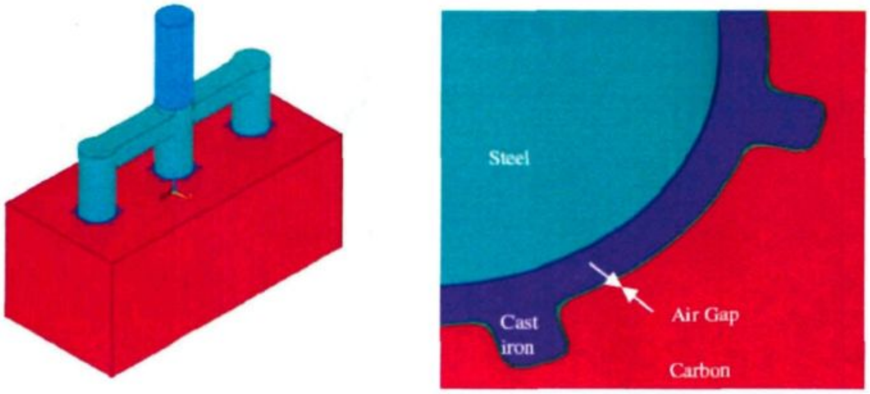

Figure 1.15: Simplified anode assembly model and stub to carbon detail presented by Richard *et al.* [5]

Traditional ways of increasing (apparent) surface area in fluted designs, like adding flutes, increasing their length or their width, result in a larger mean diameter and a larger mean contact resistance. Minimization of the stub-to-carbon voltage drop is therefore a balancing act between the real contact area and the resulting electrical contact resistance [see 5].

In 2010, Dupuis presented his model as an ANSYS® based TEM anode stub hole design tool. Using his tool he stated that when comparing the results obtained for the two 16 flute cases, according the TEM model with the proper pressure and temperature dependent contact resistance setup, a very slight change in the flutes' design aiming at increasing contact pressure of the flutes side faces should decrease the anode voltage drop by 17 mV, or 5.9% [38].

Similar to their paper published in TMS 2009 (see 40), Fortin *et al.* presented a paper in 2012 (see 42) addressing the influence of the stub diameter (shape) change (see figure 1.16), due to chemical attacks, on the voltage drop. Using their weakly coupled TEM model of an AP-30 technology anode assembly, developed in ANSYS® and solved with FESh++, several simulations were performed whose results were used to carry out a two-level factorial analysis. Results indicated that the main parameter influencing voltage drop is the outer stubs. In terms of energy efficiency, they concluded that a 10 mV increase in the voltage drop occurs in the tripod anode assemblies when a 180 mm stub diameter is reduced to a 160 mm deteriorated diameter. This results in 7.2 GWh of annual energy loss for hypothetical smelters using 250 cells operating at 330kA.

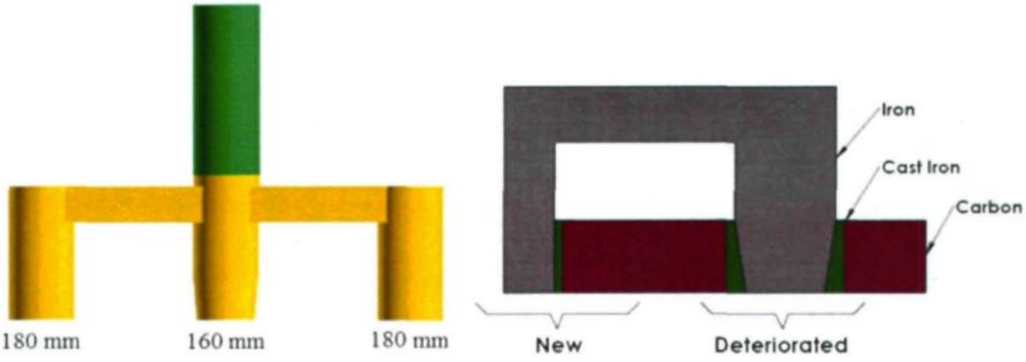

Figure 1.16: Anode assembly model to investigate deteriorated stubs influence on the anodic voltage drop presented by Fortin *et al.* [42]

These findings show that modeling a realistic anode assembly has thus far been challenging. All of the models presented to date have considered a perfect and theoretical geometry especially for the cast iron connector, while in reality there can be several types of defects such as: cold shut, pancake formation and/or stub malpositioning into stub hole. These defects can have considerable impacts on the behavior of the system e.g. stub malpositioning into stub hole, results in variable connector wall thickness; which, consequently, leads to different contact distribution. All of the models presented thus far have been simulating a brand new carbon while carbon is consumed during its 20-30 day lifespan to produce aluminum, and therefore, the behavior of the system can change accordingly. Nobody to date has presented a model that predicts cracking. Thus, a model encompassing even some of the aforementioned aspects will be a powerful tool to examine the anode assembly under different conditions to find the key parameters that will finally help us to decrease the voltage drop.

1.7 Originality and contents of the thesis

1. This project contains several novel characteristics especially in terms of geometrical modeling. A hexapod anode assembly was modeled for the first time. Hexapod

> assemblies have more complex geometries compared to other types such as tetrapod or tripod assemblies. The model is least simplified in terms of geometrical modeling, which is not seen in the previous models presented. Also, the model is fully parametric in terms of dimensions and mesh. Furthermore, the full anode assembly model has several features presented for the first time such as: pancake formation, carbon consumption, malpositioning of stub into stub hole, stub hole design tool (flutes shape and numbers[3]). Coupling of the thermal, electrical and mechanical fields is extensive compared to the previous work.

The present thesis consists of five chapters which will adequately address the effort dedicated to developing the numerical model of the full anode assembly and the results and findings using the half block model.

In Chapter 2, the physics of the problem is briefly addressed. Then, the mathematical governing equations of all thermal, electrical and mechanical contact problems are described. Also explained is how they are coupled and solved.

Chapter 3 deals with the finite element model. After explaining the geometry of the full anode assembly model and its features, the half block model is explained. All interfaces and contact that take place in the half block model are itemized. Material properties and boundary conditions as well as mesh composition and load steps of the simulations are elaborated afterwards. Finally, there is a thorough description of the initial air gap implementation.

Analysis is detailed in Chapter 4, which contains all of the steps to calibrate the half block model and the results of the calibrated model as well. In sensitivity analysis section all of the results obtained from the simulations to evaluate the sensitivity of the model to various parameters are presented.

Chapter 5 deals with the conclusions drawn from the simulations and results of the analyses. Finally, recommendations are presented for future work to continue this research.

---

[3] Flute numbers have been presented by other investigators in the past

The confidential version of this thesis comprises seven appendices containing detailed information especially on the results plots with original values (not scaled), material and contact properties, and parameterization.

CHAPTER 2:
MATHEMATICAL MODELING

2.1 General points

This chapter presents governing equations of the TEM problem required for finite element discretization. Study of the anode assembly in operation involves taking account of complex physical phenomena and their interrelations. As previously mentioned, many components of the anode assembly involve TEM phenomena; however, some of them deal only with one or two of them e.g. TE, TM. The separate solving of these three phenomena is now relatively well known; nonetheless, the interaction among them requires special attention.

The purpose of this chapter is to present the thermal, electrical and mechanical concepts and the terms of couplings among them. The derivation of the weak form of the governing equations will provide the necessary expressions to solve the problem by the finite element method.

Equations presented in this chapter have been drawn from the thesis of P. Goulet [see 39]. Equations described in this chapter are only the necessary ones to express the TEM balance in the context of this study. Thus, the reader is referred to his work for more details. Before proceeding into discussing mathematical formulations, however, the physics of the problem in question is reviewed.

2.2 Physics of the problem

A review of how a cell reaches its operating condition after the start-up with a focus only on the anode assembly and particularly on the stub hole region will be useful in better understanding the impacts of the influencing phenomena and their interrelations.

Supplying a very high electric current to the cell, through busbar, causes heat inside the components as well as at the interfaces which conduct the electric current. As previously stated, this is known as the Joule effect. In fact, the temperature dependent resistivity of the materials transforms electrical energy into thermal energy. The components of the anode assembly, which are solid materials, have a tendency to deform in response to the change in temperature due to the heat generated by the Joule effect. This change is simply called thermal expansion. That said, the thermal expansion of the solids will be different depending on their coefficient of thermal expansion (CTE).

In table 2.1, which briefly elaborates how TEM phenomena are coupled, thermal expansion has been noted as the impact of the thermal phenomenon on the mechanical one where α, the coefficient of thermal expansion can be a function of temperature. The CTE measures the fractional change in size per degree change in temperature at a constant pressure. Once an anode assembly is set to operation, only a few contact points facilitate the conduction of the electric current at the cast iron to carbon interface. Hence, temperature and pressure dependent contact resistance, imposed at the interface, is extremely high once the anode assembly is set to operation. In plain language, the accumulated contact area, which is the sum of areas of all the contact points, is too small compared to the total area. Temperature and pressure dependency of contact resistance, in terms of coupling, shows itself in different places in table 2.1.

The gradual increase in the temperature of the solids causing the thermal expansion changes the contact condition at the cast iron/carbon interface. The air gap at the interface is gradually filled up and more contact points are generated; and consequently, it lowers contact resistance since the real contact area increases. Thermal expansion increases contact pressure where the air gap is fully closed up. An increasing contact pressure at a point decreases contact resistance at that point (for a certain level of pressure). Notice that the decrease in the voltage drop at the interface depends on the geometry of the stub hole too. Typically, the thickness of cast iron at the lower part of the connector is smaller than that at the higher part; and thus, the resultant initial air gap is smaller in magnitude at the lower part when compared to the higher part. Therefore, generally, the air gap is initially filled up at the lower part and it evolves to the higher part. It is not guaranteed that the interface will be closed entirely. As for the cast iron/carbon interface, together with an elevated temperature and pressure, contact resistance decreases. Apart from that, an increase in temperature changes the material and interface properties of the solids, such as electrical or mechanical properties, as well.

It is not only the CTE that can change with a changing temperature. Mechanical properties, such as Young's modulus or Poisson's ratio, can also change with varying temperature. Having less contact resistance compared to the initial temperature and contact condition at the operation start, more electric current can be drawn, and the current density as well as its distribution in the stub hole region changes. With a higher current, more heat is generated and this process continues until it reaches an almost steady state condition.

The term "an almost steady state" has been used above, since after reaching the typical operating conditions, carbon starts to be consumed to reduce alumina to aluminum. To keep the carbon block partially immersed in the bath which has reached 960°C at the operation condition, it needs to be lowered gradually. The bath acts as a source of heat at a constant temperature, and therefore, the temperature of the stub hole region increases as it gets closer and closer (due to lowering) to the bath during its lifetime. However, the lifetime of carbon is long enough to consider the temperature increase caused by lowering of the carbon block negligible for a short period of time.

A carbon block's lifetime consists of two periods: start-up and operation. In practice it takes 12 to 36 hours for an anode assembly is set to operation. During this period, while the temperature of the anode assembly rises gradually, voltage drop decreases until it reaches an almost steady state condition (operational condition). Usually the lifetime of a brand new carbon block is approximately 20-30 days depending on the technology. Comparing these two periods of time (operation and start-up) it is clear that that the major part of the overall energy loss occurs during the operation period. Thus, neglecting the start-up (transient) period and solving the steady state problem solely, is a good approach to evaluating the performance of the anode assembly during the lifetime of carbon.

There can be other reasons that can perturb the balance between the thermal, electrical and mechanical phenomena. For instance, if a problem occurs in the adjacent anodes (in the same cell) which suddenly changes potential loss, the balance can be perturbed. As another example, a crack propagation, in the region close to the stub hole, leading to a sudden loss of contact at the cast iron/carbon interface or dropping a part of carbon into bath can perturb the TEM balance at the interface.

Before going through the mathematical definitions of the TEM phenomena and their coupling in the following sections, the summary of the impacts of all of these phenomena on each other in the anode assembly, particularly in the stub hole region, can be reviewed in table 2.1. Earlier in this document figure 1.7 was presented which schematically described TEM coupling.

Table 2.1: Description of TEM coupling

	On Thermal	On Electrical	On Mechanical
Impact of Thermal	$-k(T)\cdot\nabla T$ $h_c(T)$ $h_{conv+rad}(T)$	$R_c(T)$ $R(T)$	$E(T)$ $\nu(T)$ $\alpha(T)\Delta T$
Impact of Electrical	Joule effect $R(T)$ $R_c(T)$	$-G(T)\nabla V$	No impact
Impact of Mechanical	$h_c(P)$	$R_c(P)$	$H(T)\cdot\epsilon(u)$

In the prior table, k, h, R, E, ν, G, H, ϵ are thermal conductivity, thermal conductance coefficient, electrical resistance, Young's modulus, Poisson's ratio, electrical conductivity, stiffness respectively. $\alpha(T)\Delta T$ represents thermal expansion; subscript "c" stands for contact. P, T and V as function variables in the presented parameters represent pressure, temperature and voltage respectively.

2.3 Description of the electrical problem

In general, the word "electricity" refers to a number of physical effects such as: electric charge, electric current, electric field, electric potential and electromagnetism. Electric charge is a physical property of matter which makes it experience a force when near other electrically charged materials. The SI unit of electric charge is the coulomb (C). Electric current is the movement or flow of electrically charged particles, typically measured in amperes (A). The total electric charge of an isolated system (control volume) remains constant regardless of changes within the system itself. Considering that the current is continuous in the anode assembly (even more generally in the reduction cell), the conservation of electric current gives the result:

$$I_g + I_{in} - I_{out} = I_{st} \tag{2.1}$$

where I_{in}, I_{out}, I_g, I_{st} are the current that enters the control volume, current that leaves, generated and stored current.

Since it is assumed that there is no current generation in the anode assembly; and also, there is no current stored in the anode assembly, equation (2.1) can be simplified to:

$$I_{in} - I_{out} = 0 \tag{2.2}$$

By expressing the balance on the differential element $d\omega$ of the computational domain ω , presented in figure 2.1, one finds the continuity equation such that:

$$\nabla \cdot \mathbf{j} = 0 \tag{2.3}$$

where $\mathbf{j}$ is the current density vector on the differential element. For a constant current, the spatial distribution of $\mathbf{j}$ does not depend on time. The electric field inside a medium through which a current passes satisfies the equation:

$$\nabla \times \mathbf{E} = 0 \qquad \textbf{(2.4)}$$

where $\mathbf{E}$ represents the gradient of electric potential such that:

$$\mathbf{E} = -\nabla \mathrm{V} \qquad \textbf{(2.5)}$$

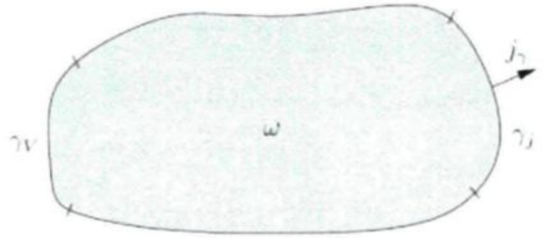

Figure 2.1: Computational domain of the electrical problem [39]

Ohm's law expresses the relation between the current density $\mathbf{j}$ and the electric field $\mathbf{E}$. This relation depends on the material properties of conductors:

$$\mathbf{j} = \mathbf{G}(\mathrm{T})\mathbf{E} \qquad \textbf{(2.6)}$$

with $\mathbf{G}(\mathrm{T})$ being the electrical conductivity of the material which is a function of temperature. Considering continuity law, it can be written as:

$$\nabla \cdot (\mathbf{G}(\mathrm{T})\nabla \mathrm{V}) = 0 \qquad \textbf{(2.7)}$$

The variation of electrical resistivity (inverse of conductivity) with respect to temperature is the only parameter affecting the balance of the system. The slightest variation in the electric potential results in an instantaneous response of the system. Moreover, the system should satisfy both Dirichlet (Essential) and Neumann (Natural) boundary conditions (BCs):

$$V\Big|_{\gamma_V} = V_\gamma \tag{2.8}$$

$$\mathbf{G}\frac{\partial V}{\partial n}\bigg|_{\gamma_j} = \mathbf{j}\cdot\mathbf{n} = j_\gamma \tag{2.9}$$

Equation (2.8) represents potential imposed on a portion of the boundary γ_V as the Dirichlet or Essential BC. Given in equation (2.9) a fixed current density j_γ, shown in figure 2.1, was described on a portion of the domain γ_j representing Neumann or Natural BC. $\mathbf{n}$ is the unit normal vector on the boundary surface. By applying the method of weighted residuals on equation (2.7), the weak form of the electric equilibrium equation at time t on the field w is obtained:

$$W_E = \int_{\omega} \delta V(\nabla\cdot(\mathbf{G}(T)\nabla V)d\omega = 0 \tag{2.10}$$

In order to obtain the boundary conditions as presented above, integration by parts is performed on equation (2.10), which yields the weak form expression such that:

$$W_E = -\int_{\omega}(\nabla\delta V)^T((\mathbf{G}(T)\nabla V)d\omega + \int_{\gamma_V}\delta V(\mathbf{G}(T)\nabla V)\cdot\mathbf{n}d\gamma + \int_{\gamma_j}\delta V(\mathbf{G}(T)\nabla V)\cdot\mathbf{n}d\gamma = 0 \tag{2.11}$$

Knowing that the electrical potential imposed on the boundary γ_V is V, there will not be any variation of potential on that boundary: δV will be equal to zero; and thus, the entire term of integral on the boundary can be eliminated. Substituting these values in the weak formulation (2.11), and considering equation (2.9), the equation of electrical equilibrium becomes:

$$W_E = -\int_{\omega} (\nabla \delta V)^T (\mathbf{G}(T) \nabla V) d\omega - \int_{\gamma_j} \delta V j_\gamma d\gamma = 0 \quad \textbf{(2.12)}$$

The integral on the boundary γ_j encompasses γ_s, the portion of the boundary where the current density j_s is imposed. Furthermore, in case of two solids in contact, it includes γ_c, the portion of the boundary where the continuity of the current j_c is applied. Thus, the integration on the contact boundary will provide a contribution such that:

$$W_{Ec} = -\int_{\gamma_C} \delta V j_c d\gamma \quad \textbf{(2.13)}$$

The conservation of electric charge requires the continuity of the normal current density in the vicinity of the contact points. It is simply enough to know the potential in order to calculate the potential loss at the interface due to contact resistance. Electric current loses its potential while passing through the interface; however, as per the law of conservation of energy, the same amount of dissipated electrical energy is transformed into thermal form. This is what it is known as Joule effect. The generated heat through the Joule effect becomes a course of volumetric energy q_V for the thermal problem and is given by:

$$q_V(T,V) = \mathbf{j}^T \rho_e(T) \mathbf{j} = (\mathbf{G}(T)\nabla V)^T \mathbf{G}(T)^{-1} \mathbf{G}(T) \nabla V = (\nabla V)^T \mathbf{G}(T) \nabla V \quad \textbf{(2.14)}$$

where $\rho_e(T)$ is the electrical resistivity of the material. Knowing the energy brought into the system is electrical, the resistivity of materials and resistance at interfaces transform partially this energy into heat.

2.4 Description of the thermal problem

Heat transfer is governed by the following law of conservation of energy, applied to the control volume:

$$\dot{E}_{in} - \dot{E}_{out} + \dot{E}_{g} = \dot{E}_{st} \tag{2.15}$$

where $\dot{E}_{in}$, $\dot{E}_{out}$, $\dot{E}_{g}$ and $\dot{E}_{st}$ represent respectively the rate of energy entering the control volume, leaving the control volume, generated in the control volume and stored in the control volume.

The terms $\dot{E}_{in}$ and $\dot{E}_{out}$ are surface phenomena as they are proportional to the surface area of the control volume and are involved with all three means of heat transfer, meaning conduction, convection and radiation in a normal situation. The term $\dot{E}_{g}$ (energy generation) is associated with the conversion of another form of energy (electrical, chemical, electromagnetic or nuclear) into thermal energy. It is a volumetric phenomenon that occurs inside the control volume; and therefore, proportional to its magnitude. In our specific context, the term of rate of generated energy can be replaced by the dissipation of electrical energy by the Joule effect $q_V(T,V)$. The term of stored energy is a volumetric phenomenon which is correlated to density ρ and heat capacity C_p which are functions of temperature. It is also related to the change in the internal energy of the system. If the material does not include change phase, the effect of latent energy is negligible. By applying the law of conservation on a differential control volume $d\omega$, the following equation can be found for a continuum medium:

$$-\nabla \cdot \mathbf{q} + q_V(T,V) = \rho C_P(T)\dot{T} \tag{2.16}$$

where heat flux, **q**, is obtained through the Fourier's law:

$$\mathbf{q} = -\mathbf{k}(\mathrm{T})\nabla \mathrm{T} \tag{2.17}$$

where **k** is the thermal conductivity of material and a function of temperature. Substituting equation (2.17) in equation (2.16) will give the following equation which is valid for all of the points of the domain ω, presented in figure 2.2:

$$\nabla \cdot (\mathbf{k}(\mathrm{T})\nabla \mathrm{T}) + \mathrm{q}_{\mathrm{V}}(\mathrm{T}, \mathrm{V}) = \rho \mathrm{C}_{\mathrm{P}}(\mathrm{T})\dot{\mathrm{T}} \tag{2.18}$$

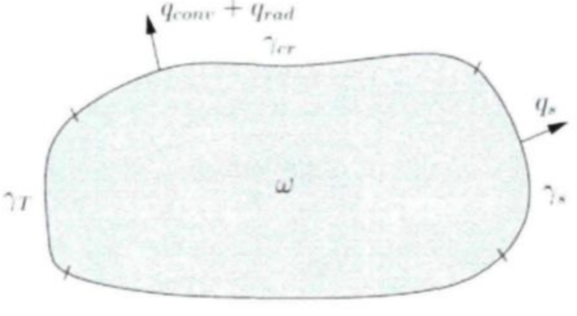

Figure 2.2: Computational domain of the thermal problem [39]

The right hand side of the equation will be equal to zero in case of steady state problems since the rate of change of temperature with respect to time will be zero. This equation must satisfy the Dirichlet boundary conditions, which is a temperature applied on the portion γ_{T} and Neumann boundary conditions, which is a heat flux applied on the portion γ_{q} of the domain ω such that:

$$\mathrm{T}\,|_{\gamma_{\mathrm{T}}} = \mathrm{T}_{\gamma} \tag{2.19}$$

$$-\mathbf{k}(\mathrm{T})\frac{\partial \mathrm{T}}{\partial \mathrm{n}}\bigg|_{\gamma_{\mathrm{q}}} = \mathbf{q} \cdot \mathbf{n} = \mathrm{q}_{\gamma} \tag{2.20}$$

By applying the method of weighted residuals on equation (2.16), the variational form of W_T equilibrium equation of energy rate at time t on the domain ω, shown in figure 2.2, is obtained:

$$W_T = \int_{\omega} \delta T(\nabla \cdot (\mathbf{k}(T)\nabla T) + q_V(T,V))d\omega = 0 \tag{2.21}$$

By applying integration by parts on the first term of (2.21) can be rewritten as its weak form so that the boundary conditions can also be shown in the equation such that:

$$\begin{aligned} W_T = &-\int_{\omega} (\nabla \delta T)^T \mathbf{k}(T)\nabla T d\omega + \int_{\gamma_T} \delta T \mathbf{k}(T)\nabla T \cdot \mathbf{n} d\gamma + \int_{\gamma_q} \delta T\, k(T)\nabla T \cdot \mathbf{n} d\gamma \\ &+ \int_{\omega} \delta T q_V(T,V) d\omega = 0 \end{aligned} \tag{2.22}$$

The first integration term is the contribution generated through the internal heat transfer (medium is the solid materials/components of the anode assembly in this case). The second integration term is on a portion of the boundary where temperature T is prescribed; and thus, the variation of temperature (δT) and, consequently, the second integral becomes zero. The third integration term is associated with the contributions of the thermal flows on the boundary. These flows can be convective and/or radiative or through exchanges with another solid via a contact interface. Finally, the Joule effect in the solid is represented in the fourth integration term.

The condition of flux in equation (2.20) can be of various types and encompasses all of the external contribution of surface to the energy input to the continuous medium. Hence, it is suitable to divide the boundary γ_q (on which the fluxes are applied) based on the applied source on the surface. The first of these zones (portions) will be γ_s to which a flux q_s is applied. The second portion is devoted to the convective (q_{conv}) and/or radiative (

q_{rad}) heat transfer with the surrounding environment. These two types of heat transfer can be assembled to have a single flux (q_{cr}) on the subdomain γ_{cr} which allows us to write:

$$W_T = -\int_{\omega} (\nabla \delta T)^T \mathbf{k}(T) \nabla T d\omega - \int_{\gamma_S} \delta T q_s d\gamma - \int_{\gamma_{cr}} \delta T (q_{conv} + q_{rad})\, d\gamma \\ + \int_{\omega} \delta T q_V (T, V) d\omega = 0 \tag{2.23}$$

where

$$q_{conv} = h_{conv}(T)(T - T_\infty) \tag{2.24}$$

$$q_{rad} = h_{rad}(T)(T - T_r) \tag{2.25}$$

h_{conv} is the coefficient of convective heat transfer and is a function of temperature, material properties and type of flow. According to the definition of the thermal convection and radiation, T, T_∞ and T_r are the temperature of the surface, the temperature of the surrounding fluid and the temperature of the radiation source respectively. The coefficient of radiation h_{rad} is defined as below:

$$h_{rad} = F \epsilon \sigma_{rad} (T + T_r)(T^2 + T_r{}^2) \tag{2.26}$$

As equation (2.26), demonstrates, the coefficient of radiation, in addition to its dependency on temperature, depends on parameters such as view factor F, surface emissivity ϵ and Stephan-Boltzmann constant σ_{rad}.

All of these parameters in addition to temperature dependency of the coefficient of radiation makes it complex to calculate temperature distribution since the problem becomes nonlinear. In this context, a simplified expression for the coefficient of radiation can be written as:

$$h_{rad} = \frac{\epsilon\sigma_{rad}(T^4 - T_\infty{}^4)}{(T - T_\infty)} \tag{2.27}$$

Since it is considered that cast iron and carbon will be in contact in anode assembly, it is necessary to add a contribution W_{Tc} on the portion of contact γ_C (boundary at which contact is established) of surface boundary γ_s such that:

$$W_{Tc} = -\int_{\gamma_C} \delta T q_C d\gamma \tag{2.28}$$

2.5 Description of the mechanical problem

The equation of equilibrium of forces exerted on a solid, as shown in figure 2.3, originated from Newton's law for a static state:

$$\nabla \cdot \boldsymbol{\sigma} + \mathbf{f}_v = 0 \tag{2.29}$$

where $\boldsymbol{\sigma}$ is the temperature dependent 2nd order Cauchy stress tensor and $\mathbf{f}_v$ is the exerted external body force. Thus, a temperature variation leads to deformation by the thermal expansion of materials. This deformation is considered the thermal deformation; however, the total deformation is the sum of the thermal deformation and the mechanical deformation as presented in equation (2.30):

$$\boldsymbol{\varepsilon} = \boldsymbol{\varepsilon}_{th} + \boldsymbol{\varepsilon}_m \tag{2.30}$$

where $\mathbf{H}(\mathrm{T})$ is the 4th order elasticity tensor of the material, $\boldsymbol{\varepsilon}$ is the 2nd order total strain tensor and $\boldsymbol{\varepsilon}_{\mathrm{th}}$, the 2nd order thermal strain tensor caused by the change of temperature distribution. Similarly, $\boldsymbol{\varepsilon}_{\mathrm{m}}$ is the 2nd order mechanical strain tensor.

The mechanical deformation is described by the Hook's law such that:

$$\boldsymbol{\sigma}(\mathrm{T}) = \mathbf{H}(\mathrm{T})\boldsymbol{\varepsilon}_{\mathrm{m}} \tag{2.31}$$

The total (final) deformation can be written considering equations (2.30) and (2.31) such that:

$$\boldsymbol{\sigma}(\mathrm{T}) = \mathbf{H}(\mathrm{T})(\boldsymbol{\varepsilon} - \boldsymbol{\varepsilon}_{\mathrm{th}}) \tag{2.32}$$

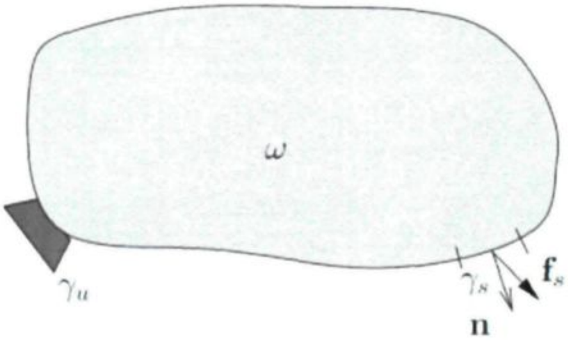

Figure 2.3: Computational domain of the mechanical problem [39]

The system requires respecting two types of boundary conditions such that:

$$\mathbf{u}\big|_{\gamma \mathrm{u}} = \mathbf{u}_{\gamma} \tag{2.33}$$

$$\boldsymbol{\sigma} \cdot \mathbf{n}\big|_{\gamma f} = \mathbf{f}_{\gamma} \tag{2.34}$$

The former is the Dirichlet (Essential) boundary condition, which is a displacement applied on a portion of the boundary γ_u of the domain ω. The latter represents the Neumann (Natural) boundary condition, which is a stress applied on a portion of the boundary γ_s of the same domain ω. By applying the method of weighted residuals on the equation (2.32), the weak form of the virtual work equation on the domain ω can be obtained:

$$\mathrm{W_M} = \int_{\omega} \delta\mathbf{u}^{\mathrm{T}} (\nabla \cdot \boldsymbol{\sigma} + \mathbf{f}_{\mathrm{v}}) d\omega = 0 \tag{2.35}$$

To make the boundary condition appear in the above equation, integration by parts is applied such that:

$$\mathrm{W_M} = \int_{\omega} \delta\mathbf{D}^{\mathrm{T}} \boldsymbol{\sigma}\, d\omega - \int_{\gamma_u} \delta\mathbf{u}^{\mathrm{T}} \boldsymbol{\sigma} \cdot \mathbf{n}\, ds - \int_{\gamma_f} \delta\mathbf{u}^{\mathrm{T}} \boldsymbol{\sigma} \cdot \mathbf{n}\, d\gamma - \int_{\omega} \delta\mathbf{u}^{\mathrm{T}} \mathbf{f}_{\mathrm{v}}\, d\omega = 0 \tag{2.36}$$

where $\mathbf{D}^{\mathrm{T}}$ is the vectorial form of the 2nd order virtual strain tensor in which δu, δv and δw are the components of the virtual displacement vector ($\delta\mathbf{u}$):

$$\delta\mathbf{D} = \left\langle \delta u,_x \quad \delta v,_y \quad \delta w,_z \quad \delta u,_y + \delta v,_x \quad \delta u,_z + \delta w,_x \quad \delta v,_z + \delta w,_y \right\rangle^{\mathrm{T}} \tag{2.37}$$

Since the displacement is prescribed on the portion γ_u, the second integral in equation (2.36) will be zero. Furthermore, considering the Neumann boundary condition presented in equation (2.34), the integral can be divided into internal and external contributions; and therefore, the equation below can be obtained:

$$\mathrm{W_M} = \mathrm{W_{M,int}} + \mathrm{W_{M,ext}} = 0 \tag{2.38}$$

with:

$$W_{M,int} = \int_{\omega} \delta\mathbf{D}^T\boldsymbol{\sigma}\, d\omega \tag{2.39}$$

$$W_{M,ext} = -\int_{\gamma_f} \delta\mathbf{u}^T\mathbf{f}_\gamma d\gamma - \int_{\omega} \delta\mathbf{u}^T\mathbf{f}_v d\omega \tag{2.40}$$

The load $\mathbf{f}_\gamma$ represents all of the forces applied on the boundary. The load applied on the boundary γ_s is represented by $\mathbf{f}_s$. The load $\mathbf{f}_c$ can also be applied on the portion γ_c from a solid in contact. In that case, a portion of the boundary is dedicated to contact boundary and a contribution of contact must be included in the virtual work of the external forces as below:

$$W_{M_C} = -\int_{\gamma_C} \delta\mathbf{u}^T\mathbf{f}_c d\gamma \tag{2.41}$$

2.6 Solution strategy

Modeling of the anode assembly requires solving all the thermal, electrical and mechanical problems introduced in the previous section. To do this, a system of equations must be solved, which is highly nonlinear. The variational expressions of the thermal, electrical and mechanical problems can be discretized by the finite element method. The details of such discretization have been presented in the thesis of P. Goulet [see 39].

The TEM equations system, the compact global matricial form of the governing equations, which is obtained from the linearization of the residuals of the equations using the first order Taylor series expression will take the form of equation (2.44) such that:

$$\begin{bmatrix} K_{TT} & K_{TV} & K_{TU} \\ K_{VT} & K_{VV} & K_{VU} \\ K_{UT} & K_{UV} & K_{UU} \end{bmatrix} \begin{Bmatrix} \Delta T \\ \Delta V \\ \Delta U \end{Bmatrix} = \begin{Bmatrix} R_T \\ R_V \\ R_U \end{Bmatrix} \tag{2.42}$$

where T,V and U stand for temperature, voltage and displacement respectively; R_T, R_V and R_U represent the residual expressions corresponding to the thermal, electrical and mechanical problems respectively. Also, Δ is the correction operator.. From the tangent matrix, it is clear that the thermal, electrical and mechanical phenomena are coupled. Each element of the matrix has two subscripts denoting one physical phenomenon affecting another (except for the elements on the main diagonal), e.g. K_{VT} is associated with the impact of the thermal phenomenon on the electrical one. A complete list of impacts of the physical phenomena was given at the end of section 2.2.

The TEM problem can be solved through different methods based on the coupling level between phenomena taking place in our specific problem. Solving a weakly coupled problem requires separating thermo-electrical (TE) problem(s) and the mechanical (M) problem from the global TEM system (2.42) so that the TEM problem is changed to a system of TE and M problem such that:

$$\begin{cases} K_{TT}\Delta T + K_{TV}\Delta V = R_T - K_{TU}\Delta U \\ K_{VT}\Delta T + K_{VV}\Delta V = R_V - K_{VU}\Delta U \end{cases} \tag{2.43}$$

$$K_{UU}\Delta U = R_U - K_{UT}\Delta T - K_{UV}\Delta V \tag{2.44}$$

Equation systems (2.43) and (2.44) show the sub-systems that must be solved iteratively. It should be borne in mind there is no impact on the mechanical condition stemming from electrical phenomenon; thus, the element K_{UV} will be zero and equation (2.44) can be simplified:

$$K_{UU}\Delta U = R_U - K_{UT}\Delta T \tag{2.45}$$

One approach is to initially solve the TE problem and then the mechanical problem using the temperature and voltage distribution obtained from the TE solution. In this approach, which is schematically presented in figure 2.4, the possible effects of the M solution on the TE problem such as variation of pressure dependent contact resistance and conductance is neglected. This approach is advantageous if such kinds of effects are slight and negligible. Put differently, the less nonlinear the problem is, the more accurate the results will be. Since each problem is solved only once, the computation time will be shorter compared to the other approaches.

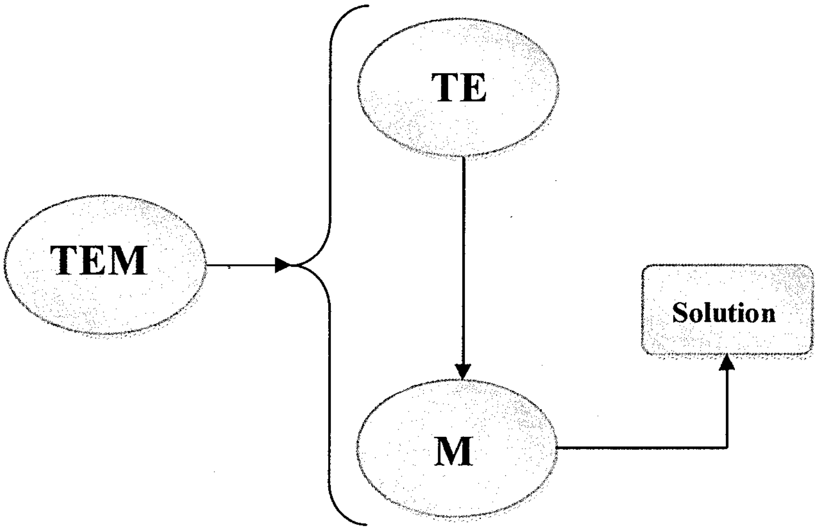

Figure 2.4: Weakly coupled approach to solve the TEM problem

Another approach, which could be designated as the fixed point method, is to initially solve the TE problem and then to feed the TE solution to the M problem and solve it. Using the M solution, the TE problem is solved again, considering the possible impact of the M solution on this problem. This loop repeats until there is a global and local convergence of both TE and M problems. Figure 2.5 is a flowchart explaining this approach.

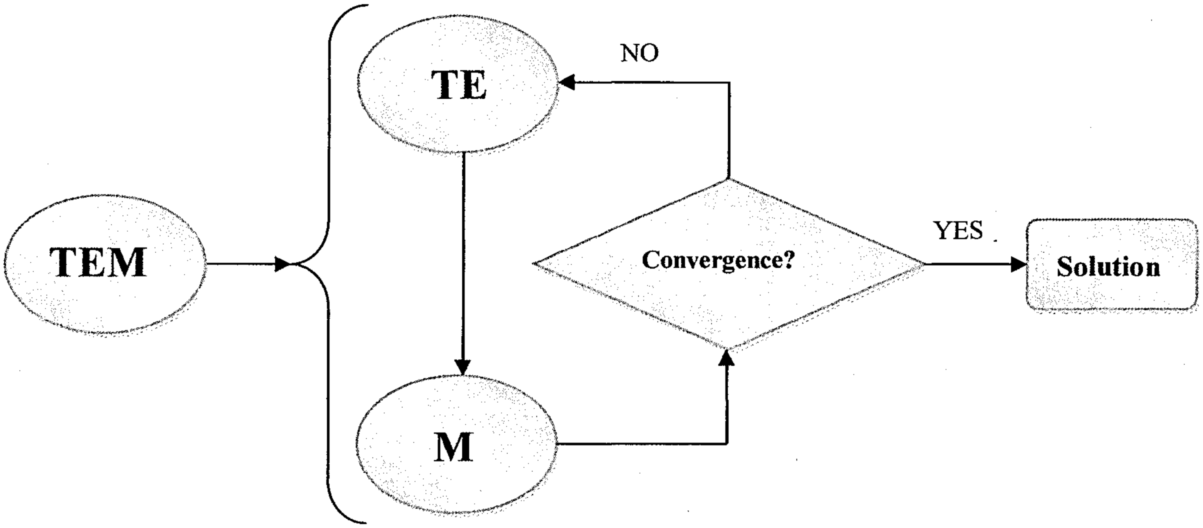

Figure 2.5: Weakly coupled approach - fixed point

Solving the fully coupled problem would be the third approach through which Newton-Raphson solution technique is used to solve all of the problems at each time step until convergence is reached when the correction of each field is less than a specified tolerance. Note that the same technique can be used to solve the problems in the two other approaches as well. When solving the fully coupled model, equation (2.42) is solved at once. In each iteration temperature, voltage and displacement are computed and then the tangent matrix and the residual vector are recalculated with the new values of temperature, voltage and displacement. Iterations are terminated once global convergence is reached. This approach generally reaches convergence faster than the second method (fixed point) especially during highly nonlinear sequences; however, it requires larger memory allocation for the factorization compared to solving the weakly coupled problem given that some coupling terms which are not considered in the previous methods occur in the fully coupled tangent matrix. The terms $K_{TU}\Delta U$ and $K_{VU}\Delta U$ are neglected when solving equations (2.43) in the two previous methods: impact of mechanical phenomenon on thermal and electrical phenomena.

In this work, the third approach, which is solving the fully coupled problem, is used. Also, an adaptive time stepping algorithm is used in conjunction with a bi-sectioning technique to avoid divergence of the Newton-Raphson solution technique during highly nonlinear sequences. 20 dual core Opteron™ 64 bits computing nodes with 2 GB of RAM per computing node were used to carry out the simulations. Required time to achieve a solution was between 9 and 13 hours for the simulations depending on the convergence encountered during each simulation. This last approach takes more time to solve each iteration, but takes less iterations to solve each time step. Also, it is more robust regarding the convergence during highly nonlinear sequences.

CHAPTER 3:
FINITIE ELEMENT MODEL

3.1 General points

A fully coupled TEM model of the whole hexapod anode assembly (AP30 technology) was developed in order to perform several simulations to achieve a better understanding of the system as well as to eventually lower the anodic voltage drop in the anode assembly. The model was built using APDL according to the technical drawing provided by RTA, which can be found in appendix A.

In terms of parameterization and geometrical modeling, two main types of parameterization were taken into account: parameterization of dimensions and parameterization of mesh settings (pattern). Considering the full anode assembly and 3 submodels that will be presented in detail later in this chapter, 83 parameters were defined to control the dimension of the full model and its mesh pattern. Furthermore, 12 macros were defined to operate some common tasks and some tasks that were not possible with APDL's basic functions, for example, sweeping from one area (source area) to another (target area) to build a volume. Since APDL is slow on large models, the full model is built through 4 input files; however, since there are 3 submodels too, the total number of programmed input files in this work reaches 7. For the full disclosure of the parameters used, refer to appendix B. Also, for the future users and/or developers of the presented model, all of the APDL component names and types, attributed material, real constant and element type numbers are given in appendix C.

After building a robust numerical model of the whole anode assembly, the first concern was to investigate the critical cast iron/carbon connection area adequately prior to using the full model in more realistic conditions. An auspicious approach requires making sure of understanding the phenomena in a simplified model before using the more complex full anode model. Nevertheless, the presented model may be useful in finding some optimization ideas regarding the stub hole. In addition, with the simplified model, the accuracy of the constitutive laws and material properties chosen for the model can be validated. It would not be a sound approach to address all of the issues at once using the whole anode model. The results obtained from the simulations in this work unraveled many unclear aspects that have been addressed by other researchers previously (e.g. contact evolution) or confirmed their findings (e.g. significance of the cast iron/carbon interface resistance).

To do this, three submodels (for submodels refer to section 3.2.1) were extracted from the full model to use for various simulations, which would help us to investigate the behavior of the system under different conditions. Note that only one of the three submodels, called the **half block model**, was used for this research.

A laboratory (experimental) model, extracted from a full anode assembly, was used to perform a series of experiments to investigate the voltage drop at different positions in the model. The experimental tests were performed by RTA. The submodel, used in this research, was generated with the exact dimensions of the experimental model to be used as its numerical representation. The results of the experimental tests were used to calibrate the numerical model and then the numerical model was used to carry out several sensitivity analysis simulations to better understand the phenomena taking place in the stub/carbon connection area. Detailed explanation on the results will be given in CHAPTER 4:.

3.2 Geometry of the anode assembly

3.2.1 Full anode assembly model and submodels

As mentioned in the previous section, a fully parametric model of the hexapod anode assembly was built using APDL 12.0. APDL is a scripting language that can be used to customize and automate common tasks in ANSYS®. APDL enables its users to build parametric models to quickly evaluate design changes. It also encompasses a wide range of other features such as import and export data to external files, macros to automate complex or frequently repeated tasks, if-then-else branching, do-loops, and scalar, vector and matrix operations. It also can be used to create simple customized menus and toolbars. APDL can be an advantageous tool for design optimization and adaptive meshing in hands of users with good knowledge of basic programming and geometrical modeling. Like any other numerical tool, APDL has its disadvantages: an inefficient help feature, limited customization, and slow realization of changes in large models, for example. APDL was used to develop the full anode assembly in this work in order to benefit from its advantages to generate parametric models. Such kind of model cannot be fully or easily developed with soft wares such as Workbench etc. Also, mesher of APDL is not as good as that of Workbench.

According to the explanation given in CHAPTER 1, an anode assembly consists of superior part, cast iron connectors and carbon block(s). In figure 3.1, which demonstrates the developed model, it can be seen that crust and bath have been developed in addition to the anode assembly to adequately represent the boundary conditions; however, it will be henceforth referred to as the **full anode assembly model**, or, briefly, the **full model**.

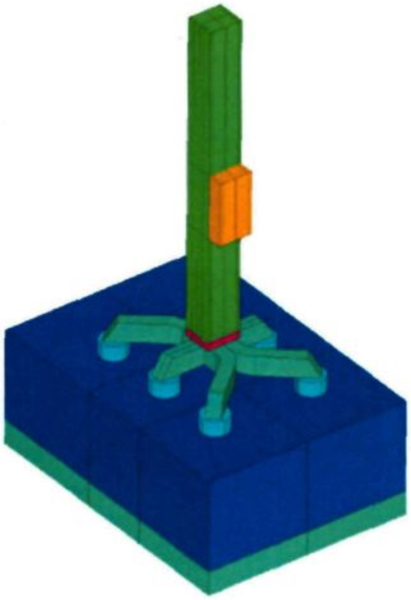

Figure 3.1: Full anode assembly model

Three submodels were generated from the full model to carry out specific simulations[4].However, using other submodels prior to using the full model would be the intermediate steps towards a systematic approach to simulate the very realistic reduction condition using the full model. Figure 3.2 to figure 3.4 depict these submodels.

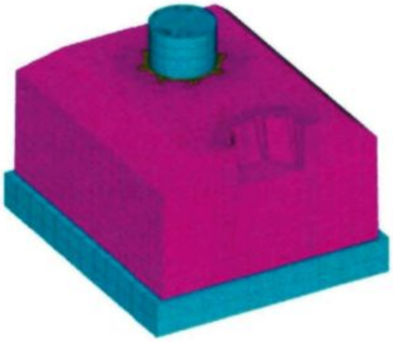

Figure 3.2: Half block submodel representing Electrical Contact Furnace (ECF) model

One stub submodel and half block model have essentially the same application. The major difference between these two models is the geometry of carbon. The stub in the one stub model is the middle one in the full anode model, whereas the half block model has one of the side stubs. Due to different carbon stiffness originating from different dimensions of carbon blocks in the aforementioned submodels, it is expected that carbon respond differently to stress taking place in the stub hole, caused by thermal expansion. Furthermore, it is conceived that comparison of the results of the same simulations using these two submodels can reveal the effect of symmetry in the carbon block. Also the stub in the half block model is shorter than it is in the one stub model. This is done exactly according to the dimensions of the experimental model.

Another component which is not originally a part of the anode assembly, called "support", was added to these submodels and is used to fix the models at their bottom. This

---

[4] It should be noted that only the half block model which is one of the three submodels was used to fulfill the simulations in the author's Master's project. The other two submodels are supposed to be used in the future projects by other investigators.

was according to the experimental model which will be explained in the next chapter. Support can be seen in the figures of both models, namely figure 3.2 and figure 3.3.

Figure 3.3: One stub submodel

The half anode assembly submodel can be used to perform more realistic simulations. Using this submodel, the impact of mechanical deformation of yoke arms on contact distribution and the impact of bath and crust on the temperature and potential distribution can be analyzed. Using this model requires the assumption of a perfect rodding process which means none of the stubs has any deviation from the center of stub holes. To carry out simulations to investigate the influence of imperfect rodding process caused by the displacement or rotation of the superior part, which results in angle-variant cast iron thickness, the full anode assembly must be used; otherwise, using the half anode model will save an enormous amount of simulation time. It should be borne in mind that analyzing the angle-variant cast iron connector impact on the contact condition, and consequently the total voltage drop can be studied primarily using the one stub or half block model.

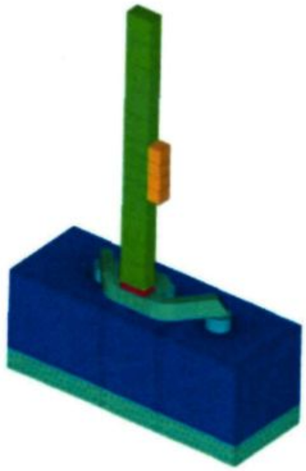

Figure 3.4: Half anode assembly submodel

3.2.2 Main components of the full model

The full model consists of several major and minor components. For the sake of ease in modeling the geometry, a classification in terms of geometrical modeling (in ANSYS® environment) was done by the author so that the main components of the full model are built through separate input files.

To generate the full model or submodels, slightly different paths may be followed as shown in figure 3.5. The figure shows the execution order of the input files to build the models and the name of the files under which the output of each step is saved. The full anode assembly model is saved under two different versions: the full model attached to the geometrical entities (volumes, areas, lines etc) and the full model detached from the geometrical entities which contains only elements, nodes and mesh components. The main components of the developed full model in this work are:

- Superior part
- Cast iron connectors
- Carbon blocks
- Crust
- Bath

As it can be seen, the superior part, itself, consists of several minor components such as:

- Rod or stem
- Plate
- Clad
- Yoke
- Stubs

Rod is usually made of aluminum and is used to hang up the entire anode assembly in the cell. Rod is fixed to the superstructure on the anode beam by a sophisticated clamp system. Clamp design can vary from one technology to another, but there is a part of it that conducts the electric current. This part, which is in contact with the rod surface, has been modeled hypothetically as a plate. This way, electrical contact between clamp system and rod could be easily modeled and dealt in simulations disregarding clamp design or shape. Figure 3.6 depicts a cell in which rod and clamp can be seen. Clad joins rod to the steel yoke. Yoke is welded to certain number of steel stubs at the end of each yoke arm. In the developed hexapod model, there are 6 yoke arms; and therefore, 6 stubs.

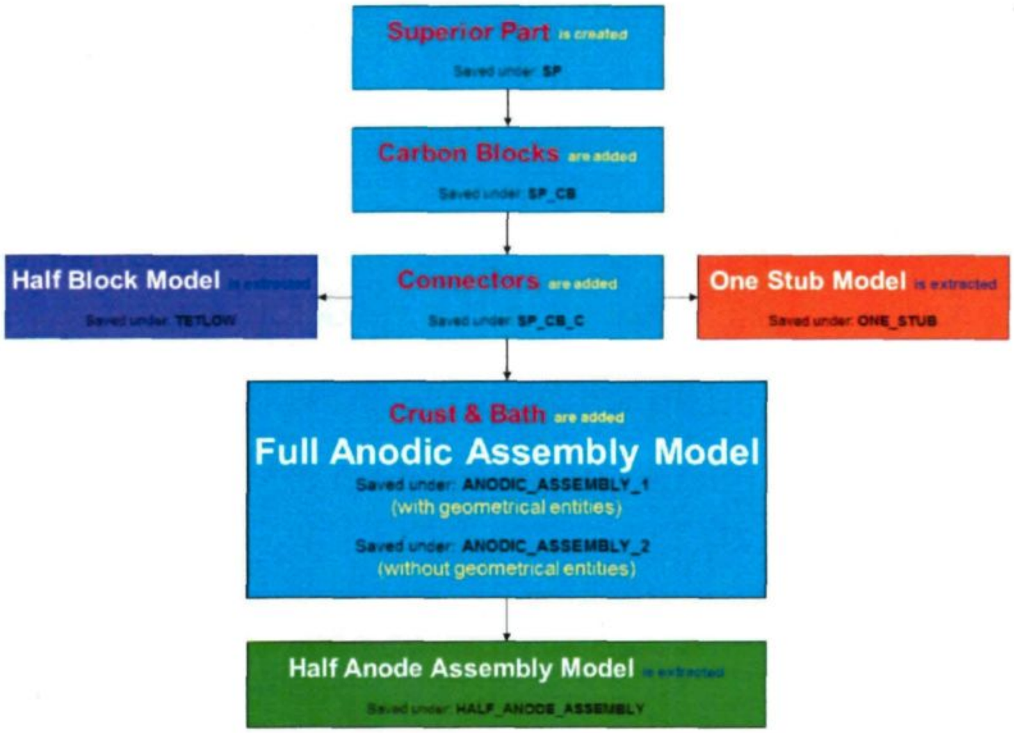

Figure 3.5: Execution order of input files to build models

Cast iron connects the superior part to the carbon blocks. Since cast iron connectors have the most complicated geometry in terms of modeling; and also, stub hole design plays an important role in contact establishment when in operation, they are considered as major components of the anode assembly. Several smart macros enable the users to build geometries of connectors with different designs. Crust and bath are two main components of the model that have different roles in the electrolysis process; nonetheless, they are built with one single execution (input) file.

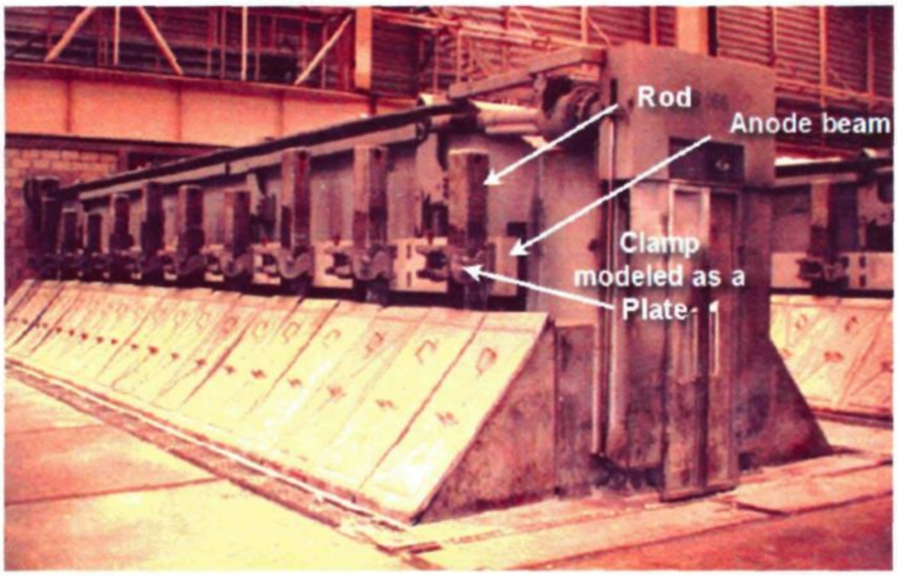

Figure 3.6: A Pechiney 300 kA PB cell at St. Jean-de-Maurienne, France [43]

A cut model illustrating the minor and the major components of the developed full model is shown in figure 3.7. Notice that pancakes (read next section) are not actually components and are supposed as a defect; however, they can be included in the model by the user.

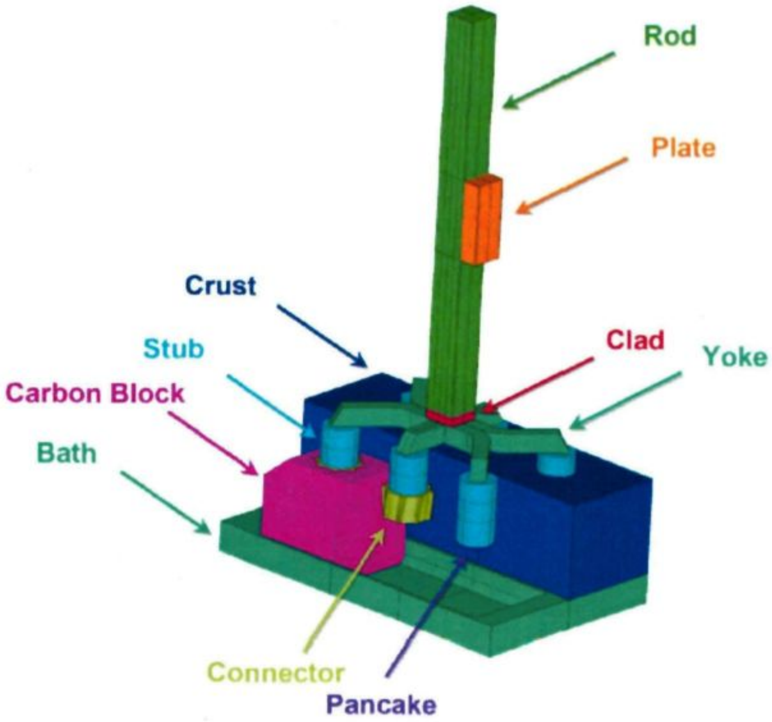

Figure 3.7: Components of the full anode assembly model

3.2.3 Rodding (Sealing) process defects

To fix the carbon block(s) to the superior part, stubs are positioned into the specially designed holes called stub holes; then, molten iron is cast to connect and fix carbon block(s) to the superior part. This process is called rodding or sealing. Once the cast iron solidifies, since it does not wet carbon, a gap opens up at the cast iron to carbon interface. Rodding is a delicate process and in practice a perfect rodding through which the stub is perfectly centered and well-positioned in the stub hole, cannot be reached. Some mismatch of the center of stubs and center of stub hole is always possible. Also, a slight deformation of the components of the superior part can cause such mismatches. Some of the usual problems that result in defects are due to imperfect rodding such as pancake formation, angle-variant thickness of connectors (caused by malpositioning of stubs into stub holes) and cold shut.

Cold shut is a discontinuity that appears on the surface of cast metal as a result of two streams of liquid metal meeting but failing to unite. In the case of anode sealing, it happens especially where the gap between stub and stub hole wall is much less than it should be with a correct positioning of the stub in the stub hole. A higher gradient of heat conduction quickens solidification and the stream is not given enough time to flow and unite with the other stream coming from the opposite side. The results are like a large discontinuity of cast iron in the connector wall as shown in figure 3.8.

Photo: Rio Tinto Alcan

Figure 3.8: Cold shut defect in cast iron connector

Most of the time, anode assemblies have more than one stub. In this work, the anode assembly was a hexapod (6 stubs). In the rodding process, not all of the stubs are of the same size, especially if they are used rather than brand new. Thus, they have slightly different heights and diameters. In the rodding shop, to place the stubs into stub holes, a hanger lowers the anode assembly slowly until one of the stubs touches the bottom of the corresponding stub hole. Usually there can still be some air gaps between the bottom of the stubs and the corresponding stub hole bottom. Therefore, when casting molten iron, this gap can be partially or completely filled up with cast iron. The part of cast iron which fills this gap is called a pancake. It is clear that with a partial fill-up, there will be a huge air gap that will provide absolute resistance against the electric current. Even in the case of a complete fill-up an air gap will open up between carbon and cast iron. Unlike the initial air gap around the stub hole wall, this air gap cannot be filled up completely in operation due to the anode hanging. Figure 3.9 demonstrates the rodding process and also pancake formation.

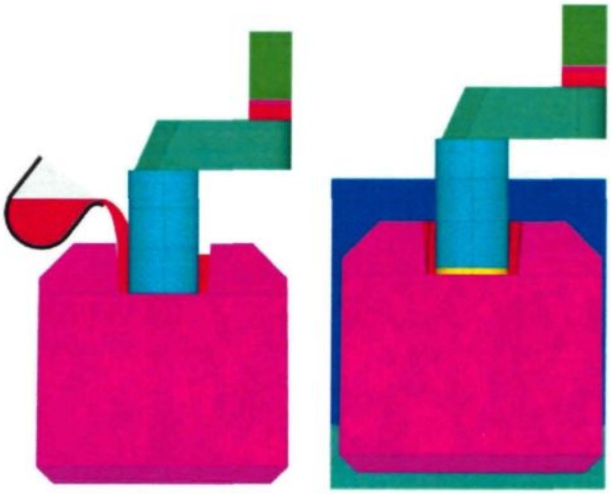

Figure 3.9: Rodding process and pancake formation

There has been no model to datethat can present pancake formation and its effect on contact and consequently on the voltage drop. A connector with pancake is also depicted in figure 3.10 (middle one). Also in this figure, angle-variance of wall thickness in cast iron connector is demonstrated (left side connector). The right side connector represents a perfectly cast one.

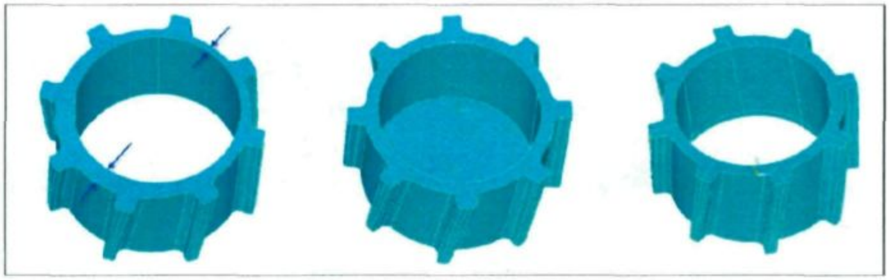

Figure 3.10: Cast iron connector with and without pancake and with angle-variant wall thickness

3.2.4 Features of the full model

The presented model offers some features, most of which distinguish the model from the previously presented ones. Some of these features are itemized below:

1- Number of flutes
2- Shape of flutes (flute design)
3- Malpositioning of stub into stub hole
4- Pancake formation
5- Carbon consumption
6- More realistic geometry
7- Capability to generate submodels

Several smart macros were defined to build the model specifically to build stub hole and cast iron connectors, which have complex geometries. The macros have been defined in such a way that they can model different designs of connector flutes and geometries. As described in the section "Previous Work" (section 01.6), there has been some work on the impact of the number of flutes on contact and voltage drop. This model can also build connectors with different numbers of flutes. This feature will help demonstrate the effects of different number of flutes on the total voltage drop. Knowing that there has been a strong tendency to redesign the stub hole or improve its design recently, the flute design feature distinguishes this model from other models since it is a powerful tool for modeling different designs of flutes with the built-in macros.

Figure 3.11 and figure 3.12 show some examples of connectors built with different numbers of flutes and different flute designs consecutively. Four cast iron connectors have been presented in each figure. The former shows connectors with 4, 10, 15 and 20 flutes. Some of the previously presented models could not generate connectors (or stub holes) with any specific number of flutes; however, the full model is capable of generating any number of flutes which is a divisor of 360 degrees. This is the only limitation which originates from the symmetrical design of the stub hole. Notice that the dimensions of the flutes are different in each case. In the latter, connectors with various flute shapes have been generated. This feature can be enormously helpful in the stub hole optimization or redesign.

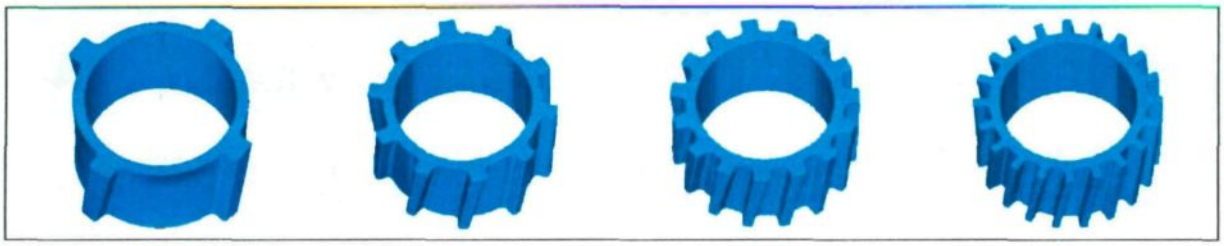

Figure 3.11: Number of flutes feature

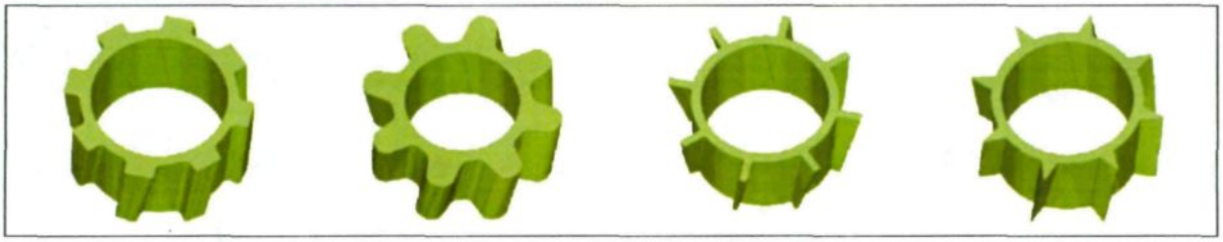

Figure 3.12: Shape of flutes feature

Sometimes, stubs are not correctly centered in the stub holes due to the displacement of the superior part from center or its rotation while it is hung in the rodding shop. In this case, after rodding, the resultant thickness of the cast iron connector wall will be angle-variant. It is assumed that in this case, the quality of contact will be poorer when in operation; nonetheless, this is yet to be investigated in depth since there has been no work thus far which addresses such kind of defect. It is the first time that the malpositioning of stubs into stub holes has been modeled and presented. The right side connector shown in figure 3.10 illustrates a perfect connector. The thickness of its wall (cylindrical portion) is constant. A connector with varying wall thickness, caused by malpositioning of stub into stub hole, is also depicted in the left side connector in the figure. An interesting comparison of a real sample of a connector with angle-variant wall thickness to a numerically modeled one has been shown in figure 3.13.

Figure 3.13: Cast iron connector with angle-variant thickness, real sample vs. modeled one

It takes 20-30 days for a carbon block to be fully consumed in the electrolysis process in the AP30 technology depending on the operational electric current; hence, the height and the volume of the carbon block decrease day by day. All of the presented models to date have been considering brand new carbon blocks for the analysis, while some of the properties of carbon such as carbon stiffness may change with a changing volume of carbon. Thus, the behavior of the anode assembly with a consumed carbon and also contact quality at the cast iron to carbon interface are unknown aspects since no simulation has been carried out to investigate such a case. Also, there are no measurements available. The presented model can simulate an anode with any arbitrary carbon height. In other words, the anode assembly can be modeled and simulated not only when it is brand new (first day in operation) but also, at any point of the operation period (lifetime). This feature can facilitate the way of analyzing the evolutive behavior of contact with varying carbon height. Figure 3.14 depicts two anode assemblies with brand new and used (consumed) carbon blocks.

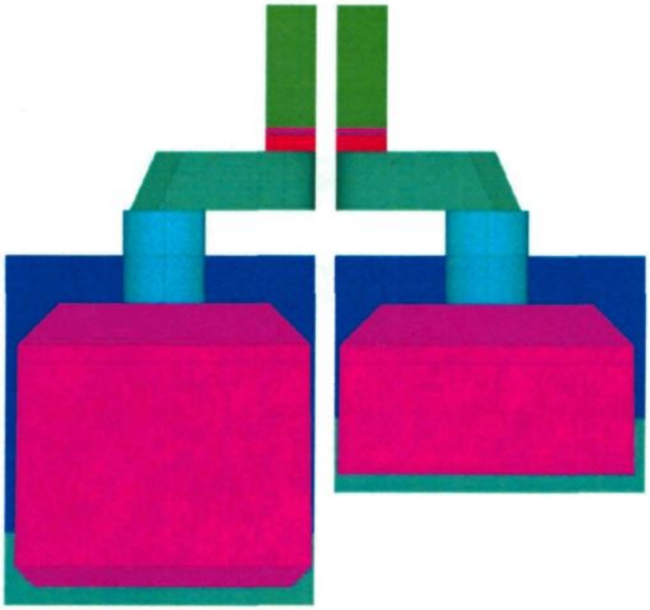

Figure 3.14: Carbon consumption modeling

3.2.5 Half block model, ECF model and experiments strategy

As previously explained, the half block model was extracted from the full model to carry out some preliminary analyses to investigate the phenomena present in the stub/cast iron/carbon area. The half block model was the numerical representation of its laboratory model, the so called Electrical Contact Furnace model or ECF model (primarily called Tetlow furnace model), shown in figure 3.15.

The strategy in performing experiments was to apply a uniform temperature (by keeping it in a furnace) to the entire model; then, a current of 1 kA was applied for 3 minutes to the top of the stub. After reaching a steady state condition, electric potential was measured by several probes at different positions in the model. Having potential at the specific positions in the model, voltage drop can be calculated between any pair of positions. Temperatures at which potential was measured were from 400°C to 950°C in increments of 100°C (50°C for the last increment). The same strategy was followed in the numerical simulations. The results generated by the simulations were recorded at temperatures from 400°C to 900°C with a constant increment of 100°C and finally at 950°C. Henceforward, for the sake of ease and simplicity the half block model is referred to as the model.


Photo: Rio Tinto Alcan

Figure 3.15: Electrical Contact Furnace (ECF)

3.3 Interfaces, contact and transition gap

In the half block model there are 5 interfaces overall:

1. Between cast iron and carbon
2. Between stub bottom and stub hole bottom
3. Between steel stub side and cast iron interior side
4. Between carbon bottom and support top
5. Between cast iron connector bottom and stub hole bottom

Initially, when building the geometry of the model, no air gap at the interfaces is generated; however, air gaps with different patterns can be applied to the model in the analysis step. FESh++, which was used for the analysis step, enables its users to apply complex air gap patterns easily. It is conceived so that the current flow from the bottom of stub and the bottom of the cast iron connector to the carbon block is the least. This is due to no or very low contact pressure (in real operation) generated at the interface of stub-connector to the stub hole bottom. However, it was possible that stub was in contact with the stub hole bottom at room temperature in the experimental model. It is known that according the stub hole geometry, with an increasing temperature the connector will move towards up and will lose contact even if the carbon block is placed on a support like in the experimental tests realized at CRDA. Moreover, there is good contact between stub and cast iron according to the *in situ* observations. Among all of the abovementioned interfaces, the cast iron to carbon one plays a key role in establishing good contact and controlling contact quality.

The support is set to have a Thermal Multi Points Constraint (TMPC) with carbon. The experimental model was connected to the support through several bolts. In order to avoid any noise deformation in carbon, assuming a perfect connection, the same coefficient of thermal expansion was used for both components (carbon and support). A perfect TEM link (TEM MPC) was applied to the stub/cast iron interface. The remaining interfaces provide TEM contact between corresponding contact surfaces. Very high contact resistance was employed at the interfaces below the stub bottom and the cast iron connector bottom. The contact properties were taken from M. Rouleau [32]. Contact properties are presented in detail in appendix D. Also, element type, mat and real attributions for contact pairs can be found in appendix C.

As explained in section 2.2 (Physics of the problem), the gap at the interface of cast iron to carbon is not perfect in practice. If it were, then the electric current could not pass through the interface and the cell could not be started and set to operation at all. Actually, after anode sealing and before putting the anode assembly in the cell, there are some points at which two surfaces of the interface touch each other. These contact points facilitate of more contact points. Generation of contact points continues until good contact is established and a steady state is attained.

It is not an easy task to numerically model exactly what takes place at the cast iron to carbon interface. Nevertheless, the electrical contact resistance concept and the fact that it decreases as temperature and contact pressure increase is a major help to model this process numerically. For this purpose, high contact resistance is applied to the interface until two contact surfaces touch each other. From that point on, the constitutive law obtained from experiments provides the governing contact resistance.

During temperature increase, to reach the operational condition, contact resistance drops drastically once two contact surfaces touch each other. The decline in contact resistance continues sharply while contact pressure is applied to the interface afterwards due to the thermal expansion. It is also possible during some simulations that contact is lost and contact resistance increases sharply. Such an abrupt change in the (effective) value of contact resistance may result in problems of convergence. To avoid any discontinuity, a Hermitian function was applied to smoothen the transition from non-contact to contact condition or vice versa. The Hermitian function is consistent in value and slope.

To implement such an approach, a transition gap value is set in the function so that the function takes control of applying governing contact resistance to the interface once two contact surfaces reach to the proximity of the transition gap or closer until they touch each other. The Hermitian function (transition function) gives its place to the contact resistance constitutive law obtained from experiments once two contact surfaces touch each other and establish physical contact. Figure 3.16 depicts a schema of the transition from non-contact to contact and vice versa through the Hermitian function. It shows how transition from non-contact to contact condition or vice versa can be problematic when contact is established or lost. It is clear that the pattern of the transition will depend on the values of the non-contact resistance, transition gap and resistance at the moment of touch. In this work, the default value for the transition gap was 1 mm. The non-contact resistance value was set to 5000×R_c

at gap=0. In fact, when the air gap magnitude decreases and reaches 1 mm the Hermitian (transition) function governs the transition from $R_{c\,max}$ to $R_c(g=0,T)$.

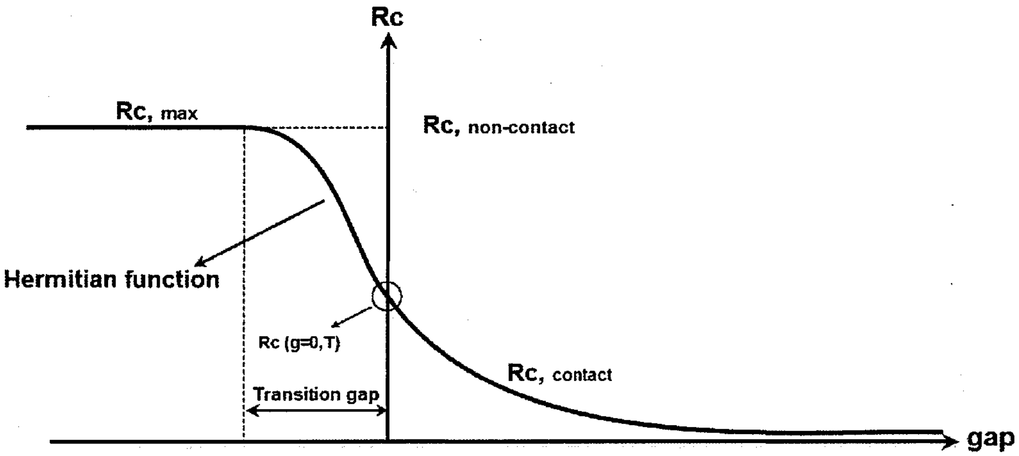

Figure 3.16: Transition gap and Hermitian function

Figure 3.17 illustrates the Hermitian contact transition function generated with the Maple code. The horizontal axis is the gap at the cast iron/carbon interface and the vertical axis is the imposed contact resistance. Note that the figure is only for demonstration purposes since the gap in the figure has been set to 0.1 mm, however the start (default) value was 1 mm.

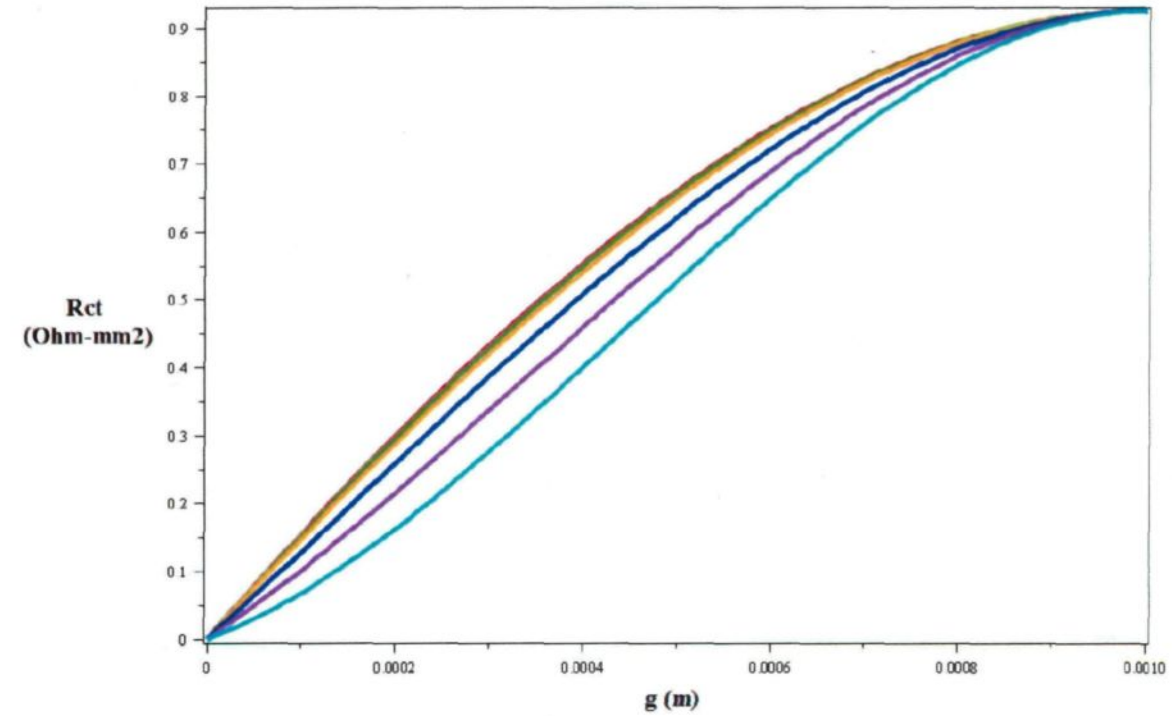

Figure 3.17: Hermitian contact transition function

3.4 Mesh and time stepping

The overall number of elements and nodes of the model are 63239 and 65803 respectively. Table 3.1 presents a summary of the finite element mesh composition of the model. These numbers can be slightly different depending on the pattern under investigation. Numerous mesh parameters have been defined to control the local and global mesh of the full anode assembly model. Appendix B details all mesh parameters in conjunction with dimension parameters to controls the mesh pattern and shape of the model. The global mesh pattern must assure global convergence with accepted accuracy. In addition, to locally refine the mesh, defined parameters can be used to avoid increasing global number of elements and keep the simulation duration as short as possible.

Table 3.1: Mesh composition

Component	Element Type	Number of elements
Solid	Linear Hexahedral, 3D Coupled Field Solid	58041
Contact	Linear Shell	10739
BCs	Linear Shell	7115

Using the mesh controlling features, special attention has been paid to the stub hole region mesh. Carbon around the stub hole, where it establishes contact with cast iron, can be meshed with a refined mesh to ensure the accuracy of the results (good representations of the gradients close to the interface) while the rest of carbon can be meshed with a coarser pattern to decrease simulation time. This can be seen in figure 3.18 where a relatively refined mapped mesh pattern has been applied in meshing cast iron and its surrounding carbon while the mesh transforms to a coarser pattern after a certain radial distance from stub hole. This radial distance can also be controlled by the user.

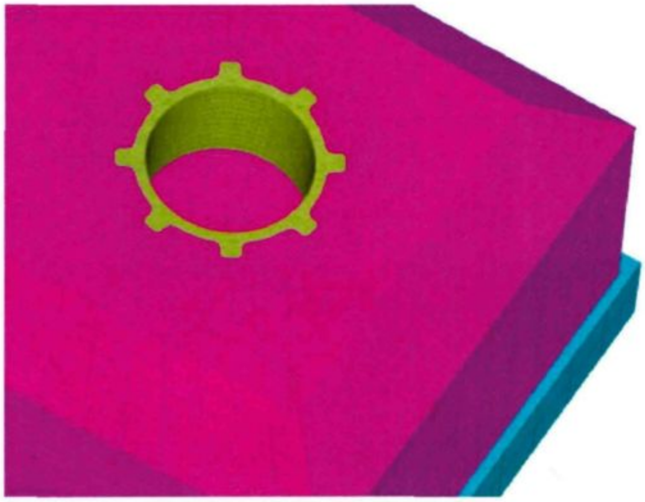

Figure 3.18: Connector and carbon block mesh

Contact problems are delicate to solve due to their highly nonlinear nature. Numerosity of contact (numerous surfaces in contact) in one single model adds to its complexity. Since the model was TEM and included contact in several parts, to avoid any problem causing divergence loads were applied in 3 steps as shown in figure 3.19. Step 1 consists of one single substep; step 2 consists of 2 substeps and step 3 consists of 6 substeps (equivalent to the number of time intervals to reach 950°C from 400°C). In the first step, the temperature of the model is set to 400°C and all mechanical loads (body loads) are applied. They serve to stabilize contact since no other mechanical force takes place in the system. Using material density given in in appendix E, these loads can be calculated. While retaining the temperature in the second step, the electrical loads are applied, meaning that the electric current is applied to the top of the stub and the bottom surface of the carbon block is set to zero volts. This step is the most sensitive one, since it is during this step that the contact conditions start to change significantly. Step 3 is the one during which simulations begin. After attaining convergence for the case of 400 °C, the results are recorded and the temperature is increased from 400 °C to 950°C by applying various temperatures (substeps) at which the solution is monitored.

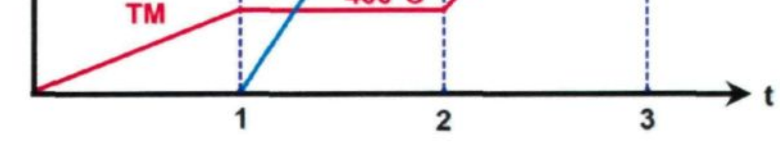

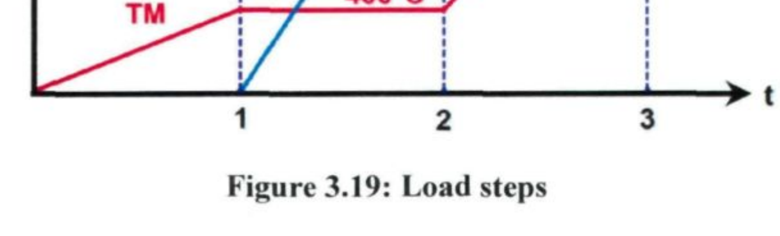

Figure 3.19: Load steps

3.5 Material properties

Carbon was supposed linear elastic. The quasi-brittle with softening constitutive law, developed by D'Amours *et al.* is a better one which is supposed to be considered the next step for more realistic carbon behavior as well as including cracking and damage prediction [see 44]. Electrical resistance of carbon was assumed orthotropic as per Wilkening and Côté [33]. The support was considered as an isotropic thermo-elastic material. The stubs and cast iron connectors were considered isotropic thermo-electro-elastic materials. Experimental results obtained at CURAL were used for thermal expansion of steel and cast iron with respect to temperature. Most of the material properties used in this model are confidential; and therefore, are presented in appendix E respecting the confidentiality agreement with RTA.

3.6 Boundary conditions

Since the model is dealing with thermal, electrical and mechanical phenomena, the boundary conditions have been itemized accordingly as following. Figure 3.20 demonstrates the boundary conditions.

- The temperature was prescribed on all nodes in the model. Since a uniform temperature was attained in experimental tests before applying electric current in each step, 7 constant temperatures of 400°C-950°C with an interval of 100°C (except for the last one which was 50°C) were applied to all of the nodes in the model according to the step 3 in load steps.

- The applied current in the experiments was 1 kA for all cases. To apply the same current a current density corresponding 1 kA was applied to the top of the stub. Notice that electric current density will be different with a different stub cross-sectional area.

- Zero voltage was prescribed at the bottom of the carbon block. Being a Dirichlet BC, zero potential was applied on all of the nodes at the bottom surface of the carbon block. In practice, potential at the bottom surface of the carbon block is not zero; however, since voltage drop is essential here, describing a zero potential will simplify the calculation.

- The support was fixed at the bottom face. This was according to the experimental setup. The support is supposed to act as a foundation on which the experimental setup was fixed and essentially should not have any influence on electrical potential. This is why support is supposed as a TM component.

- The stub was fixed in the x-y (horizontal) plane through fixing its nodes on the perimeter of the top surface. In other words, nodes that belong to the top surface of the stub and to the perimeter surface of the stub were fixed for horizontal displacements. This was also according to the experimental setup; however, fixing the entire nodes on the top surface of the stub should provide largely the same condition. z direction (vertical) was left untouched so that the stub can freely move in that direction. Apart from this being the case in the experimental tests, the interaction between stub hole, connector and stub will take place without any imposed force originating from thermal expansion and fixed-end system, which is restrained at both ends.

- Weight of the model was considered. This is supposed to be a body load and the one that provides the conditions for establishing contact since no internal force is generated.

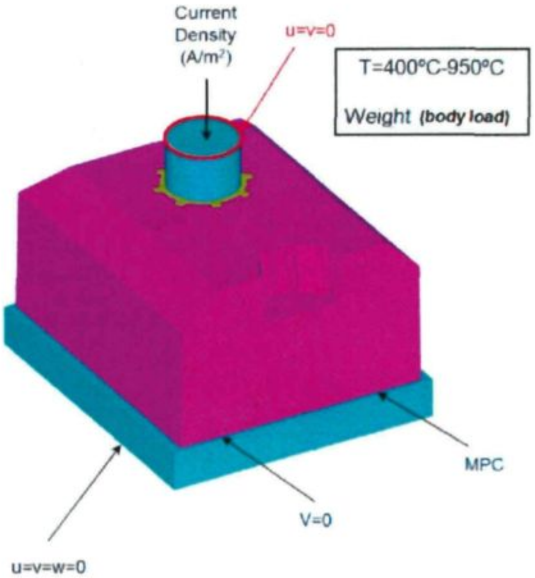

Figure 3.20: Boundary conditions

3.7 Initial air gap

Although modeling and simulation of the anode assembly or some other parts of the Hall-Héroult cell began years ago, not much work has been done on predicting the initial air gap at the cast iron to carbon interface. Richard *et al.*, in their 2009 paper [see 5] , used a pair of linear functions to predict the air gap and applied it to some extent. These equations are defined such that:

$$\gamma = R_{\text{stub}}\alpha_{\text{steel}}(T_{\text{ph}} - T_0) \tag{3.1}$$

$$\text{gap}(z) = \gamma + (t(z) - \gamma)\alpha_{\text{cast iron}}(T_s - T_0) \tag{3.2}$$

where α is the secant thermal expansion coefficient; T_{ph}, the effective stub temperature at cast iron solidification;T_0, the ambient temperature; t, the thickness of cast iron and T_s is the solidification temperature of cast iron. The gap is affected by different types of variables: R_{stub} and t are the geometrical (design) impact; α_{steel}, $\alpha_{cast\ iron}$ and T_s are the material properties impact; and, T_{ph} and T_0 are the rodding (sealing) process impact. In practice, there is not much room to change T_0; however, T_{ph} has a noticeable impact on the final air gap size. Practically all of the variables in the abovementioned equations are determined for a given anode assembly except T_{ph}, which is complex to measure. To evaluate T_{ph}, the numerical results, obtained through a systematically varying T_{ph}, are compared to the experimental ones until a good agreement is achieved. This is why T_{ph} is employed as a calibration parameter.

Richard *et al.*, as a first approximation, considered a uniform (constant) gap for different zones (cylindrical portion, tip of flutes and sides of flutes as shown in figure 3.21), while a more realistic application requires the employment of a linearly varying magnitude of gap along the height of the cast iron connector. They concluded that the magnitude of the air gap between cast iron and carbon had a significant impact on the predicted voltage drop, as it controls the resultant contact quality at the carbon to cast iron interface [5].

Equations (3.1) and (3.2) were also used in this work, but to a full extent. Considering the geometry of the cast iron connector, the gap magnitude will change linearly from its top to the bottom, due to changing thickness of cast iron along its height. Furthermore, the gap magnitude on the tip of flutes, at a certain level along the height, will be larger since cast iron is thicker, compared to the cylindrical portion thickness at the same level. This has been illustrated in figure 3.22 in an exaggerated way. Equation (3.1) calculates the radial contraction of stub, which is added to the radial contraction of cast iron to estimate the total gap at a certain level. The lateral gap of flutes are not influenced by the stub shrinkage. To estimate the size of the initial air gap on the sides of the flutes, equation is used with $\gamma = 0$. Since the resultant value will be the entire amount of lateral contraction, only half of the value must be applied on each side.

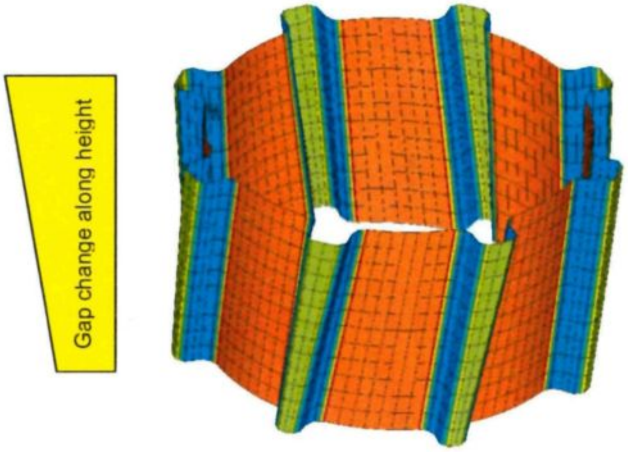

Figure 3.21: Color-coded initial air gap zones

Initial air gap is applied to the model in the beginning of the solution step and not during the modeling step. A series of Maple applications are used to define the final algebraic equations to be inserted in the appropriate FESh++ files. This way, the user has much more flexibility to control the air gap pattern applied to the interfaces and also to choose different zones.

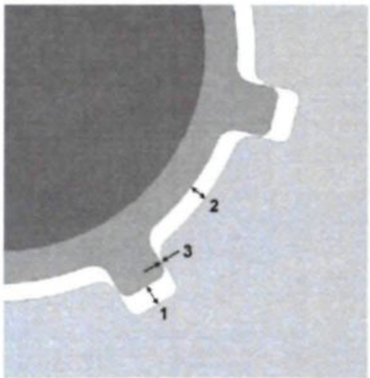

Figure 3.22: Initial air gap (exaggerated)

A tolerance parameter is used to control specifications of the zones in the analysis step. If there was no fillet at the tip (face) edges of the flues and their stem (where they are connected to the cylindrical portion of the cast iron connector), it was a simple task to determine these three zones and attribute nodes and elements to the zones, but practically there are fillets at the tip edges of the flutes and also at their stem. These fillets can be of different sizes based on the design. Also the size (radius) of the fillets typically increases from the bottom to the top of the connector along a spiral path which makes it complicated to determine the border of the zones easily. In a meshed numerical model, different mesh patterns can add to the complexity of attributing the nodes to the three zones. Therefore, implementation of a smart algorithm to do this task under any condition (different geometry or mesh) was substantial. Moreover, proper determination of the air gap zones is essential to acquire accurate numerical results fitted with the experimental ones. To determine these zones, a mathematical function was implemented in FESh++. A tolerance parameter as shown in figure 3.23 was defined to control determining the air gap zones at the cast iron/carbon interface in the numerical model.

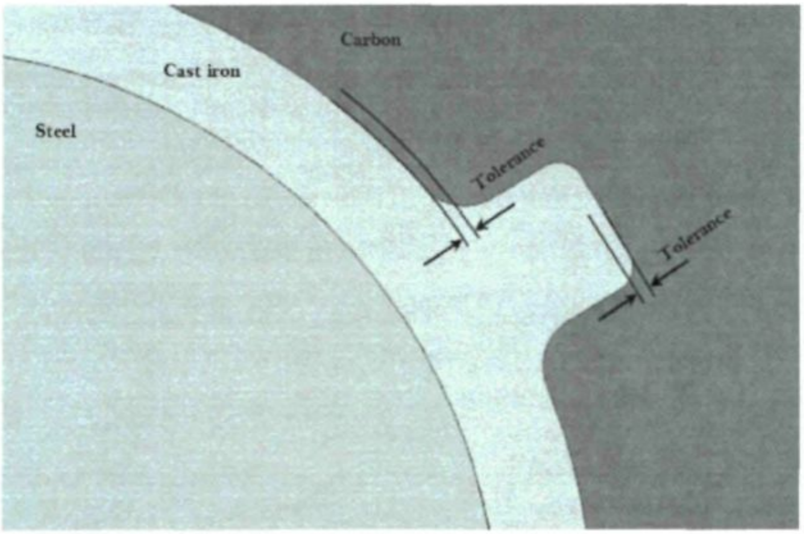

Figure 3.23: Tolerance parameter to determine air gap zones

Employing the tolerance parameter, a simple piece-wise function can be implemented to distinguish air gap zones:

$$\mathrm{Gap}(z) = \begin{cases} \text{if } R < R_{\mathrm{cyl}} + \mathrm{tol} & \text{Cylindrical portion} \\ \text{elsif } R > R_{\mathrm{flute}} - \mathrm{tol} & \text{Tip of the flutes} \\ \text{otherwise} & \text{Side of the flutes} \end{cases} \tag{3.3}$$

Note that each piece will be a function of z. In fact equations (3.1) and (3.2) will be these functions; nonetheless, they will be calculated and modified according to the coordinates system of the model; and also, determining variables existing in these equations. R is the radial distance from center of stub hole, R_{cyl} and R_{flute} are the radius of the cylindrical portion and the radial distance of the flutes tip which both vary along z (vertical) direction.

CHAPTER 4:
CALIBRATION
&
SENSITIVITY ANALYSIS

4.1 General points

This chapter deals with the calibration of the numerical model, presentation of the results detailed with the calibrated model such as electric potential distribution, stress, voltage drop at the interface etc., and discussions of the sensitivity analysis (SA) on some parameters.

Sound calibration is an inseparable part of a reliable simulation process. ECF model setup (experimental setup) was used to record electrical potential at various uniform temperatures (400°C-950°C) at several positions inside the model's components. Several probes were inserted in the different parts of the ECF model to record electrical potential. Virtual sensors were implemented in the numerical model (half block) at the same positions so that the results obtained from both models (experimental and numerical) could be compared. Figure 4.1 illustrates a schematic representation of the sensors from one principal view. For experiments strategy, refer to section 3.2.5.

To calibrate the model, instead of a trial-and-error approach, sensitivity analysis (SA) was chosen, which is more sophisticated and systematic that can lead to efficient conclusions rapidly. Five pairs of positions were chosen to calibrate the numerical model; nevertheless, the voltage drop between Ref. probe and the average of sensors CA1/CA2 readings was the most important one to calibrate the parameter influencing the initial air gap at the cast iron to carbon interface. In order to calibrate the electrical resistance of carbon a strategy was taken such that the difference of potential between the average of CF1/CE1 readings and the average of CF2/CE2 readings was considered. Moreover, the difference of potential between the average of CA1/CA2 readings and the average of CE2/CF2 was considered for calibration.

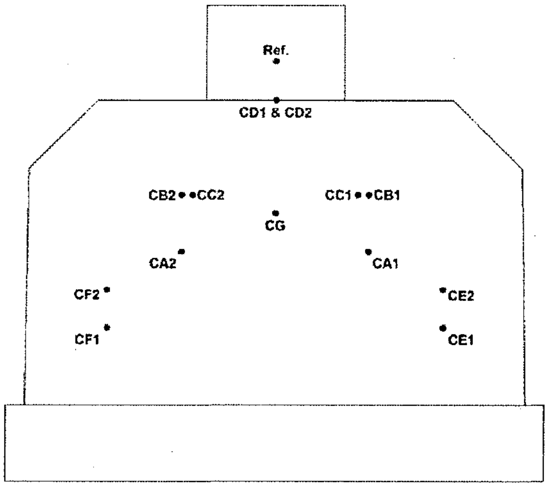

Figure 4.1: Voltage probes configuration

For the sake of simplicity and briefness, when discussing and analyzing the results, “at lower temperatures” and “at higher temperatures” will be used to refer to the lower or higher temperatures of the experiment range meaning 400°C-950°C.

4.2 Calibration

A series of parameters were taken into account in a specific order shown in the next sections to calibrate the model. The **start model** using the initial values for parameters was called “**Base model**” (or simply “Base” on the charts). After each series of simulations on a single parameter, a decision was made to choose the best fitting value of that parameter and the remainder of the simulations (in the list) were executed with employing the updated model. The final (updated) model after carrying out all of the simulations needed for the calibration phase was considered as the “calibrated model”; and then, was used for the SA simulations under the name “Base”.

The calibration phase consists of two main steps: 1) calibration of numerical parameters and 2) calibration of physical parameters. The former involves tuning the parameters that are a part of the fundamental equations and not the problem to be solved e.g. normal penalty number, which is a parameter to adjust the accuracy of the contact conditions. Normal penalty number does not directly originate from any of the physical parts of the experimental model or the physics of the problems to be solved during the simulation such as: conduction, thermal expansion, contact and so on. In fact, the main purpose of calibration of numerical parameters is to adjust the model to make sure it will converge. Unlike numerical parameters, physical parameters, as the name denotes, deal with the physics of the problem and the involving physical parameters such as frictional coefficient and electrical resistivity of carbon. In the previously mentioned list of calibration parameters, initial five ones are numerical and the remainder is the physical parameters to be adjusted during the calibration process which will be explained in detail in the following sections.

It should be noted that the parameters taken into account for the calibration depend on the available information obtained from experimental tests too. For example if electrical resistance of carbon is known through experimental tests (of the exact material) it will not be included in the list of the parameters to calibrate. To be more specific, as an example, in this work, electrical resistance of anode carbon obtained by Wilkening and Côté [33] was used instead of electrical resistance of the actual anode carbon. Although they have pretty much the same pattern, the values of resistance at various temperatures must be adjusted for the half block model. The experiments to evaluate anode carbon resistivity is an ongoing work and once the results are at hand, they can be fed directly to the model and electrical carbon resistance must be removed from the list of calibration parameters.

4.2.1 Initial parameters for calibration

To calibrate the model, the values below were chosen as the starting point based on the experience and expectations:

- Tolerance in distinguishing air gap zones: 1 mm
- $K_n=10^{11}$ N/m^3
- $K_t=10^{-3}\times K_n$ N/m^3
- At the stub/connector and carbon/support interface: MPC with $K_n=K_t=10^{10}$ N/m^3
- Transition gap: 1 mm with $R_{C,max}=5000\times R_C$ Ω-m^2 at g=0
- At cast iron/carbon interface: $\mu=1.0$
- $T_{ph}=250°C$

K_n and K_t are the normal and tangential penalty numbers respectively. μ is the frictional coefficient. Note that the remainder of the initial parameters such as the lateral gap of the flutes are not single values and are considered to be explained in their corresponding sections.

4.2.2 Considered parameters for calibration

The following parameters were employed in order to investigate the sensitivity of the output with respect to their systematic change:

Numerical

1. Tolerance on the fillets (determining initial gap zones)
2. Normal penalty
3. Tangential penalty
4. Penalty number of MPC interfaces
5. Transition gap

Physical

6. Frictional coefficient
7. Initial air gap (T_{ph})
8. Initial air gap (lateral gap of flutes)
9. Electrical resistance of carbon (horizontal)
10. Electrical resistance of carbon (vertical)
11. Electrical resistance of carbon (horizontal & vertical)

4.2.3 Calibration of numerical parameters

Since the main purpose of the calibration of the numerical parameters is simply to make sure of the convergence of the numerical model, it is not necessary to use experimental data in this step; however, the experimental results were also included in the figures to have a view of where these data stand compared to the results obtained from the numerical model.

As explained in section 3.7 (Initial air gap), employing equations (3.1) and (3.2) to create the final geometrical entity, the initial air gap at the cast iron/carbon interface is required to determine three zones of the initial air gap. In the abovementioned section, there is a detailed discussion about the tolerance parameter which was also shown in figure 3.23. It was expected that the tolerance parameters have an important influence on the accuracy of the results since it controls the distribution of the initial air gap at the cast iron/carbon interface. The results proved the expectation was right.

One point which should be borne in mind before reviewing calibration and SA results in this chapter is that to respect the NDA with RTA, the results obtained from the ECF model as well as those obtained from the numerical model were normalized to [0,1]. The maximum value (on the Y axis) solely was set to 1 and the other values were divided by the maximum value. A conventional normalization requires setting the minimum value to 0; however, it was not applied in this case to keep the pattern of the curves as close as possible to the actual results. For the sake of brevity, only the results of some sensor pairs (and not all 5 pairs) are presented in this document, chosen according to the importance of the graphs in the process of calibration or SA.

4.2.3.1 Tolerance on the fillets

Figure 4.2 demonstrates the results of the experimental and base model compared to the case in which the tolerance was set to 3 mm. Notice that the default value for the tolerance as mentioned before was 1 mm. The results prove that the default value for the tolerance was good so it must be retained for the next simulations. The figure shows the relative voltage drop between probes CA and Ref. This has been indicated in the caption of the figure. The same method has been applied to the remainder of the figures in this chapter.

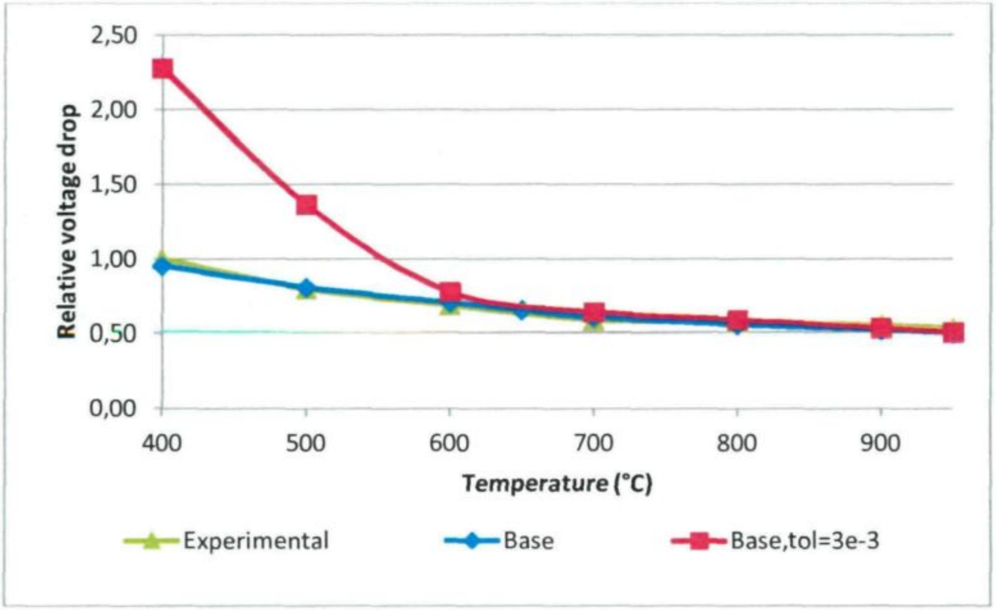

Figure 4.2: Sensitivity on the air gap zones tolerance parameter (CA-Ref)

It can also be seen that the model responded extremely differently at the lower temperatures. It shows the accuracy of the model below 600°C is enormously dependent on the tolerance parameter. In other words, proportionality of the areas attributed to the zones of the initial air gap has an impact on the voltage drop, particularly at the lower temperatures. Considering the air gap zones and the tolerance parameter elaborated in the initial air gap section (section 3.7) a larger tolerance parameter results in taking account of a higher percentage as the cylindrical portion and the tip of the flutes. These two zones typically have larger gaps compared to the sides of the flutes. The result will be a larger effective air gap and therefore, a larger voltage drop, especially below 600°C. Thus, distinguishing the initial air gap zones accurately is crucial. More simulations in the process of calibration revealed the reason for such reactions, which will be discussed later in this section.

4.2.3.2 Normal penalty number

Normal penalty number was the second numerical parameter to be adjusted. The results illustrated in figure 4.3 evidently prove that $K_n=10^{11}$ N/m^3 was a perfect choice as default value. One simulation with a smaller value ($K_n=10^{10}$ N/m^3) resulted in a curve with a huge discrepancy compared to the experimental results. The other two simulations with higher values could not be completed due to convergence problems. According to the penalty method to simulate contact, the contact pressure is calculated through allowing two bodies in contact to penetrate, but this is not the case in practice. Applying this method, the exerted contact pressure is calculated proportional to the magnitude of penetration. The value of proportionality is in fact the penalty number; nevertheless, it must be an appropriate value to adequately evaluate the contact force. Usually one single penalty number is used to simulate contact in a model; however, an advanced approach could be to attribute a different (specific) penalty number to each contact pair according to a specific tolerance for the residual penetration.

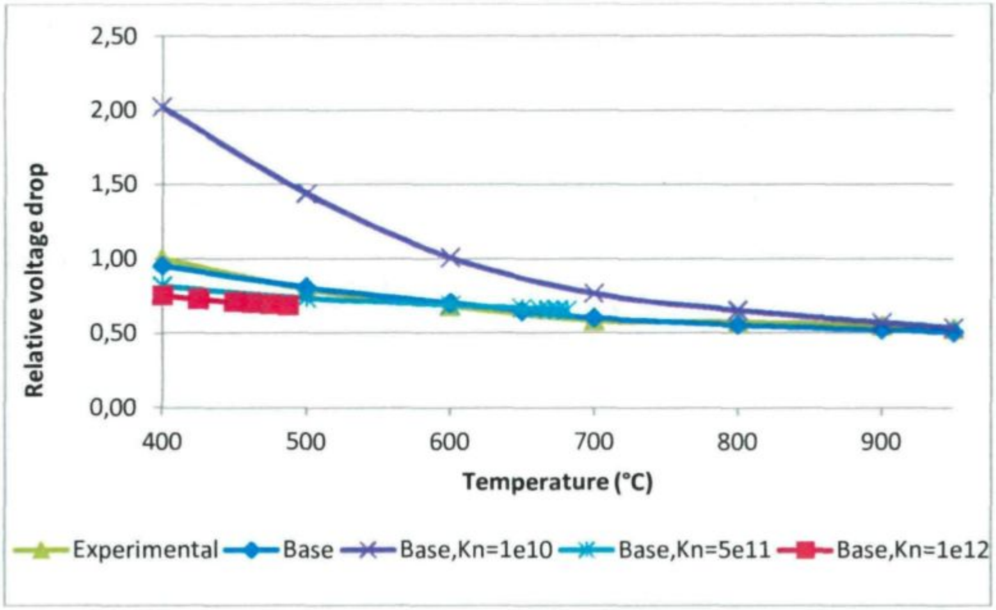

Figure 4.3: Sensitivity on the normal penalty number (CA-Ref)

The results of the SA on the normal penalty number of $K_n=10^{10}$ N/m^3, which is in fact 10 times smaller than the default value, were far from accurate. The discrepancy was generally noticeable all over the temperature range, and extremely noticeable, i.e. larger, at the lower temperatures. The SA results of two simulations with a higher penalty number compared to the default value gave less voltage drop, approximately 75-82% of the experimental value at 400°C. The case of $K_n=10^{12}$ N/m^3 could not make it through to 500°C due to numerous bi-sectioning between 400° and 500°C, which denotes difficulty converging. The same scenario happened in the case of K_n=5e11, but between 600°C and 700°C. Although one bi-sectioning occurred between 600°C and 700°C for the base case, the solution process converged successfully.

4.2.3.3 Tangential penalty number

It is a convention in the numerical methods to choose a tangential penalty number 1000 times smaller than the normal penalty number, but this still needed to be verified during the calibration process. If a larger value is needed, a larger tangential penalty number is chosen. However, the number should not exceed the normal penalty number [see 45]. Results obtained from the simulations on the sensitivity of the model on the tangential penalty number revealed that the default value was not appropriate and had to be adjusted to $K_t = 10^{11}$ N/m^3 as per figure 4.4. Notice that the value is equal to that of normal penalty and a larger value was not chosen according to the convention explained above.

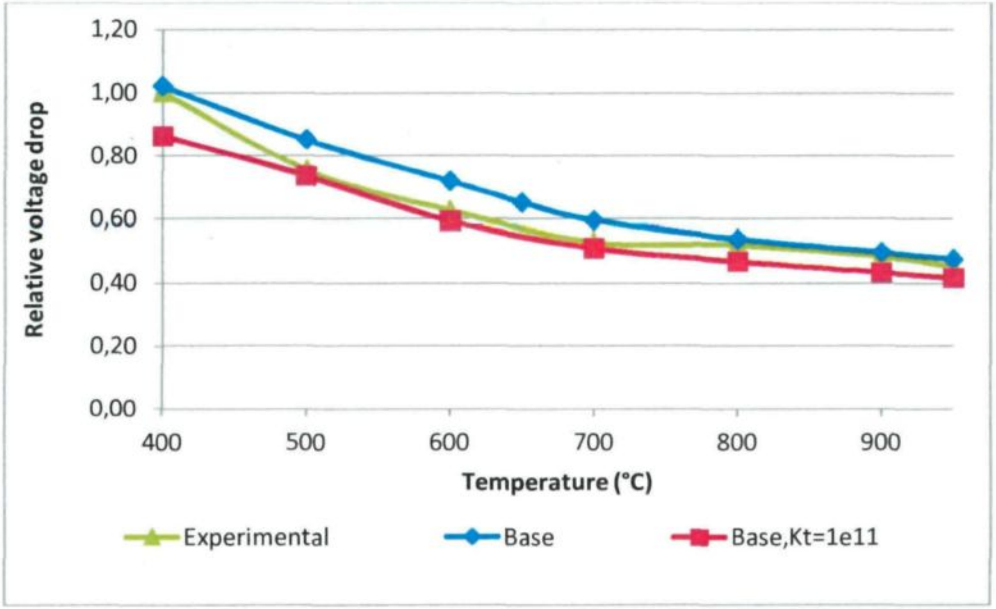

Figure 4.4: Sensitivity on the tangential penalty number (CG-Ref)

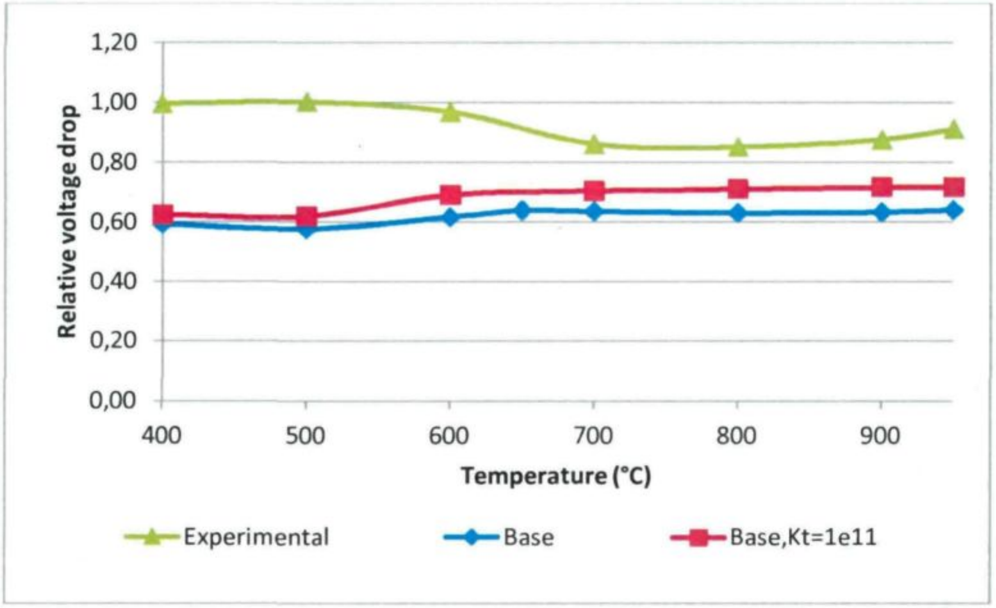

Figure 4.5: Sensitivity on the tangential penalty number (CG-CA)

4.2.3.4 Penalty number of MPC

As described in the interface and contact section (section 3.3), two interfaces, support to carbon and stub to cast iron, were set to have an MPC. To investigate whether the penalty number of the MPC interfaces had an effect on the output of the model, a simulation with normal and tangential penalty numbers 10 times larger compared to the base case was applied. The result as illustrated in figure 4.6 showed that the impact is negligible. Thus, the default values were kept for the next simulations.

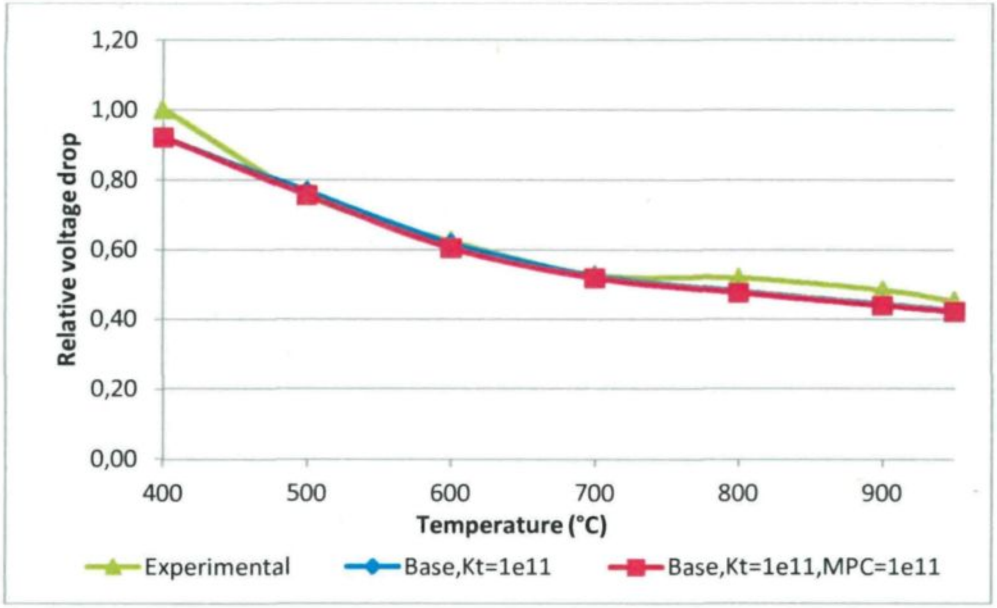

Figure 4.6: Sensitivity on the penalty numbers of MPC at stub/connector and carbon/support interfaces (CG-Ref)

4.2.3.5 Transition gap

The fifth numerical parameter to calibrate was the transition gap. The results of a simulation carried out with a transition gap value of 1 μm proved that the model had no considerable sensitivity to this value as illustrated in figure 4.7. tg in this figure represents the transition gap.

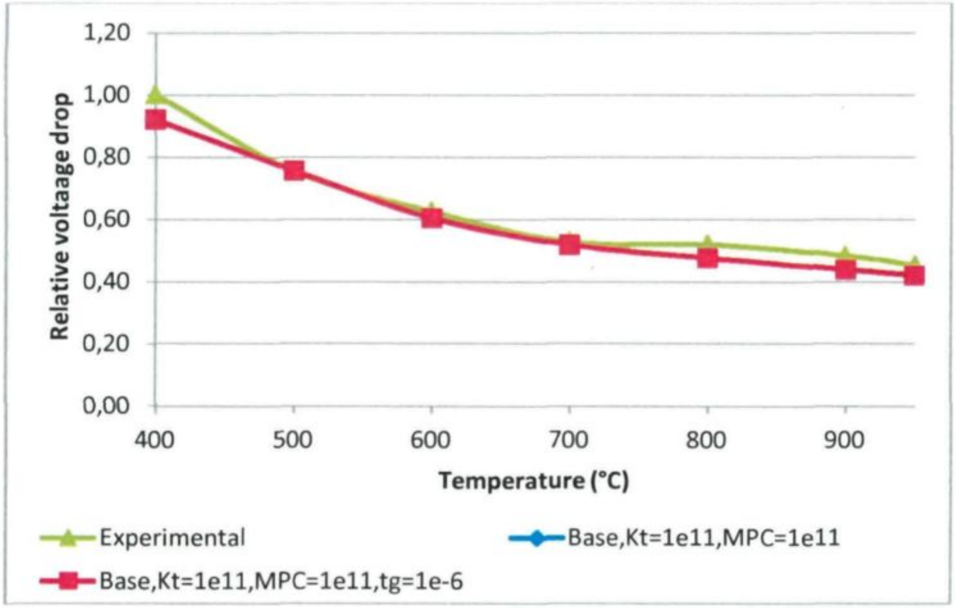

Figure 4.7: Sensitivity on the transition gap (CG-Ref)

At this point, the model is calibrated for the numerical parameters; nonetheless, some of the physical parameters must be calibrated since they have not been obtained from experiments. A detailed discussion will be laid out in the next section.

4.2.4 Calibration of physical parameters

4.2.4.1 Frictional coefficient

Frictional coefficient (μ) is essential in solving frictional contact problems and cannot be neglected without making sure of purely bound contact. In the case of the cast iron connector and carbon contact, the results of calibration as shown in figure 4.8 and figure 4.9, unraveled that a small frictional coefficient was the best fit. The reason is likely that the micro particles of carbon at the interface, which act like a lubricant and , eventually, decrease friction between two materials drastically. Frictionless assumption may also result in satisfactory results.

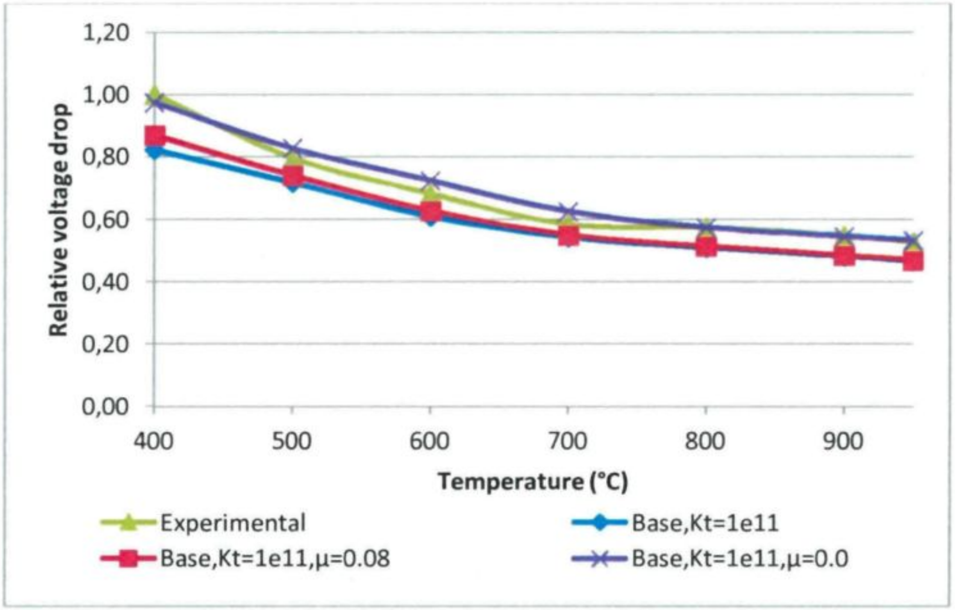

Figure 4.8: Sensitivity on the frictional coefficient (CA-Ref)

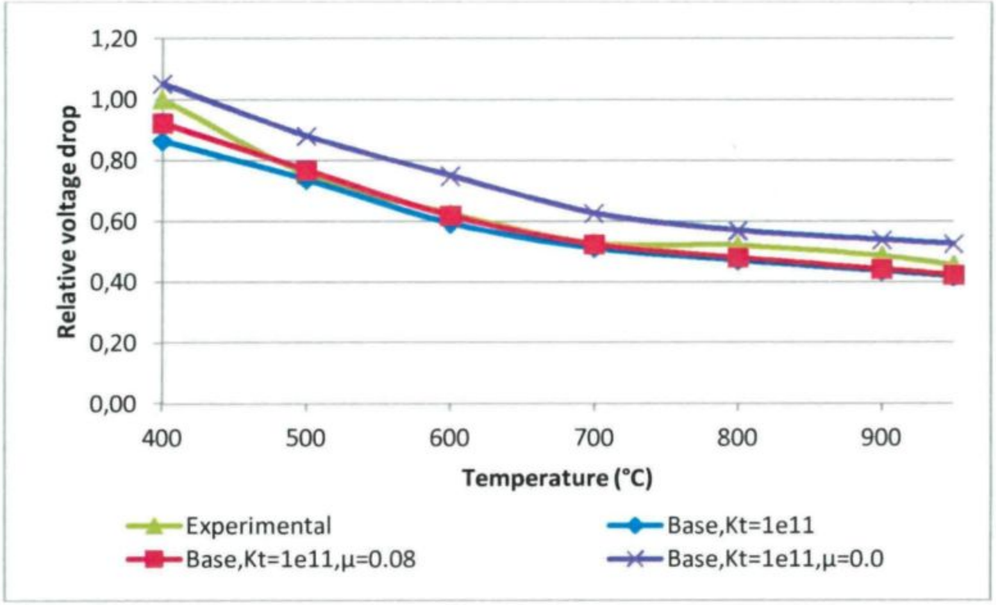

Figure 4.9: Sensitivity on the frictional coefficient (CG-Ref)

From the abovementioned figures it is clear that the frictionless case resulted in a higher voltage drop compared to the experiments. This is more evident in figure 4.9 which illustrates the relative voltage drop between probes Ref. and CG. A very high coefficient of friction gave almost the same results especially for the higher temperatures compared to the base case. This could be due to the geometry of the stub hole and flutes. After some heat up, the cast iron connector has a tendency to move higher, but since it is bound with the stub hole through its flutes inside the corresponding slots on the stub hole wall, it gets to a bound contact condition. In fact, the contact pressure is high enough to keep two surfaces together, so assuming a frictionless contact may not affect the results much. Coulomb's law of friction, presented in equation (4.1) explains this easily. f being the frictional force generated along the surfaces in contact is the amount of force to be exceeded by the tangential force to initiate motion (sliding). μ is called static Coefficient of friction and N is the normal force applied perpendicularly to the surfaces in contact.

$$F_T = \mu N \tag{4.1}$$

The overall shape of the stub hole is imperfect conical. Expanded stub and cast iron connector, due to the increase in temperature, are pushed upward; however, flutes are constrained in the slots and limit the movement. More increase in temperature may result in larger contact forces and, consequently, higher normal forces applied at the contacting surfaces (flutes side and slots sides). This way, contact established at the slots of the stub hole is constrained. Wherever the slots are much larger than the flutes, the coefficient of friction can play a more important role since sliding contact may occur. In such cases, assuming frictionless contact may be questionable.

Figure 4.10 demonstrates the results of calibration considering the probes CA and CG. The discrepancy of the experimental and numerical results in the chart may imply at the first look that the numerical results were not good; but, according to their absolute value (absolute voltage drop, not relative) which were few millivolts, and also, considering error tolerance, the results were in the right range. Furthermore, as mentioned earlier in this chapter, CA1 and CA2 were the main probes to measure voltage drop at the cast iron/carbon interface and the other measurements were used additionally for confirmation purposes. The CG-CA pair covers the region below the stub hole about which there is not much information on what exactly takes place in that region.

The reason could be the interface (or pancake) between the stub bottom and the stub hole bottom, which can get into different conditions, and the current may or may not go through this interface. In case of having contact at this interface, the current pattern below the interface will be hugely dependent on the location of contact points at the interface. In almost all of the works presented so far, there is no current going through this interface. It is reminded that in this work very high contact resistance was applied to the interface and the results were in a good range compared to the experiments.

Another reason could be the high variability of the electrical resistance of the carbon around the stub hole region. This area is not a perfectly known area to which it is difficult to assign reliable properties.

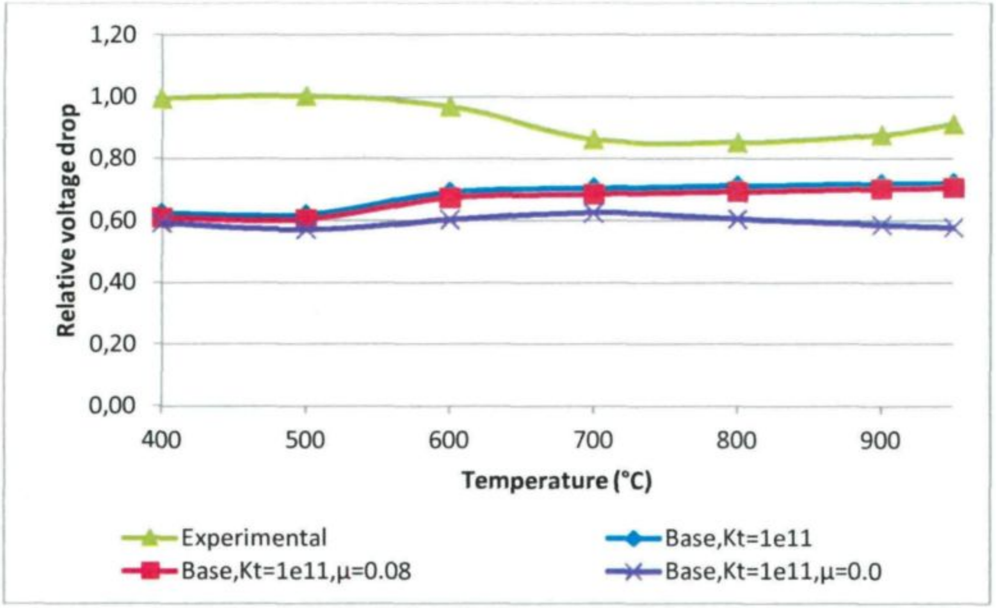

Figure 4.10: Sensitivity on the frictional coefficient (CG-CA)

4.2.4.2 Initial air gap distribution: effective stub temperature (Tph)

According to the evaluation of the initial air gap distribution at the cast iron/carbon interface (stated in section 3.7), T_{ph} was supposed as a calibration parameter. With all of the parameters of equations (3.1) and (3.2) being on hand except for T_{ph}, the results of the simulations with a systematically varying T_{ph} can be compared to the experimental results to find the fitting T_{ph}.

According to equations (3.1) and (3.2), T_{ph} contributes towards radial expansion of stub and cast iron connector and has no impact on the magnitude of the flutes' lateral gap. That being said, one more step would be needed to calibrate the initial air gap completely. In other words, in calibrating T_{ph} only two zones of the initial air gap namely cylindrical portion and tip of the flutes will be adjustedand thus, the flutes' lateral gap must be tuned through another series of simulations.

A comparison of the relative voltage drops obtained from four simulations with different values of T_{ph} to the relative voltage drop of the base case and the experimental one is illustrated in figure 4.11 and figure 4.12 . Generally higher T_{ph} values resulted in higher relative voltage drops. This can be also concluded from equations (3.1) and (3.2) where a higher T_{ph} will give a larger γ (stub contraction); and consequently, a larger gap. As explained previously, with a larger initial gap contact pressure is weak and thus the voltage drop increases.

The voltage drop at 400°C and 500°C did not change at all after exceeding the default T_{ph} value of 250°C. From 600°C the model showed more sensitivity to the T_{ph} values higher than 250°C. It simply signifies the voltage drop until 500°C is not controlled by the cylindrical portion and flutes tips. The only remaining part of the whole contact area would be flute sides, which must be validated through SA on the lateral gap of the flutes. T_{ph} value of 300°C which was the best case was selected and the base case was updated to be used for the next simulations.

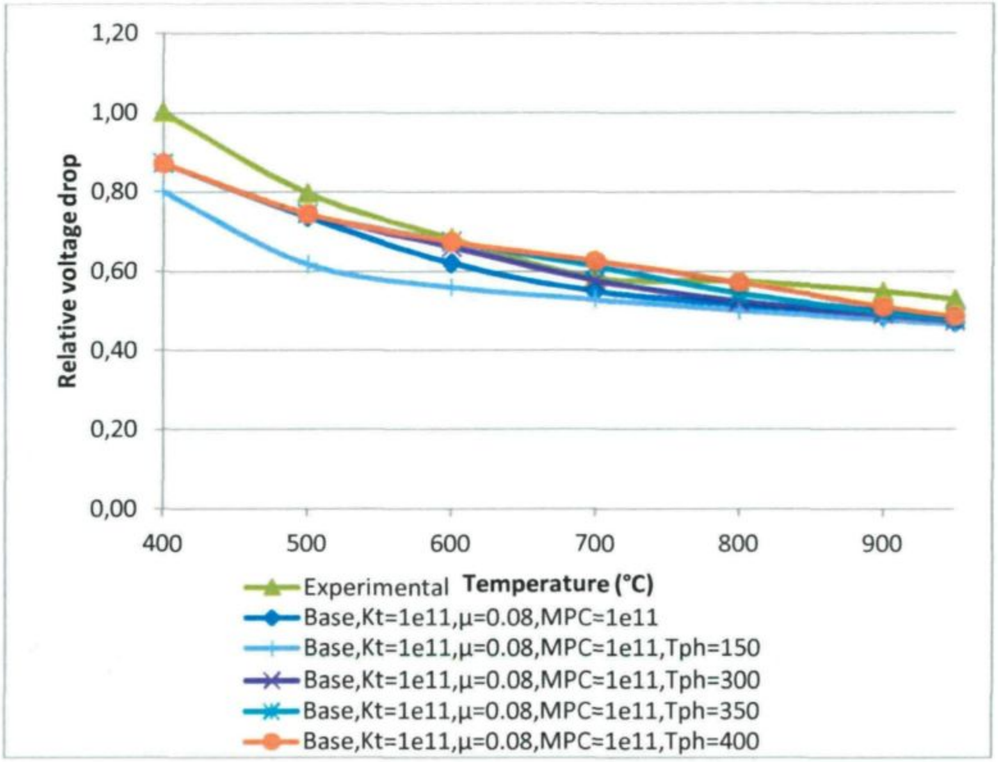

Figure 4.11: Sensitivity on the T_{ph} (CA-Ref)

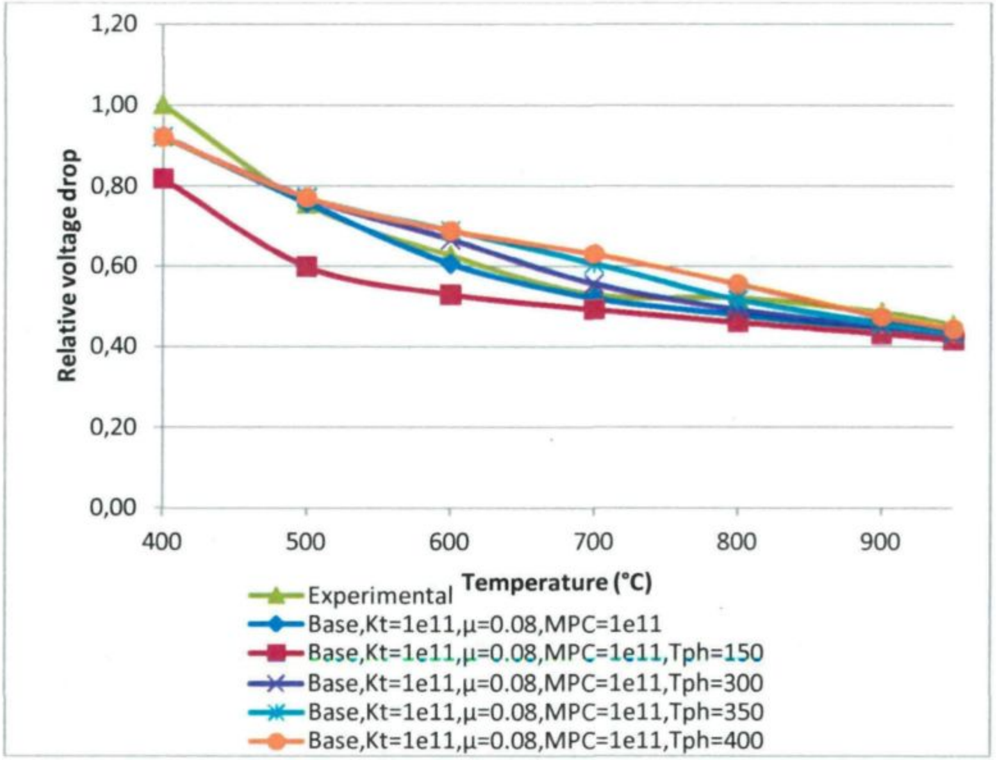

Figure 4.12: Sensitivity on the T_{ph} (CG-Ref)

4.2.4.3 Initial air gap distribution: lateral gap of flutes

Following the SA simulations on the initial air gap, the initial lateral gap of the flutes in the updated base case was set to 120%, 140% and 160% of its default value and the results were compared as shown in figure 4.13 and figure 4.14. At first glance it can be noted that the discrepancy of the curves starts with a maximum amount and decreases as temperature increases. At 700°C and higher temperatures, the curves are almost identical, indicating that the lateral gap does not affect the total voltage drop after 700°C. The output of the simulations corroborates the hypothesis of the previous section, suggesting that the voltage drop is controlled by the sides of flutes at lower temperatures. It seems that contact establishes first with the sides of the flutes and then spreads to the cylindrical portion as well as tips of the flutes. This can be verified by studying contour plots of contact at the cast iron/carbon interface, which will be presented in section 4.2.5.

One important point that should be borne in mind here is that the method used to vary the lateral gap here must originally be done by changing the coefficient of thermal expansion.

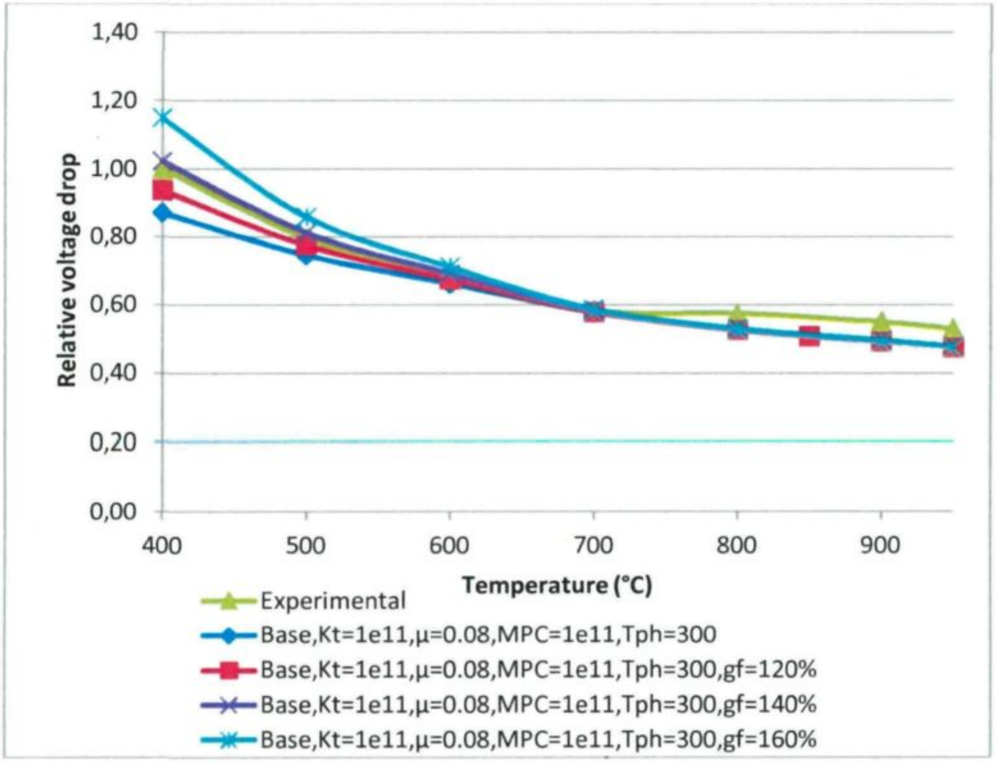

Figure 4.13: Sensitivity on the lateral gap of flutes (CA-Ref)

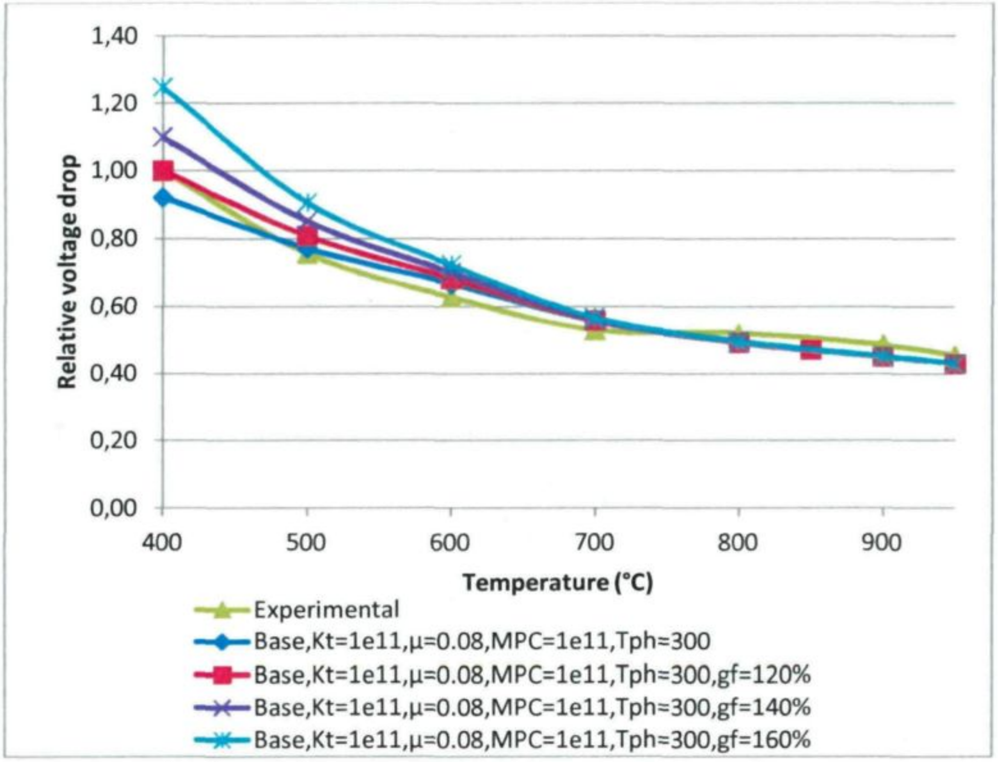

Figure 4.14: Sensitivity on the lateral gap of flutes (CG-Ref)

4.2.4.4 Electrical resistance of carbon (horizontal)

Since the electrical contact resistance of anode carbon of Wilkening and Côté [33] was used in the numerical model (instead of anode carbon resistivity obtained from experimental tests), it was needed to adjust carbon resistivity for both horizontal and vertical directions since carbon is generally considered orthotropic considering the fabrication process. To calibrate the electrical resistance in the horizontal direction, two simulations were carried out with 10% higher and lower resistance than the base case value. The comparison of the output with the experiments shown in figure 4.15 and figure 4.16 revealed that anode carbon was 10% more resistive than the default value for the horizontal direction (XY plane which is parallel to the carbon bottom surface). Notice that figure 4.16 reflects the voltage drop caused (partially) by the stub and connector bottom interface and the area below the stub hole bottom, which is an unknown area in terms of current density

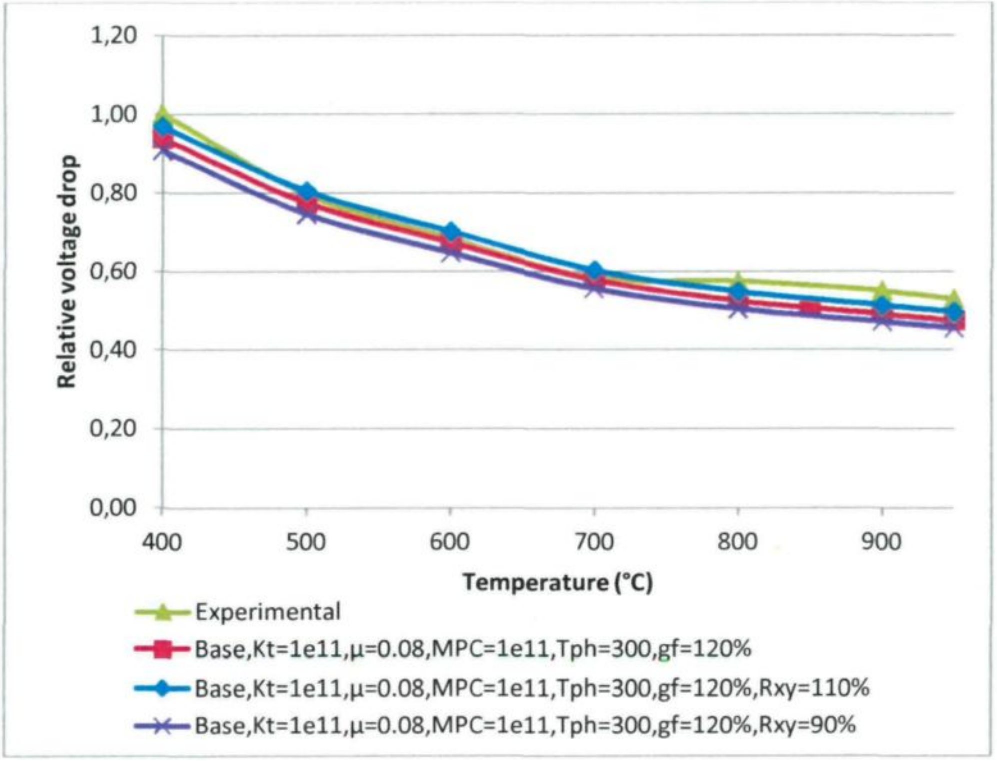

Figure 4.15: Sensitivity on the electrical resistance of carbon-horizontal direction (CA-Ref)

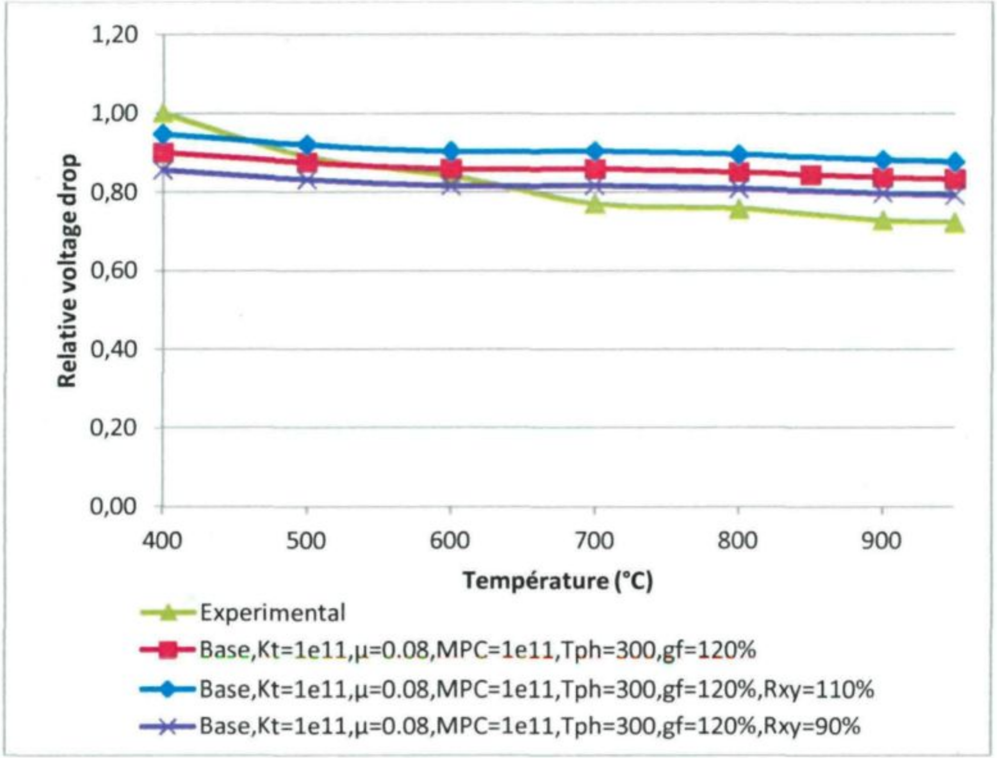

Figure 4.16: Sensitivity on the electrical resistance of carbon-horizontal direction (CG-Ref)

4.2.4.5 Electrical resistance of carbon (vertical)

The strategy to calibrate the vertical electrical resistance of carbon was the same as that used to adjust the horizontal electrical resistance. The results of simulation with a 10% variation to the base case were compared. Figure 4.17 which illustrates the relative voltage drop between probes CG and Ref, as an example, corroborates the idea that sensors inside carbon must be used to calibrate carbon resistance and also that they should be sufficiently far from each other to reflect a reasonable relative voltage drop. Despite the fact that the vertical distance of these two probes is long enough (see figure 4.1), only a short fraction of the distance is carbon and therefore, a significant discrepancy cannot be seen in all of the results. In figure 4.18 and figure 4.19, which illustrate the relative voltage drop among the probes inside carbon, such a discrepancy originating from the sensitivity of the model to the vertical resistance of carbon can be easily noted. Anode carbon was 10% less resistive in the vertical direction (Z direction which is perpendicular to the bottom surface of carbon). This could be due to the anode fabrication process where carbon experiences vertical pressing, which consequently makes carbon denser (more compact) in the vertical direction.

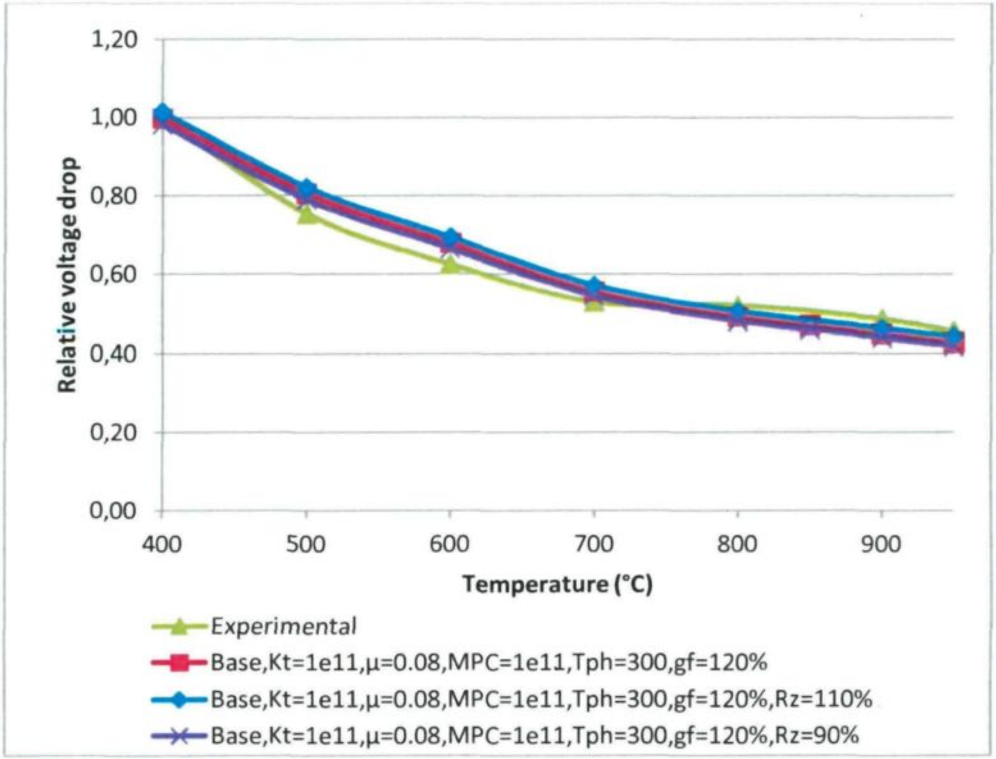

Figure 4.17: Sensitivity on the electrical resistance of carbon-vertical direction (CG-Ref)

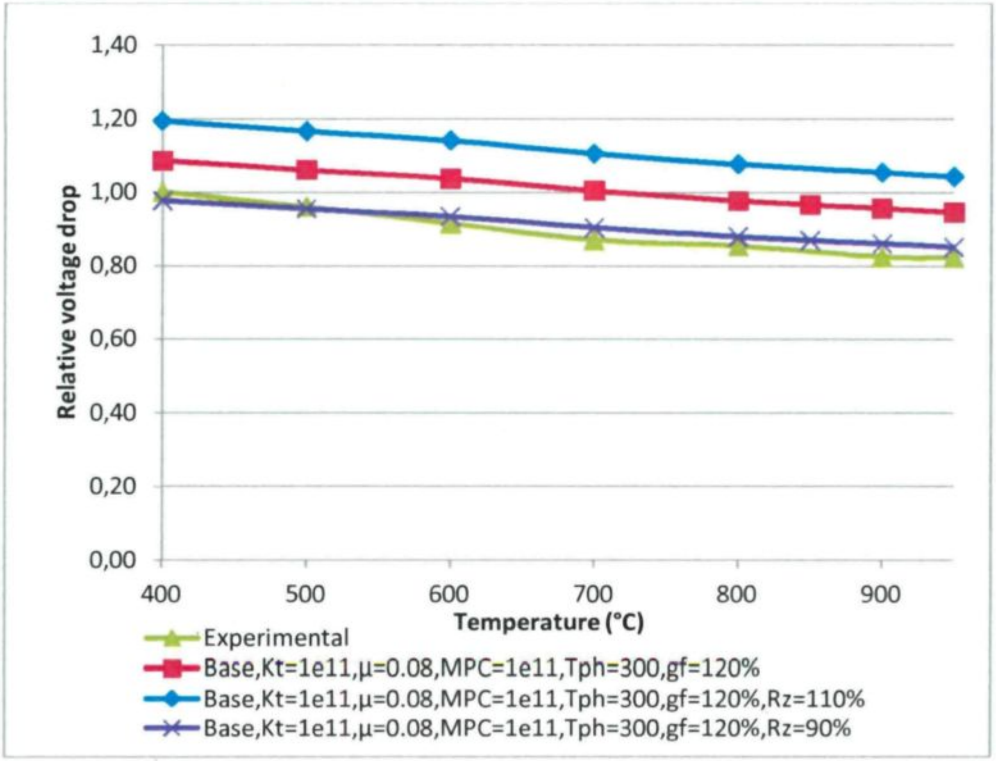

Figure 4.18: Sensitivity on the electrical resistance of carbon-vertical direction (CE1,CF1-CE2,CF2)

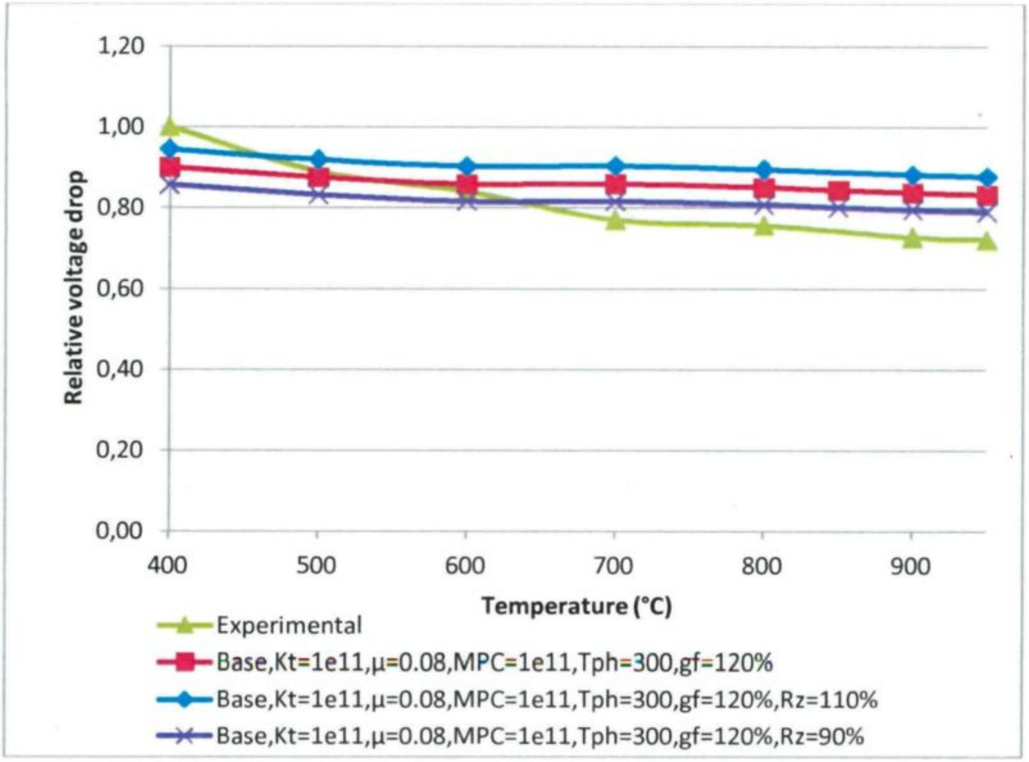

Figure 4.19: Sensitivity on the electrical resistance of carbon-vertical direction (CA-CE2,CF2)

4.2.4.6 Electrical resistance of carbon (horizontal & vertical)

After analyzing both horizontal and vertical resistance of carbon separately, to see the effect of both on the results, the new values namely 110% of horizontal value and 90% of the vertical value of the base case were employed and the output was as figure 4.20 and figure 4.21 for two comparison cases. The accuracy of the results as it can be seen in figure 4.20 was excellent; however, some deviation can be seen in figure 4.21. This is a relative comparison and to have a better judgment, absolute values must be considered. The origin of such kind of error could be various sources such as: error in positioning the probes in the experimental model, error in reading the values of electric potential, error caused by impurity of carbon between two probes (hairline cracks, pores) etc. It is clear these errors are inevitable, but they should be in a reasonable range. It should be borne in mind that the probes in the experimental model have a certain physical size whereas their corresponding virtual sensors in the numerical model are supposed as points. This dictates a range of tolerance to be considered. Considering the possible origins of the errors and using absolute values of the readings by the probes, it was concluded that the discrepancy of the curves (results) in all of the cases including the case of figure 4.21 was in a reasonable range.

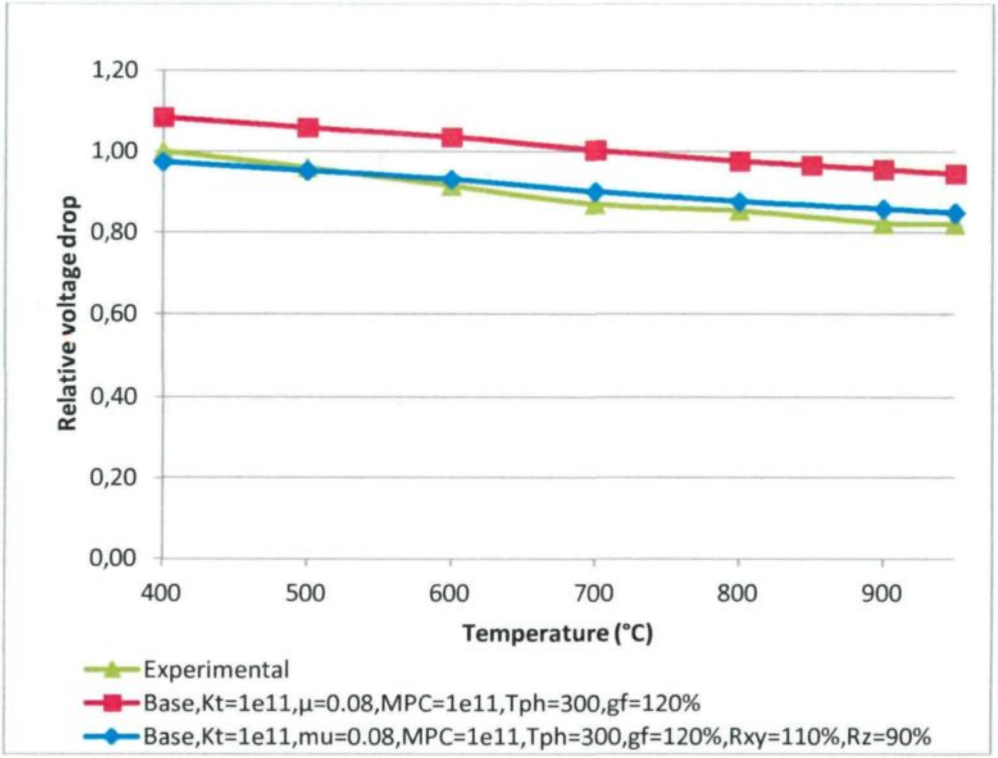

Figure 4.20: Sensitivity on the electrical resistance of carbon-horizontal and vertical directions (CE1,CF1-CE2,CF2)

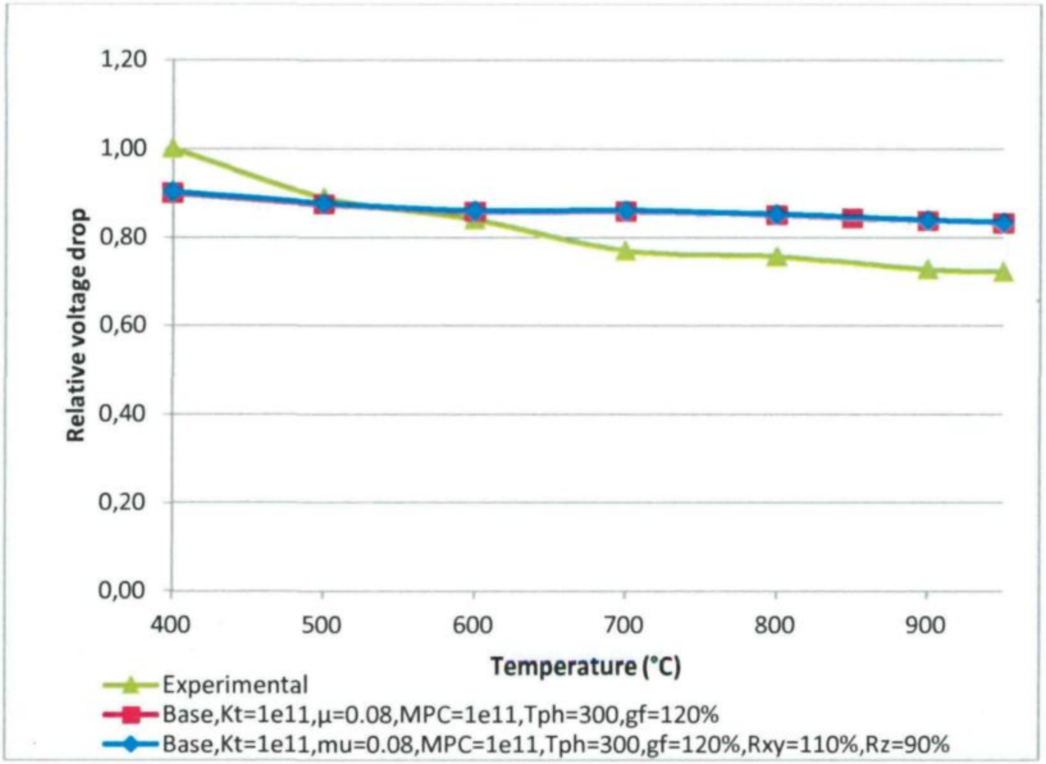

Figure 4.21: Sensitivity on the electrical resistance of carbon-horizontal and vertical directions (CA-CE2,CF2)

At this point the model is considered calibrated and ready to be used to carry out sensitivity analyses. Nevertheless, it is better to investigate and analyze other aspects such as potential distribution, current density, stress etc. before going through more analyses. A series of this sort of investigation is given in the next section.

4.2.5 Investigation of the calibrated model

Apart from voltage drop, the results should be better understood in terms of other engineering concepts such as stress, contact, current density, temperature and potential distribution in order to make sure that recommendations for optimization purposes are also within a reasonable range. In other words, voltage drop cannot be the only criterion for the system optimization; however, it remains one of the most important one. It should be kept in mind that optimization was beyond the scope of the work presented here and the discussions in this section are only for the purpose of better understanding. Also optimization needs to take account of the real condition in which the anode undergoes high thermal gradient. Since a constant and uniform temperature was applied at each step, temperature distribution is not among the contour plots to investigate. The Joule effect could cause some heat generation which may change the temperature distribution especially in the stub hole region; nevertheless, in all of simulations, the maximum generated heat by the Joule effect was approximately 8°C at 950°C. Therefore, the difference made in the temperature distribution could be neglected in terms of investigating the temperature distribution. It should be noted that the heat generated by the Joule effect and consequent change in the temperature was considered in the calculations.

To better cover the range of experiment temperatures, 400°C, 700°C and 950°C were chosen to plot the results in this section. This way, the evolution and changes could be seen to a satisfactory extent and in brief as well. When visualizing the results, minimum and maximum values in the legend of the plots were set to fixed values so that colors represent the same range in all of the results of simulations at different temperatures. Thus, the plots can be compared easily to both see evolution with respect to temperature and to draw conclusions. In addition, the minimum in all of the plots is represented with blue and the maximum is represented with red. For confidentiality reasons, the legends of the results have been eliminated in the public version of this document. Plots with legends are presented in appendix G.

4.2.5.1 Electric potential distribution

From figure 4.22 through figure 4.24 which demonstrate 3D contour plot and cross sectional plots of potential distribution in the calibrated model, it can be seen that at 400°C voltage drops drastically when passing the cast iron/carbon interface. This is in accordance with the fact that at lower temperatures contact resistance is higher.

As stated in the boundary conditions section, the bottom of the carbon block has been set to zero voltage, shown in blue in the contour plots. Thus, it can be concluded that the electric potential at the top of the stub where the electric current is imposed to the model also represents the total voltage drop.

At 400°C, potential in the stub which is represented in red is the maximum. As the temperature is increased, the electric potential in stub decreases and reaches its minimum at 950°C. Also, from all of the plots, it can be seen that the electric potential in the middle of the whole carbon block, where there is an empty half stub hole, is lower compared to the opposite side. This is due to the fact that the electric current has the tendency to pass through the shortest possible path to the bottom of the carbon block. In other words, the tendency is to flow vertically rather than horizontally.

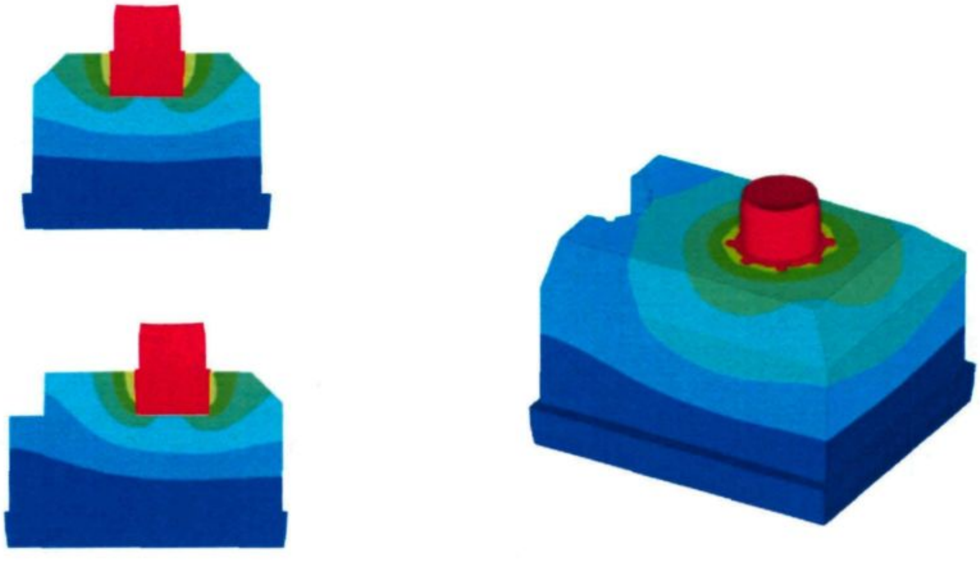

Figure 4.22: Potential distribution at 400°C

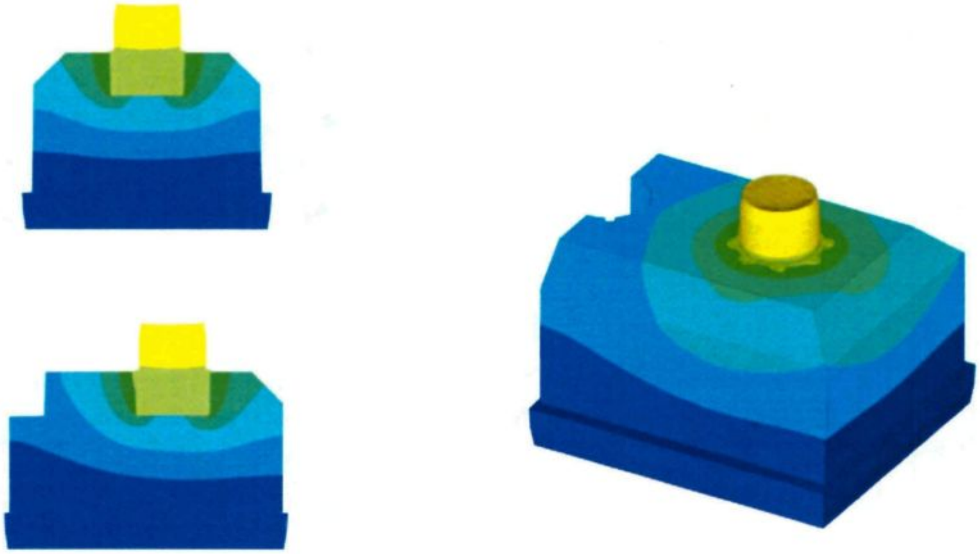

Figure 4.23: Potential distribution at 700°C

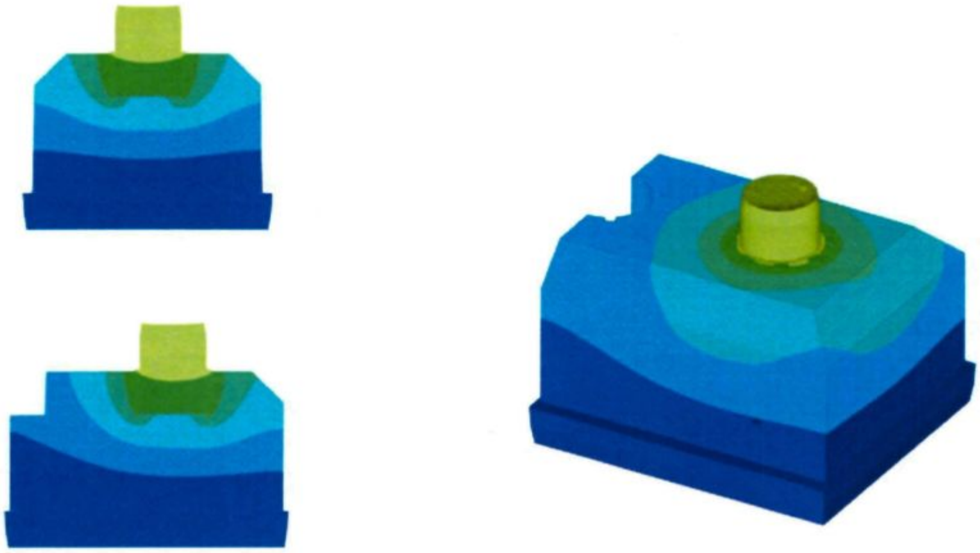

Figure 4.24: Potential distribution at 950°C

4.2.5.2 Stress distribution

Carbon used in the anode assemblies of different designs has approximately 30 MPa and 5-8 MPa of ultimate compressive and tensile strength respectively. It is clear that with a fairly low tensile strength, carbon is prone to fail or damage under tension. That being said, the first principal stress (S1) becomes an important criterion to be checked for any design or optimization recommendations.

The 1^{st} principal stress distribution plots show an increasing tensile stress with an increasing temperature. Stress at 700°C is higher than it is at 400°C as presented in figure 4.25. At 950°C the maximum tensile stress reaches its pinnacle around the stub hole region as shown in figure 4.26. The green in the contour plots represents a stress between 4 to 15 MPa; thus, considering an ultimate strength of 5MPa, carbon failure is possible. Since linear elastic material was used for carbon, the model cannot predict possible failure or damage. However, it is thought that actual carbon material could tolerate localized high stress through local material failure, which does not necessarily result in a crack and follow-up propagation. In some cases, though, cracks were witnessed.

A point that must be borne in mind is that it is conceived that in the real electrolysis cells (realistic operating conditions) the effective stub hole area does not exceed 700°C-800°C and therefore carbon may not reach the stresses that it does at 950°C. The maximal stress at 950°C exceeded 59 MPa on the surfaces of the flute slots in the stub hole which can be seen in red in figure 4.27. In spite of the very high stress on some parts of the flute slots' surface, the dominant stress range in the material is still 4MPa-15 MPa (green). The consequence of such high stress in the material cannot be easily determined unless a more developed constitutive law is used for carbon. Hence, it is highly recommended that with using a realistic constitutive law for carbon, damage and cracking prediction can be added to the features of the model, which makes it a more robust tool. Such a constitutive law has been developed by G. D'Amours [44] but it has not been considered in any anode assembly model presented thus far. This is an ongoing project at the CURAL which will be added to the model as soon as it is ready.

Figure 4.25: 1st principal stress (tensile) at 400°C (left) and 700°C (right)

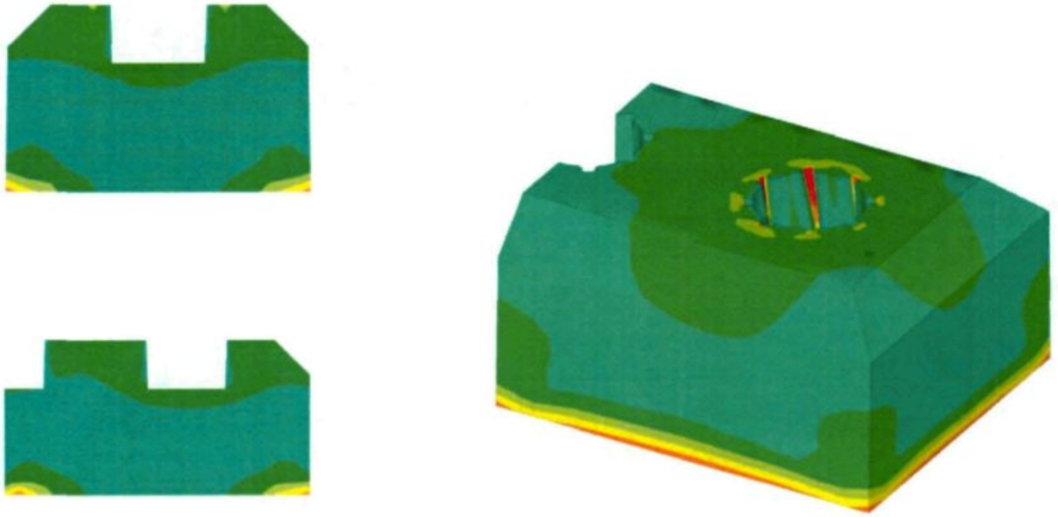

Figure 4.26: 1st principal stress (tensile) at 950°C

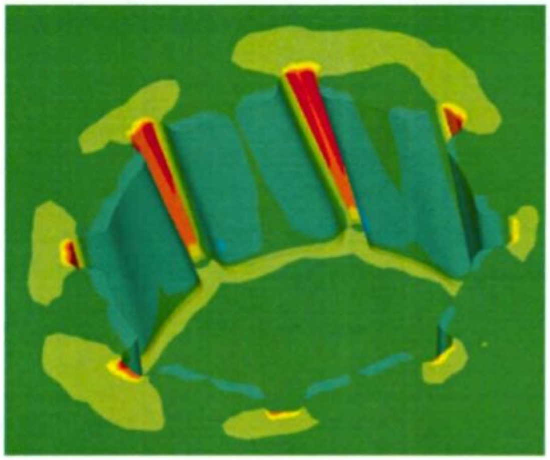

Figure 4.27: 1st principal stress (tensile) distribution in stub hole region at 950°C

The 3rd principal stress helps understand the maximum compressive stress induced in the model due to the loading conditions. Since carbon is much more resistant to compressive stress than to tensile stress (30 MPa vs. 5 MPa), no damage or failure due to compression is expected. This can be seen in figure 4.28 where stress reaches 7 MPa (green) almost globally at all of the test temperatures. At 950°C, which is considered the most critical case, the stub hole region and the bottom parts of the carbon block reach 18 MPa (light blue). Similar to the 1st principal stress case, carbon, in some local parts on the edge of flute slots exceeded 30 MPa; however, no visual damage was recorded in the experiments. Again, the stub hole area at 700°C did not tolerate any stress higher than the ultimate compressive strength of 30 MPa.

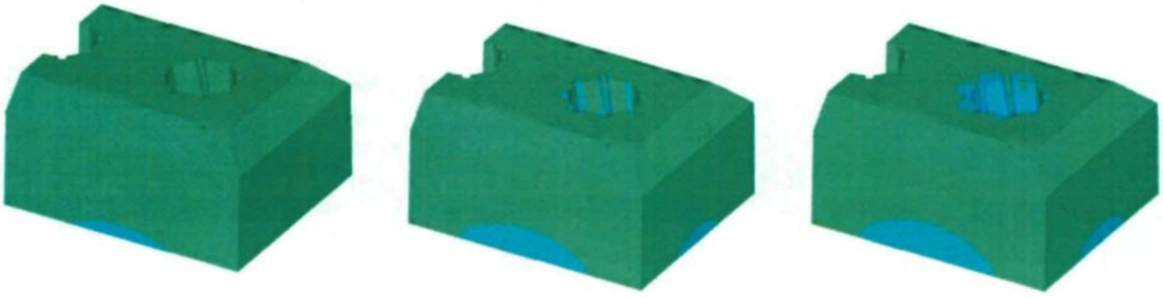

Figure 4.28: 3rd principal stress (compressive) distribution at 400°C (left), 700°C (middle) and 950°C (right)

4.2.5.3 Current density

Comparing the current density distribution in the cast iron connector at 400°C, 700°C and 950°C presented in figure 4.29 confirms other researchers' findings that more current is drawn from the lower parts of the cast iron due to the tendency of the electric current to flow through the shortest path to the bottom. Also it is clear that with an increasing temperature (from left to right) more current is drawn, since contact resistance at the cast iron to carbon interface decreases.

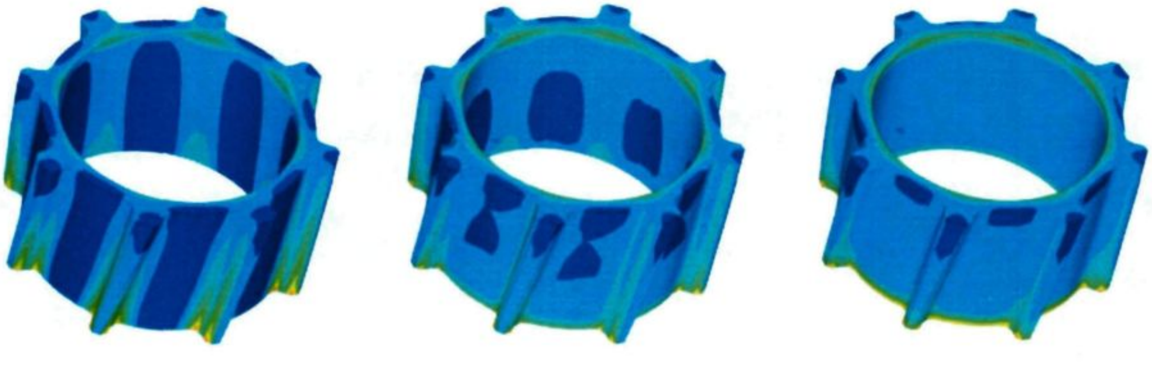

Figure 4.29: Current density in the cast iron connector at 400°C (left), 700°C (middle) and 950°C (right)

The contour plot of current density at 400°C unravels that the current is drawn much more from the lower parts of the flutes' sides. This must be due to the fact that contact is established primarily at those parts. This will be corroborated with the study on contact in one of the following sections.

4.2.5.4 Interfacial voltage drop

Due to the importance of the cast iron to carbon interface, the voltage drop is visualized using contour plots. Figure 4.30 illustrates three contour plots of the voltage drop at 400°C, 700°C and 950°C at the cast iron/carbon interface generated by the abovementioned tool.

Figure 4.30: Voltage drop at the cast iron to carbon interface at 400°C (left), 700°C (middle) and 950°C (right)

From the plots it can be seen that with an increasing temperature the voltage drop decreased generally. Voltage drop should not be confused with contact resistance. It should be noted that the voltage drop is the production of contact resistance and current density, so the voltage drop is not necessarily higher where the contact resistance is higher. However, the upper parts of the interface still showed high resistance and caused high voltage drop in general. In addition, once again, plots showed that the voltage drop was minimal at the lower parts of the flutes' sides particularly where they are connected to the cylindrical portion. This will be investigated much more in the contact evolution section.

4.2.5.5 Contact condition

Without a doubt, contact quality controls the voltage drop at the cast iron to carbon interface. Hence, scrutinizing contact at this interface is crucial. Contact status has been visualized for three temperatures in figure 4.31. The legend presented for the contact status plots in figure 4.31 is mainly used as an indication of the quality of contact. The range between 0 and 1 is assumed no contact condition. This range has been color-coded with different shades of blue. Approaching 1 and exceeding is interpreted as establishing contact, while contact in the range of 1 to 2 is considered sliding contact. It is assumed that with exceeding 2 contact turns to sticking due to enough contact pressure, which is better in terms of quality.

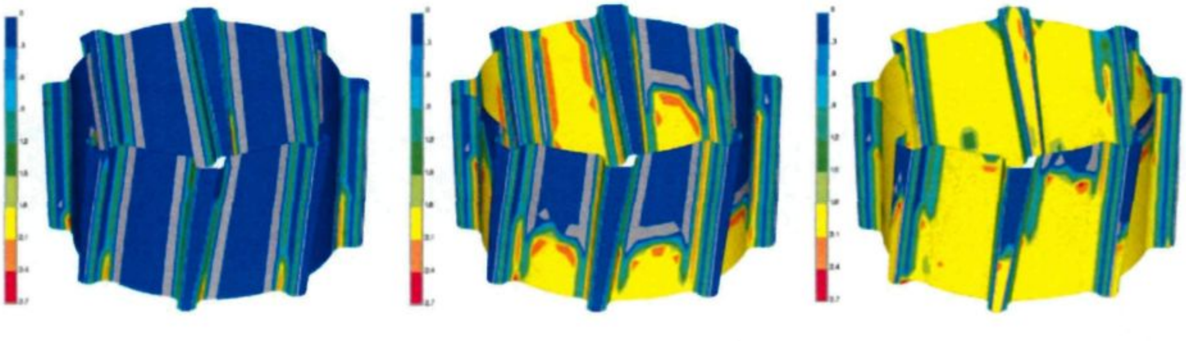

Figure 4.31: Contact evolution at the cast iron to carbon interface at 400°C (left), 700°C (middle) and 950°C (right)

From the left side plot, presenting the contact status at 400°C, it can be clearly seen that contact is established at the sides of flutes at their lower part. This is in agreement with what was seen during the calibration process, where the lateral gap of flutes controlled the voltage drop from 400°C to approximately 600°C and from there, other zones (cylindrical portion and tip of the flutes) took the lead. The middle plot, which is the contact status at 700°C, confirms this statement. The contact status at 900°C shown in the right side figure is the best case among all three since a higher percentage of the surface contributes to contact. However, it should be noted that the stub hole and surrounding materials will not reach higher temperatures such as 950°C in the real application. It is believed that the (effective) temperature in the stub hole is around 650°C in practice [see 40]; nevertheless, since the analysis was done for a brand new anode, it is expected that with carbon consumption during operation, this temperature rises as the anode assembly is lowered; and thus, it gets closer to the 950°C-960°C bath temperature which acts like a heat source of constant temperature.

In addition, *in situ* measurements of temperature inside carbon during its lifespan by RTA were used to roughly evaluate the temperature inside carbon around stub hole. The results showed that on day 3 of the carbon block's lifespan, the temperature range can be approximately 695°C at the top surface of carbon, disregarding heat convection that transfers noticeable heat energy and lowers the temperature. At the level of the bottom of stub hole (130 mm from top surface) the temperature was around 750°C. On day 18 or later, the temperatures were 870°C and 890°C respectively. It should be noted that lower temperatures are expected inside the stub since stubs are metal and highly conductive; thus, a noticeable amount of heat energy is transferred through conduction and also convection where stub surfaces are exposed to air. Given this, it is conceivable that in reality the effective average temperature in stub hole could be between 600°C and 800°C (700°C ±100°C). Hence, the middle figure is a good representation of a realistic hypothesis about how contact status would look in operation. A thorough analysis of temperature distribution inside a stub hole during the carbon's lifetime in operation has yet to be carried out, but would provide more clues.

In addition to the voltage drop tool for the cast iron to carbon interface, some tools were also implemented to extract some statistical facts. Using those tools, the contact area percentage at each temperature was determined. The contact areas for all of the abovementioned cases from left to right were 12%, 42% and 70% respectively. It is evident that if the temperature of the stub hole drops, for example to 600°C, contact quality will be poorer and voltage drop will increase remarkably. The total contact area could be a good indication of contact efficiency, but contact can be different in terms of quality and more parameters should be taken into account.

Considering that the total contact area increases with an increasing temperature, it is expected that the cast iron to carbon interface show a higher performance last days of its lifespan rather than in the initial days since it gets closer to the bath; and thus, the temperature in the stub hole increases. This will be elaborated in section 4.3. Unlike the higher quality of contact at the end of the carbon's lifespan and less voltage drop at the interface, the total voltage drop in the anode assembly not only does not decrease but actually increases as carbon is consumed during operation. This is due to the higher resistivity of metal components (such as rod, yoke, stubs and cast iron) at higher temperatures. The accumulated voltage drop of components of the anode assembly increases since the decrease in the voltage drop at the interface is simply not enough to compensate for the accumulated increase stemming from higher resistivity of the metals at higher temperatures.

A deeper investigation on the evolution of contact area with respect to temperature illustrated in figure 4.32 and figure 4.33 unravels that the contact area ratio increases rapidly after 600°C. Interestingly, after reaching 700°C, the slope decreases slightly. To better understand the evolution of the contact area quantifying the relative rate of contact establishment would be a good idea. To do this, the slope of the contact area graph in figure 4.32 (or figure 4.33) between two consecutive temperatures on the x axis was calculated. The minimum value, which was the slope between 400°C and 500°C, was set to 1 and the rest of the slopes were calculated relatively to that slope as shown in table 4.1.

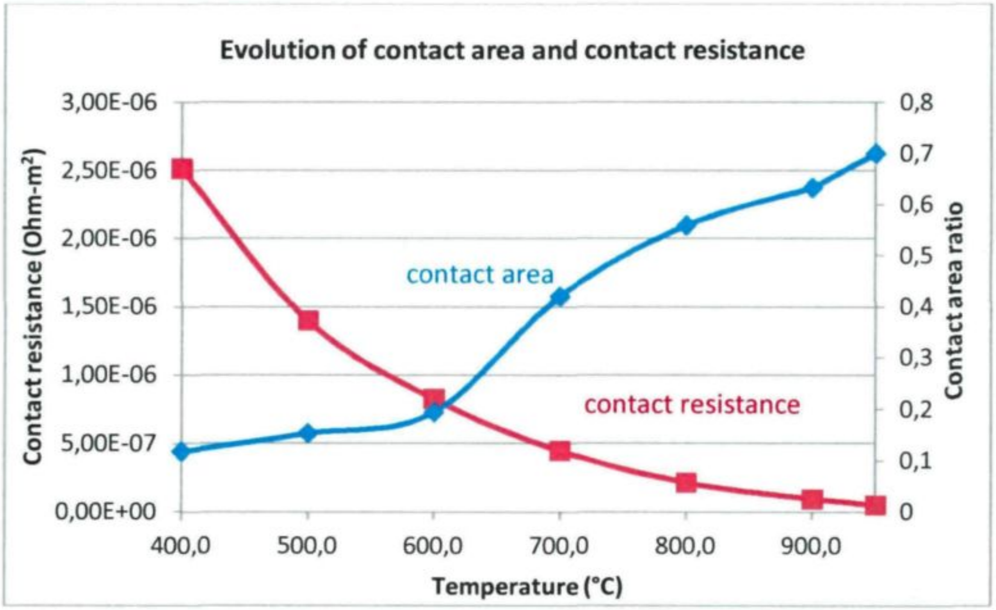

Figure 4.32: Evolution of contact area and contact resistance

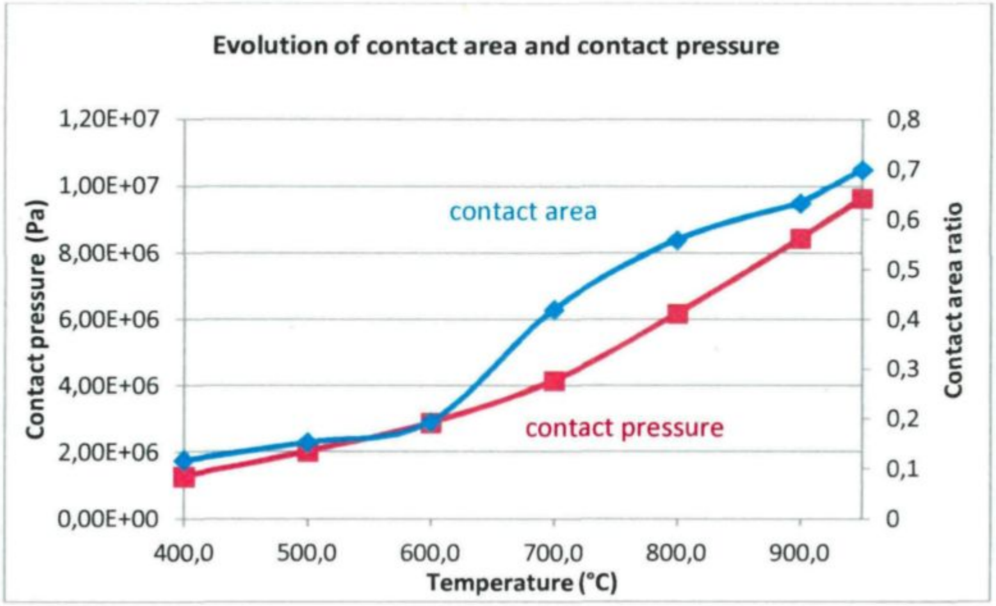

Figure 4.33: Evolution of contact area and contact pressure

From table 4.1 it can be seen that from 600°C to 700°C, contact area generation is drastic. The rate of contact establishment in the aforementioned range is 6.3 times compared to 400°C-500°C and 1.62 times compared to 700°C-800°C. Up to 600°C, the total contact area is only 19.39% of the total area at the cast iron to carbon interface while from 600°C to 700°C, an additional 22.53% of the total area contributes to contact which is more than the sum of the contributions up to 600°C. That said, it can be concluded that a slight variation of temperature between 600°C-700°C will have a relatively noticeable impact on the contact generation or loss. However, according to the explanation given earlier in this section concerning the contact status, it is not quite sure the consequent of this rapid increase will be enough effective to lower the contact resistance accordingly. This can be verified with using the information of contact resistance presented in figure 4.32.

Table 4.1: Contact evolution - statistical facts

Temperature Range	**400°C-500°C**	**500°C-600°C**	**600°C-700°C**	**700°C-800°C**	**800°C-900°C**	**900°C-950°C**
Voltage Drop Decrease (CA1,CA2)-Ref. [scaled]	0.2	0.11	0.10	0.01	0.03	0.02
Rate of Contact Establishment (Relative to Step 1)	1	1.14	6.3	3.88	2.05	3.76
Contact Area Generation (% of total area)	3.58%	4.09%	22.53%	13.89%	7.33%	6.73%
Relative Average Contact Resistance Decrease (relative to the precedent step)	-44.28%	-40.92%	-45.53%	-51.98%	-55.78%	-42.91%
Relative Average Contact Pressure Increase (relative to the precedent step)	58.97%	43.17%	43.83%	48.81%	36.52%	14.33%

In table 4.1, the relative decrease in contact resistance of each step of temperature increment is given. The values are approximately between 48% and 59%. The best case is the step between 400°C and 500°C, meaning that contact resistance at 500°C is 59.08% of that at 400°C. It should be noted that the last step is a 50°C increase while the other increments were all 100°C; thus, it is very likely that the contact resistance decline during an increase from 900°C to 1000°C could be much more than 57.09%.

Average values in all of the statistical facts were weighted by the area of interface contact elements; however, for the case of average contact resistance a better and more effective approach would be employing a weighted average by the current density as well. This is because the elements at the lower part of the interface contribute more in terms of allowing the current to pass through. In other words, the current density in the lower part elements is higher than it is in the higher part elements. Still, it can be concluded that the voltage drop is the main indicator. Normalized values used to illustrate the voltage drop in all of the charts presented in the calibration section have been also given in table 4.1. The voltage drop between the reference probe and probes CA1/CA2 at 400°C was normalized to 1. It can be seen that from 400°C to 500°C there is a 0.2 decline in the voltage drop, which was the maximal drop among all of the temperature increments. From 500°C to 600°C, the voltage drop declined 0.11 and 0.10 during two increments of 100°C. It is interesting to know that after 700°C there is almost no effective change in the voltage drop in spite of the increases in the contact area and the average contact pressure. This could be due to the fact that newly added contact area contributions to the total contact area after 700°C belong to the middle and higher part of the interface whereas current density is much lower compared to the lower part of the connector. This is visible in the plots presented in figure 4.29. Another reason, as aforementioned, would be the higher resistivity of the metal components, namely steel stub and cast iron in the half anode model. The contribution of each component to the voltage drop between probe Ref. and CA1/CA2 is unknown; however, a focus on the performance of the cast iron to carbon interface in the sensitivity analysis section reveals that the voltage drop decreases with an increasing temperature. The average contact resistance at the interface is relatively presented in table 4.1 for each increment. Additionally, the same type of change for the average contact pressure is also shown in the table. Both of series of data corroborate that the increase in the average contact pressure and the decrease in the average contact resistance at the interface are a sustained trending despite a slight difference in the momentum (rate) of trending in each temperature increment.

Figure 4.34 and figure 4.35 illustrate some more statistical facts that are in accordance with the conclusions drawn from the previous data. The change in the average current density during the temperature rise from 400°C to 950°C was not more than 1.6%, which is negligible. The average current density can be assumed almost constant along the temperature rise since a constant current was applied. Note that the area of the interface is assumed constant in this case. The negligible change originates from the strictness of the convergence criteria and/or approximation errors. Unlike the average current density, its standard deviation declined as shown in figure 4.34. A low standard deviation indicates that the data points tend to be very close to the mean, whereas high standard deviation indicates that the data points are spread out over a large range of values. In plain language, the current density is closer to a perfectly uniform current density distribution at higher temperatures. This is due to the fact that more contact area is generated at higher temperatures so the current can be spread all over the interface. However, attaining a perfectly uniform current density distribution is practically impossible since electric current is drawn more from the lower part of the cast iron connector.

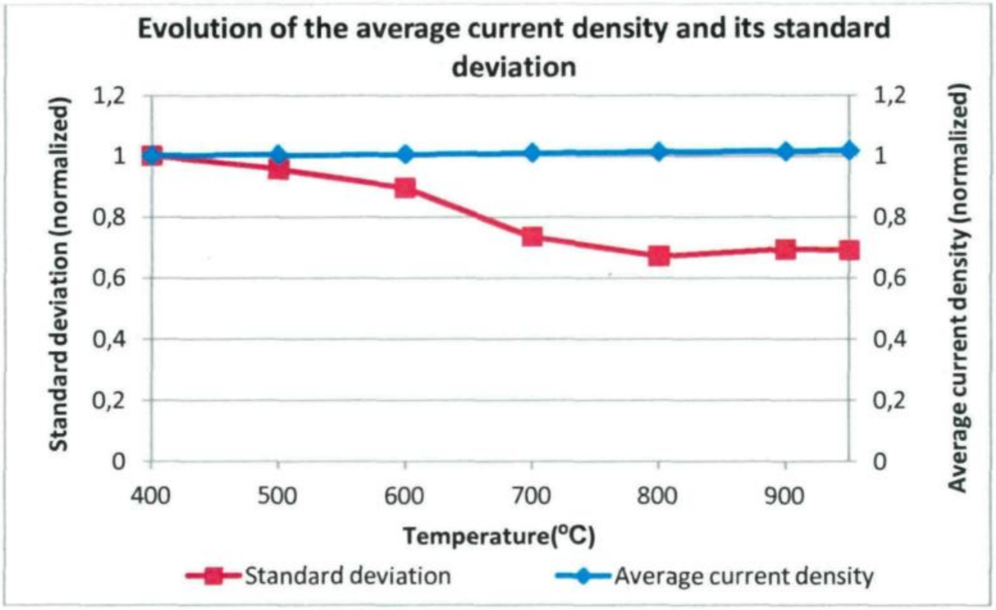

Figure 4.34: Evolution of the average current density and its standard deviation at the cast iron to carbon interface

Figure 4.35 illustrates how the average contact status at the interface evolves with respect to temperature. Like contact area generation, from 600°C to 700°C the average contact status rises rapidly. This increases the importance of this temperature range because not only does a remarkable percentage of the area at the cast iron/carbon interface contribute to the contact area, but also, the average contact status experiences a strong improvement.

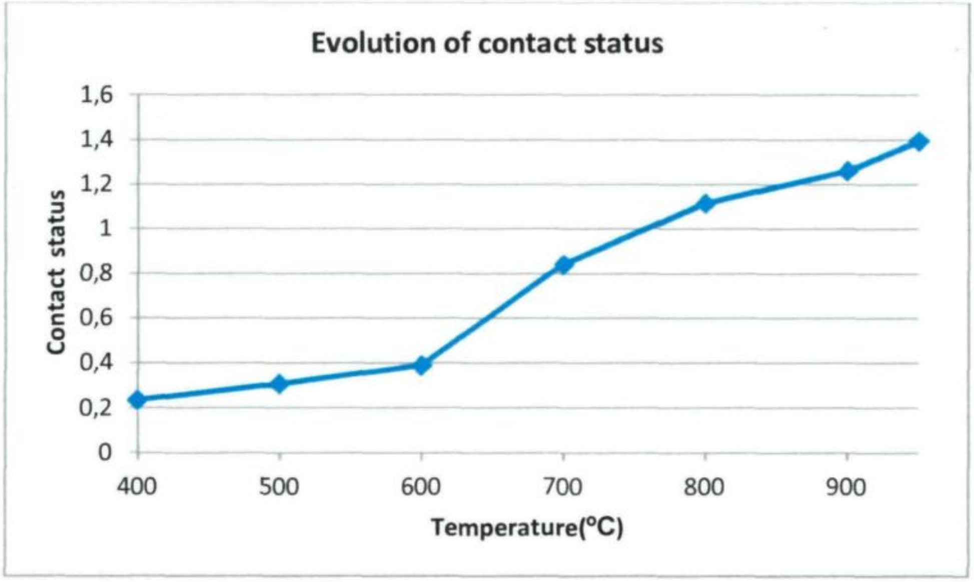

Figure 4.35: Evolution of contact status

As previously mentioned, in operation the temperature in the stub hole lies somewhere in 700°C ±100°C range where the total contact area may not even reach 50% of the total area at the cast iron to carbon interface. Thus, finding solutions to increase the contact area through geometrical (design) optimization or correcting the composition of the material in a way to get better contact would be a challenging but worthwhile goal. Sensitivity analysis will unravel some unknown points in course of better understanding the phenomena taking place at the cast iron/carbon interface which can be of great help for further development and optimization.

4.3 Sensitivity Analysis (SA)

Sensitivity Analysis (SA) is the study of how the variation in the output of a model (numerical or otherwise) can be apportioned, qualitatively or quantitatively, to different sources of variation in the input. [see 46]. This section presents the results that were obtained through simulations to evaluate the sensitivity of the model to some variables.

4.3.1 Considered parameters for SA

Once the model was calibrated with the experimental data, it was ready to be used to carry out some sensitivity analysis. Numerous and different types of SA could be carried out; however, the ones that could help understand the behavior of the materials of the model and the cast iron/carbon interface characteristics were given priority. Also, one study of geometrical sensitivity, namely, SA on the change in the diameter of the stub, was fulfilled. The parameters below were selected to perform SA and evaluate the impact of their change on the response of the model:

1. ECR (Electrical Contact Resistance) at the cast iron/carbon interface
2. CTE of steel, cast iron and carbon
3. Phase change of steel and cast iron
4. E & ν as a function of temperature (mechanical properties)
5. Electrical resistance of cast iron
6. Stub diameter

Note that in the charts illustrating SA results in this section, the calibrated model is referred to as "Base". Although it was not necessary to include the experimental results in the figures of this section after calibration, they are included to make it possible to easily compare those results with the SA results.

4.3.2 ECR at cast iron/carbon interface

It is well known that up to 25% of the anodic voltage drop is attributed to the cast iron/carbon interface [10]; however, since contact resistance is a function of temperature, it is expected to see variable contributions to the total voltage drop by this interface at different temperatures and pressures. To investigate the contribution of the interface to the total voltage drop, a simple strategy was chosen. Two simulations were carried out using a very little contact resistance applied to the interface. In one case, constant resistance of 10^{-12} Ω-m^2 was imposed. In the other case, the contact resistance at 950°C and 9.5 MPa was calculated and imposed on the interface. From the results illustrated in figure 4.36 it can be seen that both cases showed almost a constant resistance along the testing temperature range. A very slight decline in the voltage drop was seen in both cases; nevertheless, the decline was negligible. The discrepancy of the result of two cases with the base case makes a nearly triangular area roughly representing the contribution of the interface to the total voltage drop.

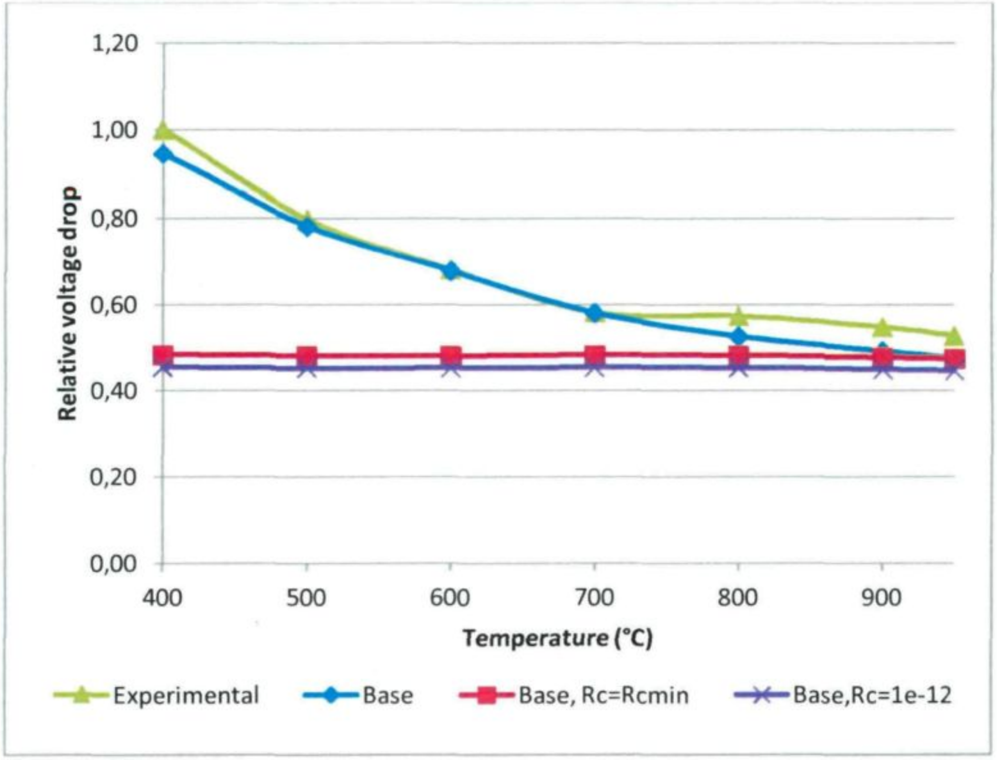

Figure 4.36: SA on the ECR at the cast iron/carbon interface (CA-Ref)

At 400°C the contribution of the interface to the total voltage drop is the maximum, which reaches 50%. With an increasing temperature up to 700°C the contribution decreases by an approximate amount of 10% with a 100°C increment. From 700°C to higher, the contribution falls down to 3% or less, comparing the results of the simulation with $R_C=10^{-12}$ $\Omega\text{-m}^2$ and the experimental results. However, comparing the results of the SA with the base case showed a sustained decline after 700°C to higher temperatures as shown in table 4.2.

Table 4.2: Decrease in contribution of cast iron/carbon interface to the total voltage drop between probes Ref. and CA

Temperature Range	**400°C-500°C**	**500°C-600°C**	**600°C-700°C**	**700°C-800°C**	**800°C-900°C**	**900°C-950°C**
Experimental $R_C=10^{-12}$	11%	10%	12%	1%	3%	3%
Base $R_C=10^{-12}$	10%	9%	11%	8%	5%	3%

These results were obtained using a uniform temperature, while in practice, temperature distribution is not uniform. Nonetheless, it is expected, assuming an effective temperature for the stub hole region, that these values give a good estimation for the contribution of the interface to the total voltage drop. Assuming an effective stub hole temperature between 500 °C and 700 °C as the possible effective temperature in the stub hole region, the contribution of the interface will lie somewhere between 22% and 44%. Interestingly these values are identical no matter whether experimental results or base case results are used to calculate the contribution of the interface to the voltage drop between Ref. and probes CA1/CA2. Using the total voltage drop in the model, these numbers are 14% and 29%. It is certain that the contribution of the interface to the total voltage drop in a whole anode assembly will be less since the voltage drop caused by the rod, yoke and the lower part of the actual carbon block which has been cut in the ECF model will be added. A more realistic simulation considering temperature gradient in the model will give a more precise evaluation of how the interface affects the total voltage drop with respect to temperature.

4.3.3 CTE of steel, cast iron and carbon

Six simulations were fulfilled with α_{steel}, $\alpha_{\text{cast iron}}$ and α_{carbon}, 90% and 110% of their base case values. Figure 4.37 through figure 4.39 demonstrate the results of the aforementioned SA. It should be kept in mind that the CTE of steel and cast iron have an influence on the initial air gap and thus, the initial air gap must be recalculated for the SA cases (90% and 110% cases). Also the CTE of carbon may have an impact on the geometry of the stub hole in the rodding process; hence, the thickness of cast iron may change. In this study, the geometry of the stub hole was assumed intact (during the rodding process) since the CTE of carbon is not as large as those of steel and cast iron; and therefore, the impact is negligible. Nonetheless, the CTE of carbon, if changed, can result in a change in the geometry of the stub hole. Apparently, different stub hole dimensions ensuing from the thermal expansion will create different contact conditions compared to the base case. With a different contact distribution, the voltage drop will change accordingly. That said, SA was also performed on the CTE of carbon to investigate its impact on the total voltage drop.

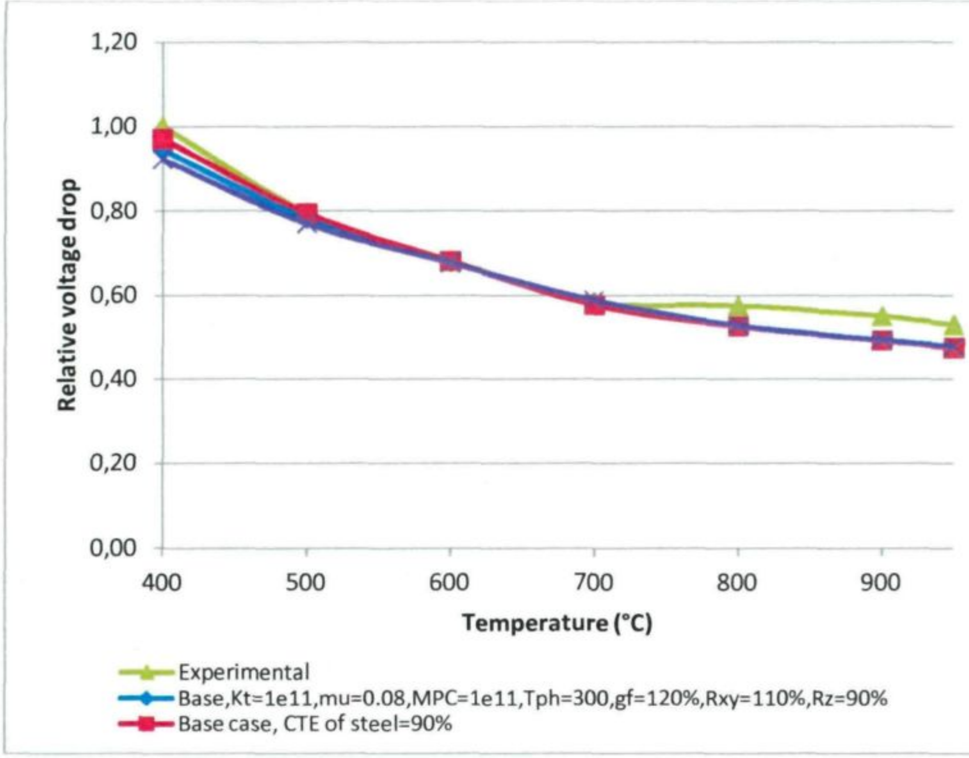

Figure 4.37: SA on the CTE of steel (CA-Ref)

It is clear from the results that the CTE change had an impact on the total voltage drop, marginally in some cases, and noticeably in some other ones. However, a higher CTE of steel or cast iron resulted in less voltage drop. This is in accordance with expectations since with a higher CTE, the expansion and subsequent contact pressure will be higher; and thus, contact resistance and consequently the voltage drop will be less significant compared to the base case. These results can be seen in figure 4.37 and figure 4.38. By comparing these figures with figure 4.39 it can be easily concluded that it is the opposite for carbon. With a higher CTE of carbon, at higher temperatures the stub hole will be larger; therefore, steel and cast iron will need to fill up more room compared to the base case and once it is filled, the remainder of expansion will provide contact pressure which will be less in this case. With a lower CTE of carbon, the gap is filled sooner and a higher percentage of the expansion is used to produce contact pressure. With a higher contact pressure, the voltage drop will be less according to the contact resistance curve. It should be stated that the curves for cast iron heating and cooling are not necessarily identical. This will have an impact on the size of the initial air gap and may result in different voltage drop values. In this study, one single dilatation curve was employed. This implies that the cooling curve is supposed identical to the expansion curve with respect to temperature.

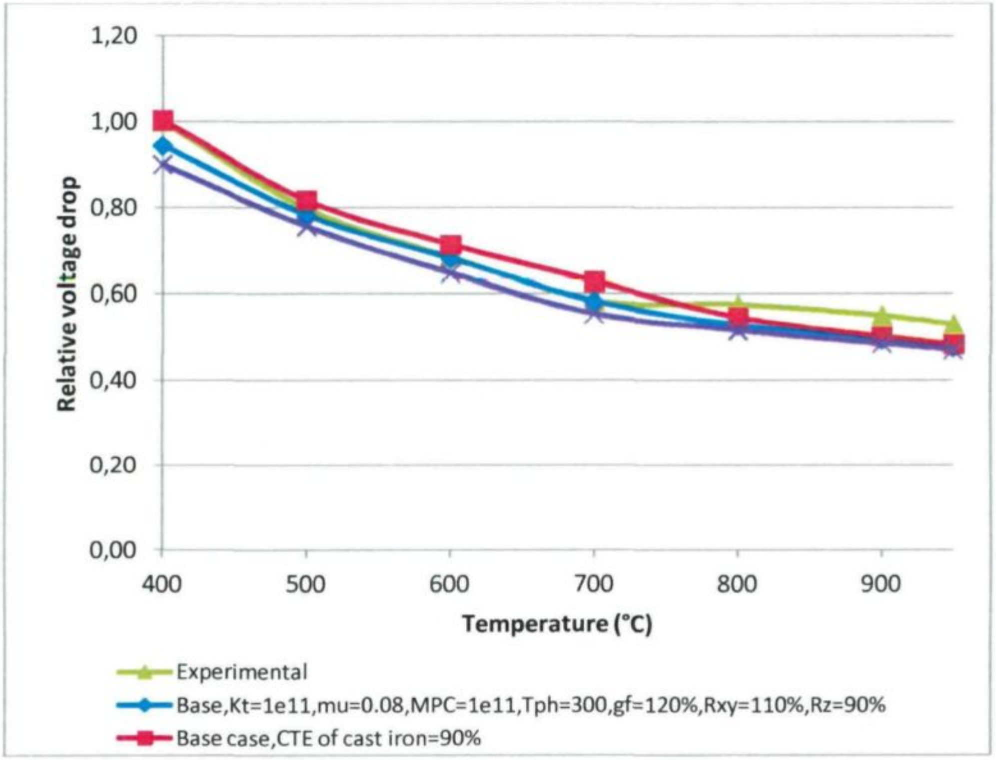

Figure 4.38: SA on the CTE of cast iron (CA-Ref)

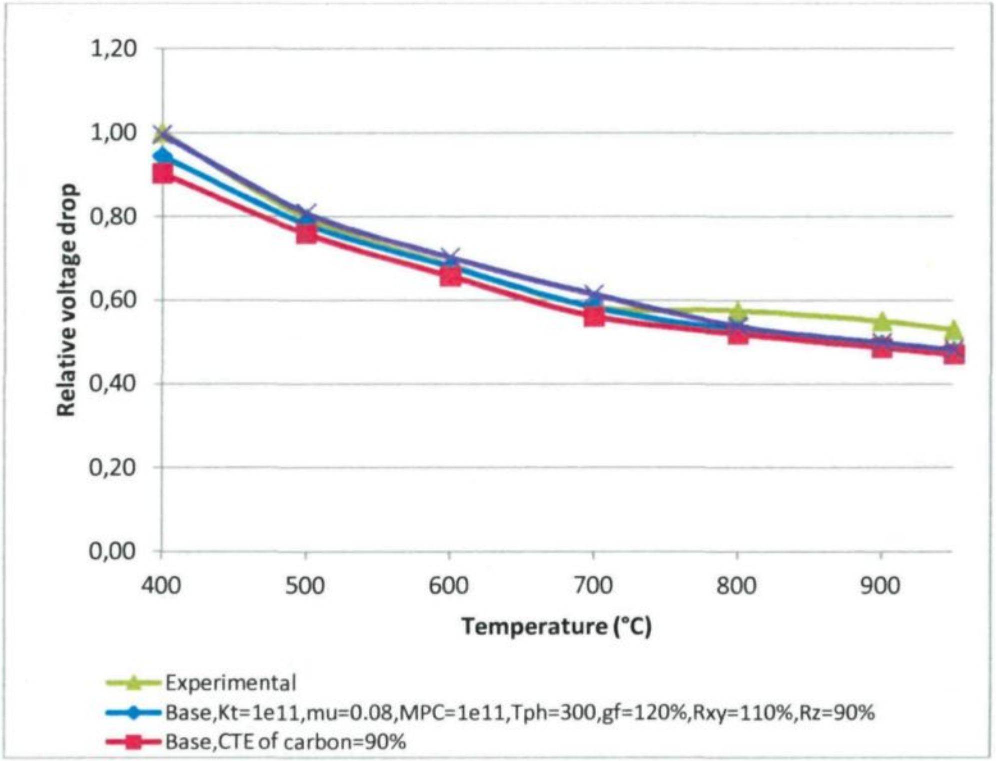

Figure 4.39: SA on the CTE of carbon (CA-Ref)

4.3.4 Phase change of steel and cast iron

A typical curve of thermal expansion of steel is shown in figure 4.40. From the figure it can be seen that steel expands with an increasing temperature. The expansion is a sustained uptrend with respect to temperature until it reaches a temperature at which a phase transition (phase change) occurs. This phase change which is known as α-γ transition in the figure can be seen as a short counter-trend move that can be physically interpreted as contraction of steel. Thermal expansion curves of cast iron of different types follow the same pattern but temperatures can be different depending on the composition. The contraction due to the phase change can change contact pressure distribution at the cast iron/carbon interface and result in a change in the contact status. It is given that with a change in contact status, the voltage drop may not be the same as before entering the phase transition temperature range. Since there has not been much work on the effect of the phase change on the voltage drop a SA simulation was performed using the results of dilatometry of steel and cast iron of the experimental model (see appendix B).

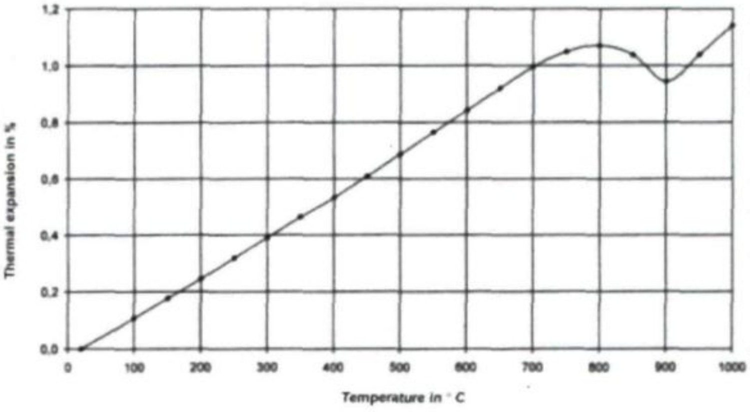

Figure 4.40: Expansion of Alouette Stub Steel [33]

It should be noted that phase change in steel and cast iron does not usually start at the same temperature and thus, their resultant impact depending on the temperatures at which phase changes start and finish can be different. Also, the amplitude of the phase change will have an impact on the amount of contraction and consequently the rate of the decrease in contact pressure. The SA on the phase change of steel and cast iron shown in figure 4.41 supports the abovementioned statements. Considering phase transition of steel and cast iron separately, a small rise in the total voltage drop at the interface was seen. This increase in the total voltage drop was higher when considering phase change of both steel and cast iron.

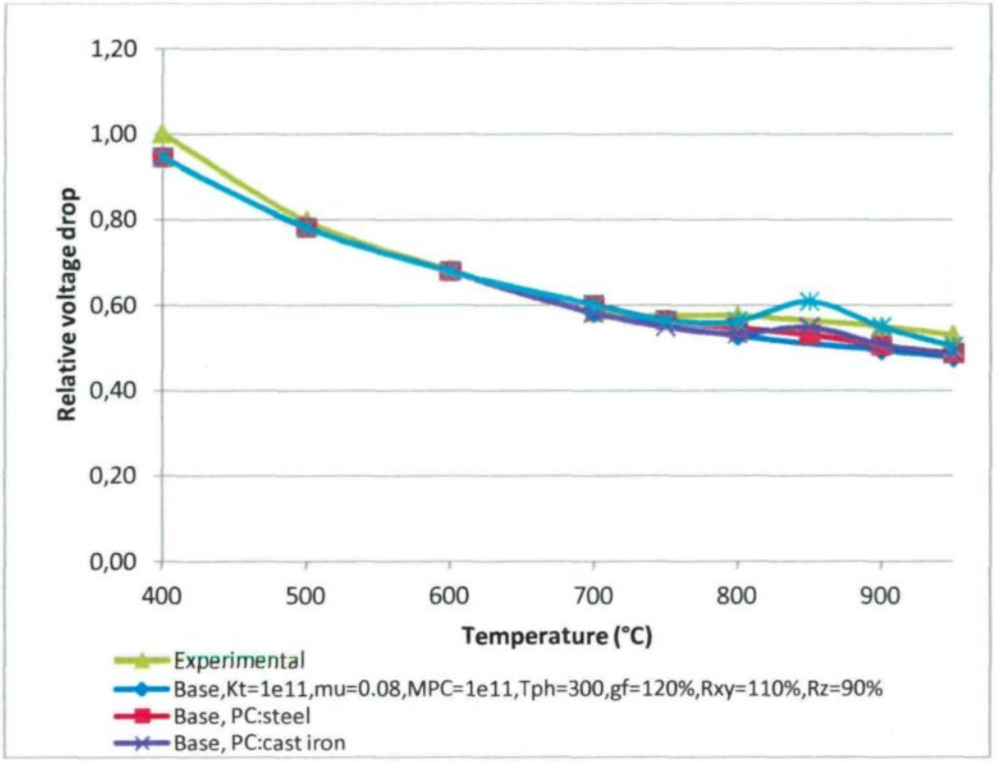

Figure 4.41: SA on the phase change of steel and cast iron (CA-Ref)

The maximum increase in the total voltage drop occurred at 850°C, reaching approximately 8% higher voltage drop compared to the experimental data. This number using base case data was 19%. However, it is clear that phase transition has a noticeable impact on the voltage drop and any effort to correct the composition of steel or cast iron in order to experience less contraction during phase transition will result in a better performance and less voltage drop. Also, correcting the composition in a way that the phase change occurs at a temperature outside the operating temperature range could be another approach.

Phase change can also occur during rodding; nonetheless, the study of such phase changes is outside the scope of this work and is ongoing in the framework of another project at the CURAL.

4.3.5 E & v as a function of temperature

Young's modulus and Poisson's ratio are two mechanical properties that have direct impacts on the magnitude of uniaxial and transverse strain respectively. Young's modulus, practically, is a measure of stiffness of the material. It is known that a change in stiffness may change contact pressure distribution and consequently contact status at the cast iron/carbon interface. For the sake of simplicity in previous work, these properties have been supposed constant while in reality they are both temperature dependent. To investigate whether such a simplification is legitimate, temperature dependency of these parameters were taken into account as per figure 4.42 to figure 4.45. Although some change in the total voltage drop was expected, no noticeable change was seen in the results of the SA on this subject as illustrated in figure 4.46.

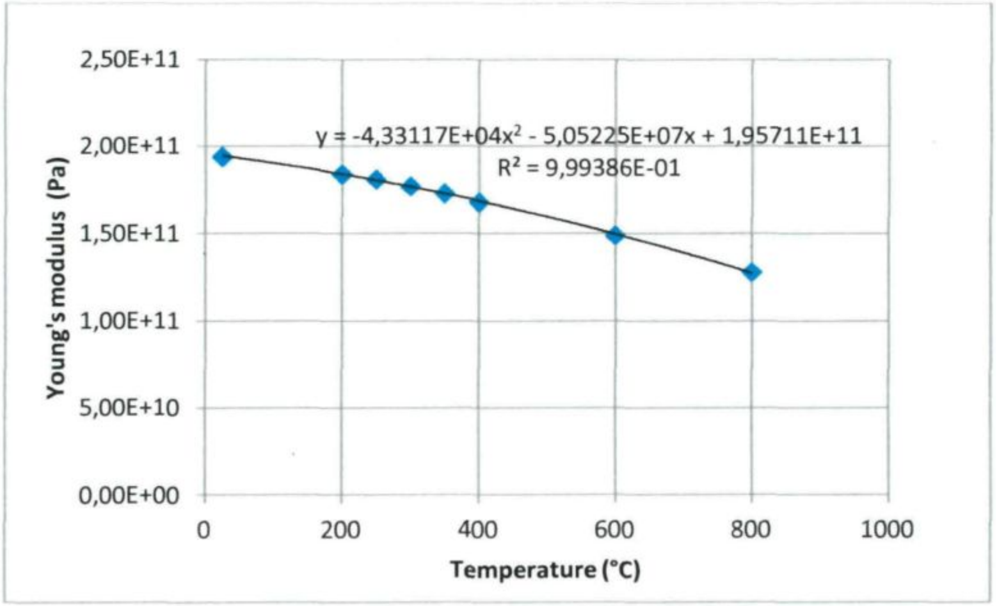

Figure 4.42: Young's modulus of steel (ref.:SAE)

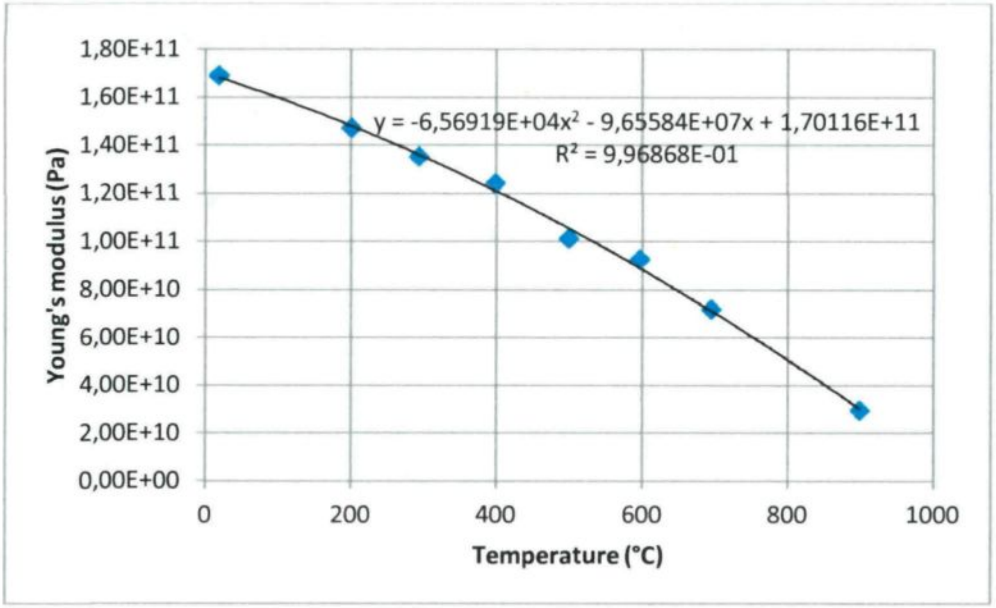

Figure 4.43: Young's modulus of cast iron (SGCI) [47]

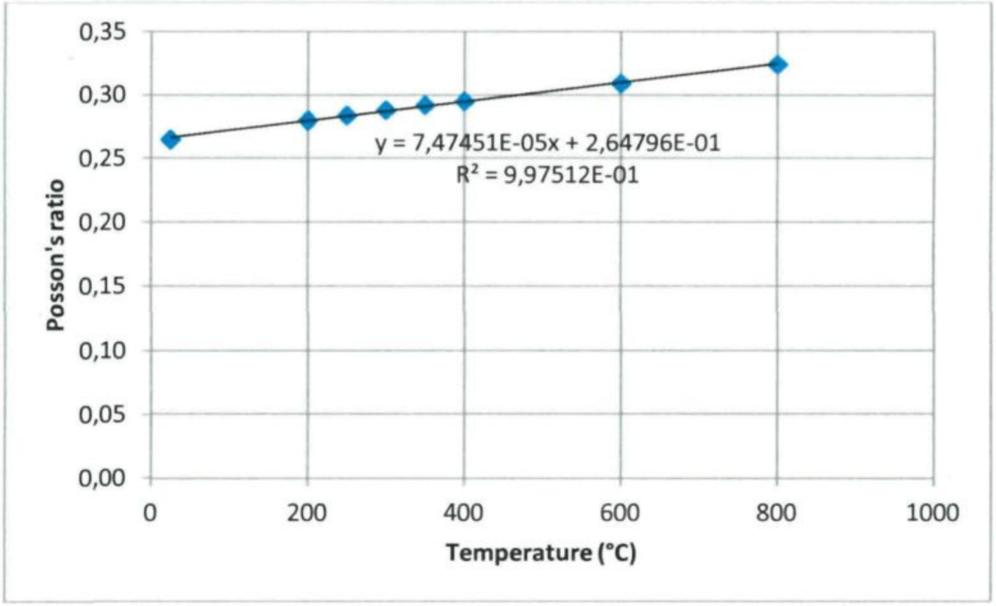

Figure 4.44: Poisson's ratio of steel (Ref.: SAE)

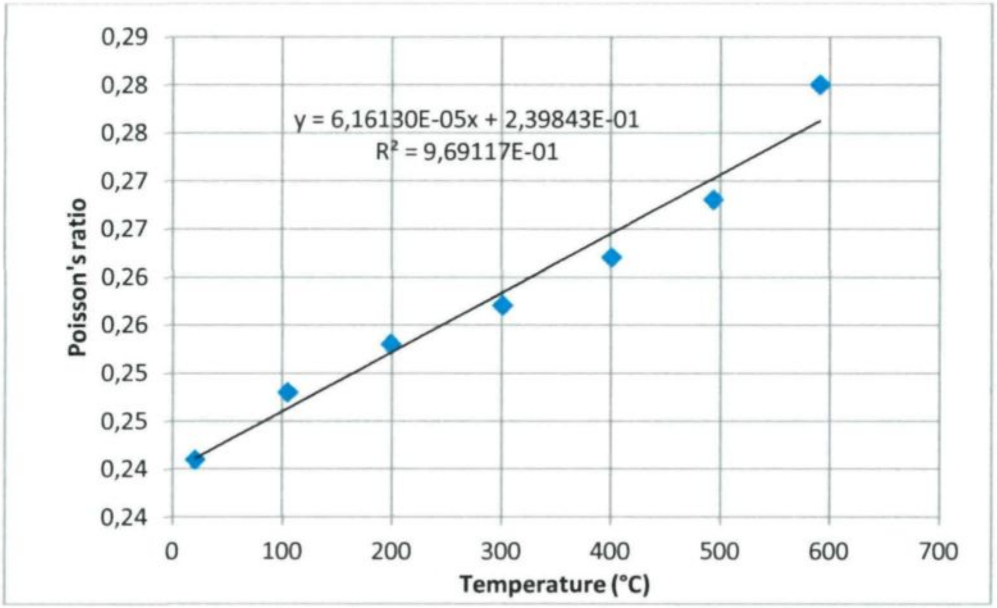

Figure 4.45: Poisson's ratio of cast iron (SGCI) [47]

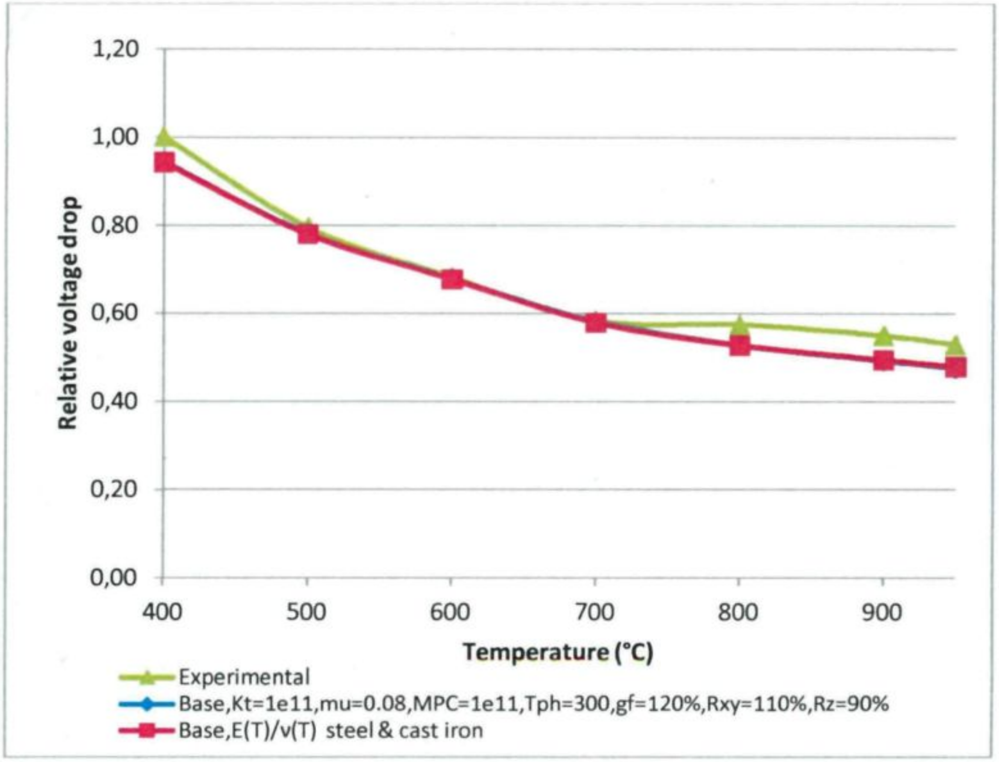

Figure 4.46: SA on the mechanical properties (E & ν) as a function of temperature (CA-Ref)

4.3.6 Electrical resistance of cast iron

Voltage drop is substantially dependent on the behavior of the cast iron connector. To determine whether or not electrical resistivity of cast iron can have an influence on the voltage drop, two SA simulations were fulfilled with 20% higher and lower values compared to the default value used in the base case. In practice, higher resistivity must result in more heat generation although that potential loss will also increase while electric current passes through cast iron from stub to carbon. Similarly lower resistivity may have an impact on the voltage drop, but inversely. The magnitude of change in voltage drop should have been measured to see whether these expectations are true or not.

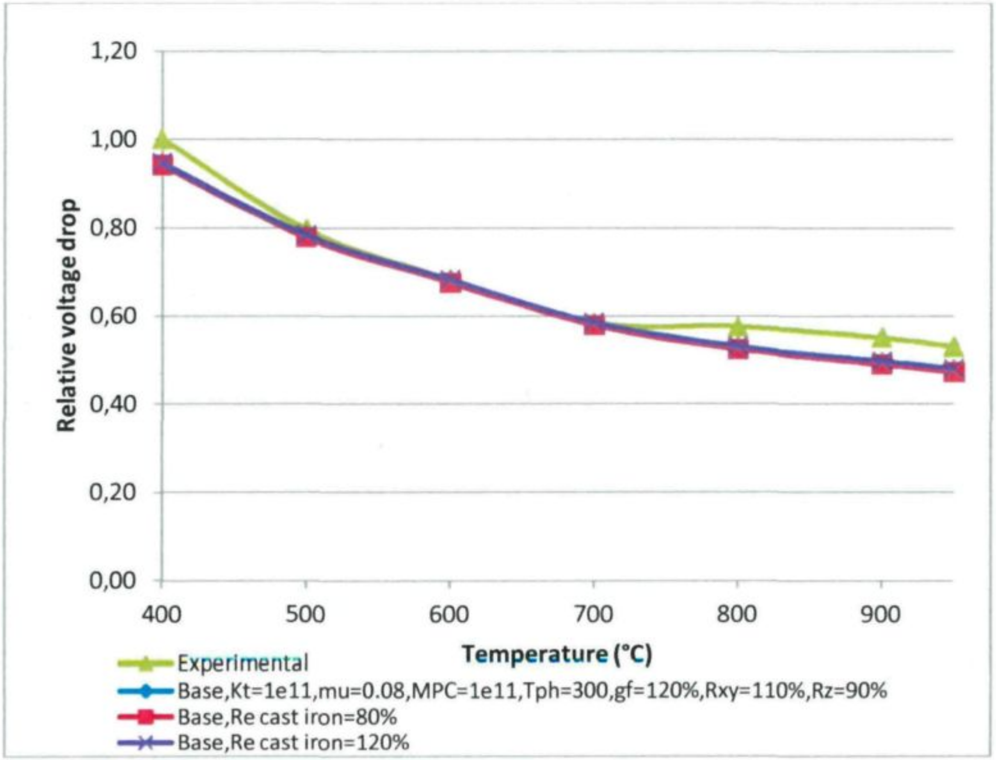

Figure 4.47: SA on the electrical resistivity of cast iron (CA-Ref)

The results obtained from the simulations as presented in figure 4.47 revealed that the change in the total voltage drop with a variation of 20% was negligible. Even though the impact at the higher temperatures was more than it was at the lower temperatures, the maximum change did not exceed 0.71% at 950°C. As expected, with a 20% increase in the resistivity of cast iron, total voltage drop increased slightly. Marginally lower voltage drop was recorded with R_e=80%$R_{e,\ base}$. Note that the results were compared to the base case.

4.3.7 Stub diameter

A change in stub diameter can originate from stub degradation due to long term use. Also, new designs may propose stubs with different diameters compared to the current design. Since stub diameter has an influence on the initial air gap at the interface, it is clear that a change in the stub diameter will affect the initial air gap so that it must be recalculated.

Three simulations were carried out with the diameter of the stub at approximately +10%, +5% and -5% compared to the base value. The results are presented in figure 4.48 through figure 4.50 for three different case of measuring voltage drop. Figure 4.48 and figure 4.49 illustrate the voltage drop between the ref. probe in the stub and probes CA1/CA2 and probe CG respectively. These two cases both encompass the stub hole and the interface between cast iron and carbon and are meant to reflect the change of voltage drop between two probes due to stub diameter change. The third case is also shown to see once again whether a change in voltage drop at higher parts of the model will have an effect on the voltage drop in carbon or not.

From the results shown in Figure 4.48 (main probes to calibrate) it can be seen that up to 500°C, all simulations generated almost the same results, but after that point, the curves swing differently. The case with the stub diameter of +5% remains below all of the curves, representing the lowest voltage drop, whereas at 600°C and 700°C it reaches its pinnacle with more than 6% lesser voltage drop compared to the base case. From those temperatures up to 950°C, it keeps an almost constant difference of 2% less voltage drop compared to the base case. -10% and -5% stub diameter cases led to an increase in the voltage drop. The augmentation in the -10% case was higher than it was in -5% case with the maximum of approximately 12% at 700°C and 800°C. This is due to the magnitude of initial air gap. With a thicker cast iron due to smaller stub diameters (intact stub hole geometry), the resultant gap will be larger and thus, contact pressure will be less and consequently the voltage will drop more at the cast iron/carbon interface.

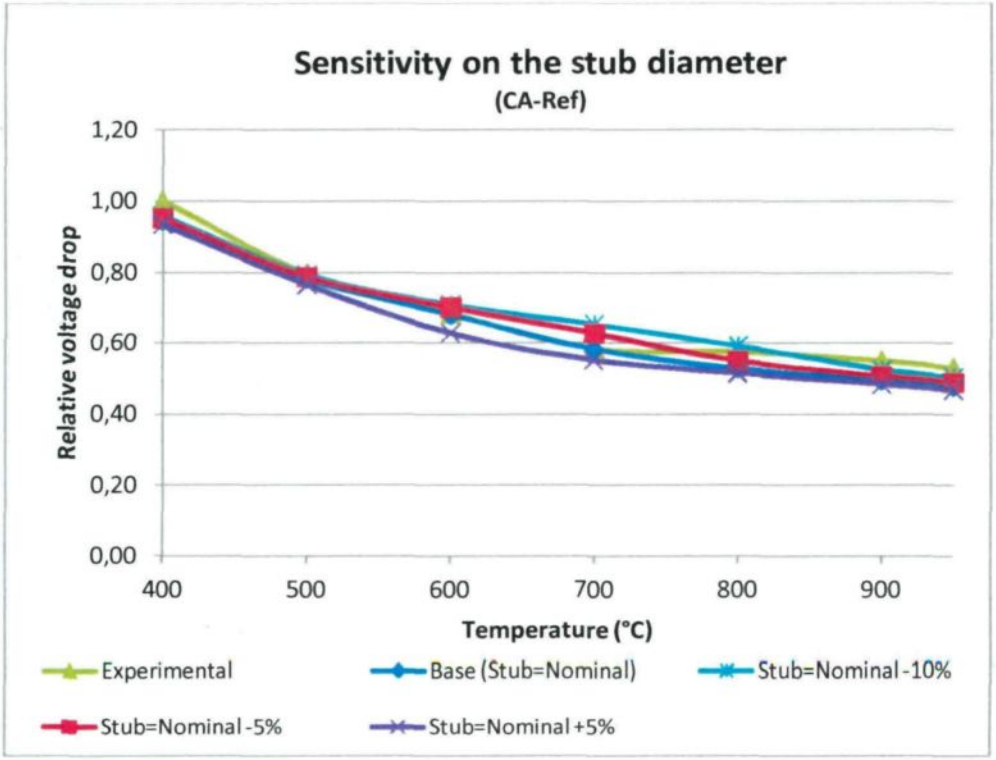

Figure 4.48: SA on the stub diameter (CA-Ref)

On the one hand, the +5% case led to less voltage drop, but on the other hand, it produced greater tensile stress especially around the stub hole, eliminating any hope of optimizing the system with a simple change in stub diameter. This is shown in figure 4.51. In the plots, maximum and minimum values have been set to identical values so that the colors represent the same range of stress in both plots. From the plots it is clear that in the case of +5% nominal diameters, the 1st principal stress (tensile stress) is much higher. Analyzing the results revealed that in the case of bigger diameter, stress decisively exceeded carbon ultimate strength, which is approximately 5 MPa. Since carbon is prone to damage and fail with stresses higher than 5 MPa, the odds are that carbon will crack and distort the contact quality and accordingly, drop the voltage drastically. Once again, not using a good constitutive law for carbon, one with the capability of predicting damage and cracking, impedes the progress of drawing any solid and reliable conclusions. With the presence of such a constitutive law, it is possible to find the diameter at which carbon reaches its ultimate strength; therefore, the opportunity to lower the voltage drop with increasing the stub diameter can be better evaluated.

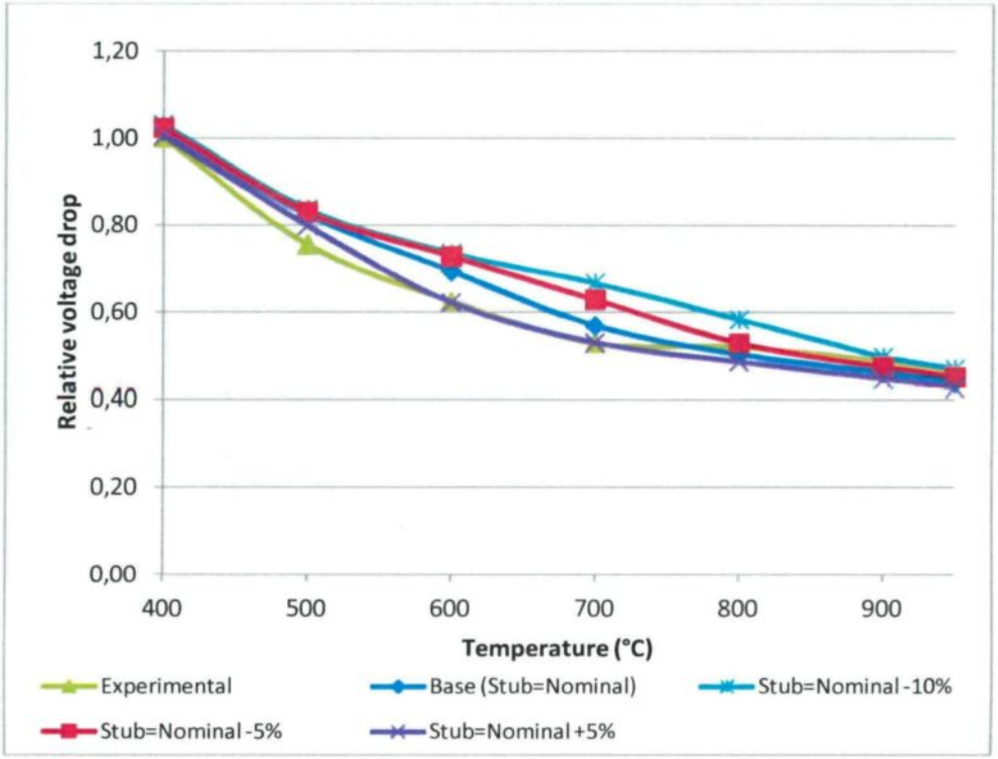

Figure 4.49: SA on the stub diameter (CG-Ref)

Almost no change was seen in the voltage drop in carbon as illustrated in figure 4.50. This simulation again showed that change in the voltage drop caused by the interface has a negligible influence on the voltage drop inside carbon. The slight difference in the readings of the probes inside carbon in the base case and in the case of different stub diameter can be due to a slightly different current path inside carbon.

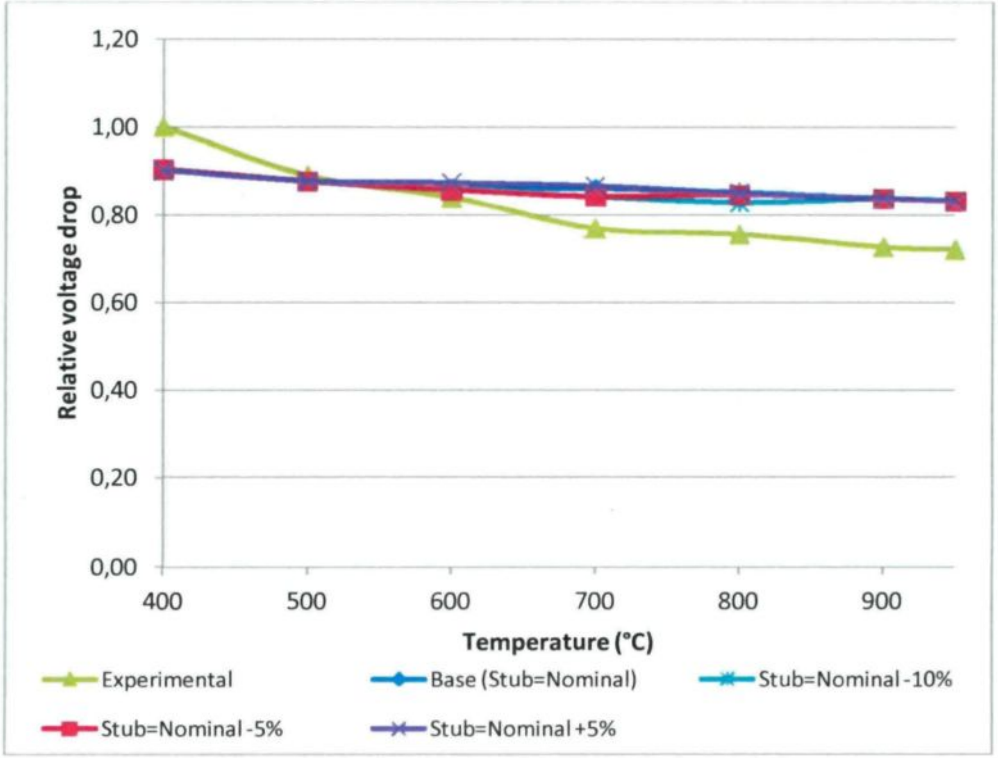

Figure 4.50: SA on the stub diameter (CA-CE2,CF2)

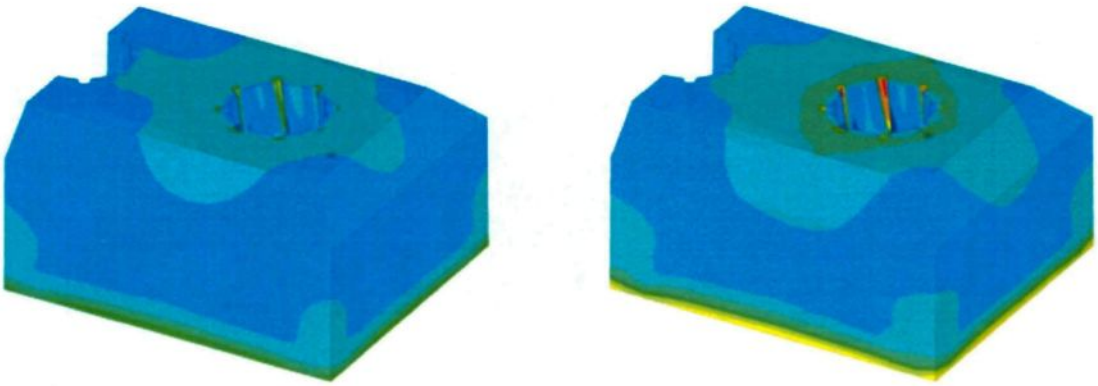

Figure 4.51: 1st principal stress nominal diameter (left), nominal+5% diameter (right)

CHAPTER 5:
CONCLUSIONS
&
RECOMMENDATIONS

5.1 General points

This chapter presents a summary of the master's thesis as well as recommendations for the future research work based on the observations and results obtained in this work.

5.2 Summary and conclusions

In the industry of the primary aluminum production, energy is of the essence since it is directly associated with the production costs and environmental issues. Hence, producers strive to derive maximum benefit from experimental and numerical studies to reduce energy loss in order to remain actively competitive in the keen worldwide competition. However, in spite of relatively abundant research to better understand the phenomena which take place in the Hall-Héroult cells and reduction process, there are still many aspects to be addressed of which the Thermo-Electro-Mechanical (TEM) phenomena that takes place in the stub hole region in the anode assembly is of significant interest. The reason behind such interest is an excellent chance of optimizing the temperature and pressure dependent contact resistance at the cast iron/carbon interface, which contributes up to 25% of the total voltage drop in the anode assembly. The Master's project presented in this thesis successfully developed a robust finite element model of a hexapod anode assembly with advanced parametrical features. A submodel extracted from the full anode assembly model was utilized to carry out sensitivity analysis on the various parameters influencing the quality of contact at the interface and consequently on the efficiency of the stub hole design.

The scripting language APDL (ANSYS® Parametric Design Language) was used to create an advanced parametric geometry of the full anode assembly model comprising many features such as number of flutes, flute shape (flute design), carbon consumption (anode with different heights to model it on a certain day of its lifetime), yoke rotation or displacement which cause angle-variant cast iron connectors, pancake formation and capability of generating submodels.. Furthermore, a more thorough and advanced approach was chosen to implement the previously defined mathematical equations for the prediction of the initial air gap distribution at the interface. The “half block” model was extracted from the full model to investigate potential distribution and voltage drop at the cast iron/carbon interface at uniform temperatures from 400°C to 950°C.

FESh++ was the code that was used to solve the fully coupled TEM model and finally calibrate it with the experimental results obtained from its laboratory model established at ARDC (Arvida Research and Development Centre) of RTA. Sensitivity analysis simulations, performed after calibration, corroborated some of the findings by other researchers and also, discovered some new facts.

The newly implemented voltage drop visualization tool in FESh++ enabled display of the voltage drop at the cast iron/carbon interface. The observations corroborated the previously found fact that more current is drawn from the lower part of the connector and also, even at higher temperatures such as 950°C, there is still high contact resistance and consequently high voltage drop at higher part of the interface due to weak contact stemming from low contact pressure.

Contact is first established at the lower part of the interface by the side surfaces of the flutes. With an increasing temperature up to 600°C, the contact area increases slowly since it is mainly controlled by the flute side surfaces, while after that point to higher temperatures, the contribution of the cylindrical portion of the interface to the total contact area, gives momentum to spread contact area to middle and higher parts of the interface. Essentially, after 700°C, contact is controlled by the cylindrical portion. The statistical tool, which was recently implemented in FESh++, revealed that the contact area ratio is 12%, 42% and 70% at 400°C, 700°C and 950°C respectively. A thorough statistical analysis discovered that voltage drop decrease with respect to a constant temperature increase slackens off dramatically after 700°C. In addition, it was noted that the rate of contact establishment was at its maximum between 600°C and 700°C, which generated contact at up to 23% of the total area of the interface (nearly 33% of the total contact area established up to 950°C).

Sensitivity analysis on the electrical contact resistance at the cast iron/carbon interface showed that the voltage drop decreases rapidly up to 700°C, by approximately 10% for each increment of 100°C; however, after that point the contribution of the interface to the total voltage drop slows down with a sustained downtrend.

The model showed higher sensitivity to change in the Coefficient of Thermal Expansion (CTE) of cast iron when a constant change of ±10% was applied to steel, cast iron and carbon separately. Unlike the CTE, the electrical resistivity of cast iron does not have much influence on the total voltage drop for a small change. Also, it was concluded that the temperature dependency of Young's modulus and Poisson's ratio is negligible, and thus assuming constant values instead of temperature dependent ones for the sake of simplicity is quite legitimate.

Phase change (transition) of both steel and cast iron has a remarkable impact on the contact condition. The contraction in the metal, caused by the transition from one phase to another, decreases the contact pressure. The cast iron connector may even lose its contact at some parts due to phase change. When the phase transition region of steel and cast iron overlaps, the magnitude of impact is larger and consequently, the voltage drop increases.

Geometrical sensitivity investigation corroborated the previous work on the change in the diameter of the stub. Although increasing the diameter of the stub results in a less initial air gap magnitude and lower contact resistance, it generates high stress in the carbon block. Considering the low tensile strength of carbon, it was concluded that carbon may not stand a chance of tolerating such high stresses considering an elastic behavior for this material.

5.3 Recommendations for future work

This research work presented excellent findings; nevertheless, it involved difficulties that may pave the way for future work and developments.

Including the rim of the cast iron connector in the geometry

Although the higher part of the cast iron/carbon interface does not establish good quality contact and most of the electric current is drawn from the lower part of the interface, it is expected that including the rim would change the mechanical behavior of the cast iron connector. For the sake of simplification, the rim has not been presented either in this work or in previous work. One reason for this is likely the difficulties in creating the geometry and meshing the cast iron connector and more importantly, the stub hole area with all important details using APDL™; however, with new versions of ANSYS®, a better mesher and geometrical modeler such as ANSYS® Workbench could solve this problem.

More realistic simulations

To model the realistic condition that the anode assembly undergoes during operation, it is necessary to consider the half anode assembly model. It is expected that the contact condition changes due to the thermal expansion in the yoke which could have an impact on the changes in the contact pressure distribution. Furthermore, in the reduction operation, an intensive thermal gradient is imposed on the anode assembly from its immerged part in the bath. In this context, convection and radiation must be taken into account to adequately evaluate the temperature distribution and consequently the potential distribution in the assembly. It is suggested that first the same simulations carried out in this research are executed with a temperature gradient (using half block model), simulating the molten bath. Nevertheless, the presented model has been calibrated and can be used to simulate the real operating conditions. The next step would be to utilize the half anode assembly model to simulate the operating condition in full.

Carbon electrical resistance around stub hole

Since in the anode fabrication process stub holes are created through punching, the density of carbon, especially around stub hole, is expected to be higher and not uniform. Since the electrical resistance of carbon depends on its density, using a uniform and even orthotropic resistance for carbon may not be enough to sufficiently evaluate voltage drop among different positions in the carbon block. In this project, different resistance was supposed for the horizontal and vertical directions, but it is recommended to measure electrical resistivity of carbon at different positions in the block to apply a better distribution of resistivity to the carbon block.

Realistic constitutive law for carbon

Utilization of a realistic carbon constitutive law (quasi-brittle with softening) is crucial. Our results have re-emphasized the need for such implementation in an anode assembly model instead of employing a simple linear constitutive law. Particularly for optimization purposes, lack of good stress and material damage and failure measurement is a serious problem that has not been solved to date. This question is currently under investigation.

Realistic air gap prediction

This thesis shows that a good prediction of the initial air gap at the cast iron/carbon interface is an essential approach to successfully evaluating the contact condition at the interface, which directly controls the voltage drop at the interface. Simulation of the solidification of the cast iron connector considering critical phase transformations and their impact on the CTE would be a good approach. To do so, a thorough metallurgical investigation must be done in order to scrutinize the scope of such impurities. In addition, cast iron properties depend on the rate of cooling in the rodding process. Since the entire cast iron does not solidify at the same time and it undergoes different cooling rates at different parts, a detailed measurement of properties should be performed to increase the accuracy of the results obtained from simulations.

Creep in metallic components

Because they undergo stresses and high temperatures during operation, it is likely that creep occurs in the metallic components of the anode assembly, namely, steel and cast iron. It is recommended to consider creep in the anode assembly model so that its impact on the contact condition can also be included.

Geometrical optimization

Simulation of the actual reduction operation should be performed prior to any attempt to optimize the system. Geometrical optimization is one of the options to improve the design and consequently, to lowering the voltage drop. The design of stub hole is a key parameter. Challenges have begun to find a better design for the stub hole; however, the author recommends applying a sophisticated approach to narrow down the number of the parameters (dimensions) in the stub hole geometry prior to any optimization effort. An approach could be defining some indices representing various dimensions. Parameters that a change in their value would result the same change in the output can be classified in one group. This way, the geometry is controlled by a few indices rather than numerous dimensions. For example, increasing the diameter of the stub will decrease the cast iron thickness, assuming that the other dimensions are kept unchanged. A decrease in the diameter of the cylindrical portion of the cast iron connector will also decrease the cast iron thickness. Therefore, since these two changes result in the same thing, an index can be defined to represent all of these impacts coming from the change in different dimensions.

BIBLIOGRAPHY

[1] Aluminum Association of Canada http://www.aac.aluminium.qc.ca/e100.html , website consulted on 30 May 2012

[2] *La Turbine CCSTI, Dossier pédagogique sur l'aluminium*, http://www.ccsti74-crangevrier.com/ressource/dossier%20peda/dossier_peda_alu.pdf, website consulted on 15 Feb 2010.

[3] Hall-Héroult process, http://en.wikipedia.org/wiki/Hall%E2%80%93H%C3%A9roult_process, website consulted on 18 Feb. 2010

[4] Cracking behavior of anodes, Markus W. Meier, ISBN 3-9521028-1-4, January 1996

[5] Daniel Richard, Patrice Goulet, Olivier Trempe, Marc Dupuis and Mario Fafard, Challenges in stub hole optimisation of cast iron rodded anodes, TMS Light Metals 2009, pp. 1067-1072

[6] V.I. Lakomsky, Electric resistance at the contact between metal and carbon bottom block in an aluminum reduction cell,Tsvetnye Metally, 5 (1993) pp. 29-33

[7] D. Richard, M. Fafard, R. Lacroix, P. Cléry, Y. Maltais, TMS Light Metals 2000, pp. 523-528

[8] Daniel Marceau, Patrice Goulet, Daniel Richard, Mario Fafard, FESh++, une nouvelle approche orientée objet pour la simulation par éléments finis des problèmes multiphysiques.

[9] R. W. Peterson, Temperature and voltage measurement in Hall cell anodes, TMS Light Metals 1976, pp. 365-382

[10] R. W. Peterson, Studies of stub to carbon voltage, TMS Light Metals 1978, pp. 367-378

[11] D. G. Brooks, V.L. Bullough, Factor in the design of reduction cell anodes, TMS Light Metals 1984, pp. 961-976

[12] R. W. Peterson, M.D. Ohlswager, G.E. Goeres, Anode cast iron thickness optimization, TMS Light Metals 1989, 499-503

[13] T. X. Hou, Q. Jiao, E. Chin, W. Crowell, C. Celik, TMS Light Metals1995, pp. 755-761

[14] D. Richard. M. Fafard, R. Lacroix, P. Cléry, and Y. Maltais, Aluminum reduction cell anode stub hole design using weakly coupled thermo-electro-mechanical finite element models, Journal of Finite Elements in Analysis and Design, no. 37, 2001, 287–304

[15] Cooper, M., Mikic, B.B., Yovanovitch, M. M, Thermal contact conductance, International journal of heat and mass transfer, Volume 12 no 2, 1969, pp. 279-300

[16] Sridhar, M. R., Yovanovitch, M. M., Elastic contact conductance model for isotropic conforming rough surfaces and comparison with experiments, Journal of heat transfer, Volume 118 no 3, February 1996

[17] Yovanovitch, M. M., Thermal contact correlations, Spacecraft radiative transfer and temperature control, Progress in Astronautics and Aeronautics, New York, Volume 83, 1982

[18] Singer, M.T., Kshonze, K., Electrical resistance of random rough contacting surfaces using surface modeling, Proc. of the IEEE 37th Holm Conference, 1991, pp. 73-82

[19] M. M. Yovanovitch, M.R. Sridhar, Wear volume. 193, 1996, pp. 91-98

[20] Mikic, B.B., Thermal contact conductance, theoretical considerations, International journal of heat and mass transfer, Volume 17,1974, pp. 205-214

[21] Majumdar, A., Tien, C. L., Fractal network model for contact conductance, Journal of heat transfer, Volume 113, 1991, pp. 516-525

[22] B. B. Mandelbrot, The fractal geometry of nature, Freeman, New York, 1982

[23] R. S. Sayles, T.R. Thomas, Nature 271 (1978) 431

[24] A. Majumdar, C.L. Tien, J. Heat Transfer 113 (1991) 516

[25] D. Richard, M. Fafard, R. Lacroix, P. Cléry, Y. Maltais, Carbon to cast iron electrical contact resistance constitutive model for finite element analysis, J. of Materials Processing Technology 132 (2003) pp. 119-131

[26] Greenwood, J. A., Williamson, J. B. P., Contact of nominally flat surfaces, Proc. of the royal society of London, Series A, Mathematical and Physical Sciences, Volume 295, London, pp. 300-319

[27] Sørlie, M. & Gran, H., Cathode collector bar-to-carbon contact resistance, TMS Light Metals 1992, pp. 779-787

[28] F. Hiltmann, J. Mittag, A. Støre and H. A. Øye, Influence of temperature and contact pressure between cast iron and cathode carbon on contact resistance, TMS Light Metals 1996, pp. 277-283

[29] J. V. Beck, Journal of Heat Transfer, volume 110, 1988, pp.1046-1058

[30] Daniel Richard, Conception des tourillons d'anode en usage dans une cuve de Hall-Héroult à l'aide de la méthode des éléments finis, Mémoire de maîtrise présentée à la Faculté des études supérieures de l'Université Laval, mai 2000

[31] L. I. Kiss, M. Rouleau and L. St-Georges, Determination of the thermal and electrical contact resistances at elevated temperatures, Proc. of the 28th Int. Thermal Conductivity Conf. and 16th Int. Thermal Expansion Conf, Thermal Conductivity 28, Thermal Expansion 16, 2006, pp.224-234.

[32] M. Rouleau, Caractérisation thermo-électro-mécanique des interfaces fonte-acier-carbone dans une cuve d'électrolyse. Master's thesis, UQAC, 2007

[33] Siegfried Wilkening and Jules Côté: Problem of the stub-anode connection, Light Metals, TMS, edited by Morten Sorlie, 2007

[34] Nedeltcho Kandev, Hugues Fortin, Electrical losses in the stub-anode connection: computer modeling and laboratory characterization, TMS Light Metals 2009, pp. 1061-1066

[35] Lyne St-Georges, László István Kiss, Mathieu Rouleau, Evaluation of contact resistance in electrodes of hall-heroult process, TMS Light Metals 2009, pp. 1103-1108

[36] Nedeltcho Kandev, Hugues Fortin, Sylvain Chénard, Guillaume Gauvin, Marie-Hélène Martin and Mario Fafard, New apparatus for characterizing electrical contact resistance and thermal contact conductance, TMS Light Metals 2011, pp. 1003-1008

[37] http://www.genisim.com/download/epfl2004.htm, consulted on 26 April 2012

[38] Marc Dupuis, Development and application of an ansys® based thermo-electro-mechanical anode stub hole design tool, TMS Light Metals 2010, pp. 433-438

[39] P. Goulet, Modelisation du comportement thermo-electro-mecanique des interfaces de contact d'une cuve de hall-heroult, Ph. D. Thesis, Laval University, Quebec, Canada, 2004

[40] H. Fortin, M. Fafard, N. Kandev, and P. Goulet, FEM analysis of voltage drop in the anode assembly, TMS Light Metals 2009, pp. 1055-1060

[41] Wangxing Li, Jieming Zhou, Yiwen Zhou, Numerical analysis of the anode voltage drop of a reduction cell, TMS Light Metals 2009, pp. 1169-1171

[42] H. Fortin, Nedeltcho Kandev & Mario Fafard, FEM analysis of voltage drop in the anode connector induced by steel stub diameter reduction, Journal of Finite Element in Analysis and Design 52 (2012), pp. 71-82

[43] http://www.tms.org/pubs/journals/jom/0002/tabereaux-0002.html, Consulted on 30 April 2012

[44] G. D'Amours, M. Fafard, A. Gakwaya & A. Mirchi, Multi-axial mechanical behavior of the carbon cathode: understanding, modeling and identification, TMS Light Metals 2003, pp. 633-639.

[45] D. Marceau, *Modélisation du contact tridimensionnel avec frottement en grandes transformations et son application a l'étude des dispositifs d'ancrages multitorons*, Ph.D. Thesis, Laval University , Québec, Canada, 2001

[46] http://en.wikipedia.org/wiki/Sensitivity_analysis, Consulted on the 11th March 2012

[47] Sheng Da & Liu Jincheng, Cast irons containing rare earths, ISBN 7302039186, Pub. Date: 2000